

Coupled electronic charge, spins, phonons and lattice imperfections in multiferroics and 2D nano-materials: First-principles Analysis

A Thesis
Submitted For the Degree of
DOCTOR OF PHILOSOPHY
in the Faculty of Science

by

Sharmila N. Shirodkar



THEORETICAL SCIENCES UNIT
JAWAHARLAL NEHRU CENTRE FOR ADVANCED SCIENTIFIC RESEARCH
Bangalore – 560 064

JULY 2014

To my parents

DECLARATION

I hereby declare that the matter embodied in the thesis entitled “**Coupled electronic charge, spins, phonons and lattice imperfections in multiferroics and 2D nano-materials: First-principles Analysis**” is the result of investigations carried out by me at the Theoretical Sciences Unit, Jawaharlal Nehru Centre for Advanced Scientific Research, Bangalore, India under the supervision of Prof. Umesh V. Waghmare and that it has not been submitted elsewhere for the award of any degree or diploma.

In keeping with the general practice in reporting scientific observations, due acknowledgement has been made whenever the work described is based on the findings of other investigators.

Sharmila N. Shirodkar

CERTIFICATE

I hereby certify that the matter embodied in this thesis entitled “**Coupled electronic charge, spins, phonons and lattice imperfections in multiferroics and 2D nano-materials: First-principles Analysis**” has been carried out by Ms. Sharmila N. Shirodkar at the Theoretical Sciences Unit, Jawaharlal Nehru Centre for Advanced Scientific Research, Bangalore, India under my supervision and that it has not been submitted elsewhere for the award of any degree or diploma.

Prof. Umesh V. Waghmare
(Research Supervisor)

Acknowledgements

I take this opportunity to thank my advisor Prof. Umesh V. Waghmare for his constant motivation and excellent guidance throughout my Ph.D. Working with him has been a thoroughly enjoyable experience, and his contagious enthusiasm for science has motivated me at various times. His valuable comments and instructions in preparing for seminars and writing papers have helped me immensely. I am extremely grateful for his kindness, endless support and encouragement during my stay at JNC.

I am thankful to Prof. C. N. R. Rao for the engaging and fascinating scientific collaborations. Working with him has been very inspiring, and has taught me how to bridge the gap between theory and experiments.

I would also like to express my gratitude to Prof. A. K. Sood and Prof. Pushan Ayyub for the interesting and fruitful scientific collaborations. I have greatly benefited from their expertise, and learned a lot in the process.

I would also like to thank Prof. A. Sundaresan, Rana Saha, Indrani Chakraborty, Anirban Pal, Sunita Dey, Pradeep Khatri, Ramakrishna Matte, Nitesh Kumar, Achintya Bera, Kota Moses and K. Vasu for the helpful collaborations.

I thank all the TSU faculty: Prof. Shobhana Narasimhan, Prof. Vidyadhiraja, Prof. Subir K. Das, Prof. Swapan K. Pati and Prof. Kavita Jain for their instructive and enjoyable courses, and stimulating scientific interactions.

I thank my present and past lab mates Summayya, Anjali, Vinay, Meha, Krishnamohan, Soumya, Jayashree, Koushik, Suchitra, Arpita, Abhishekji, Hembram, Pramod, Pawan, Biwas, Anil, Arun, Sandeep, Arghya and Deepashri for the co-operative and cheerful environment. The coffee breaks and late night discussions will always bring back fond memories.

I would like to acknowledge here the support in the form of computational facilities provided by the Centre for Computational Material Science (CCMS), JNCASR using which some of the calculations in the work presented here were performed. I would also like to thank the Complab staff and, Bharathi, Vijay and Amit from CCMS for tending to our problems at any time of the day.

I also extend my gratitude to the Librarians, Academic staff, Accounts staff and Purchase section staff for their efficiency and helpfulness.

I am also thankful to my friends in TSU: Nisha, Sananda, Ananthu, Sarada, Priyanka, Sona, Kanchan, Pramod, Wasim and Dibyajyoti for their company and help. I also thank my batch mates Dasari and Pralok for our scientific interactions.

I take this opportunity to thank all my friends in JNC: Vybhav, Chakri, Nisha, Darshana, Vinay, Anjali, Meha, Sunil, Garima, Shreyas, Vijay, Croor, Shashank, Siddharth, Sankalp, Milind, Kanwarnain, Gayatri, Deepthi, Meenakshi, Subbaiah and Aditi for the fun times. My stay in JNC would not have been as wonderful and enjoyable, if not for their presence.

I am lucky to have friends like Kaushalya, Mayuri, Priyanka, Maithilee, Anustuv and Shruti, who have been by my side through thick and thin since my school and college days.

I would also like to thank the Hostel staff, Mess workers and Chandraiah canteen for keeping me well fed. Not to forget, Sharanappa and Shivuanna for the hot cup of coffee, and Raju for maggi during our night-outs.

I am thankful to Aruna and Kruti for their warm hospitality, and for making us feel like a family.

I am grateful to my home away from home, Vrushali and Prasanna, and my aunt Aparna in Bangalore, who have always welcomed me at their homes.

Last but not the least, my parents (Aai and Baba), my brother (Abhijeet), and Grandmother for their unending support and encouragement. They have always believed in me, and never tied me down in any of my endeavours.

Synopsis

Technological growth has often been fueled by the discovery of materials exhibiting exotic properties and improved efficiency. With advances in computational resources and scientific theories, materials can be designed and their response to external stimuli can be determined through computer simulations. To this end, first-principles Density Functional Theory-based simulations have become powerful tools that enable accurate estimation of properties of materials. They permit prediction of the stability of new materials and their properties under the influence of external fields, and at the same time, provide access to atomistic information that is not readily accessible to experiments. In addition, these simulations can be used to evaluate their applicability in devices.

Behaviour of materials is determined by various couplings between electronic charge, spins and lattice degrees of freedom (phonons). All real materials inherently possess lattice imperfections or defects, which influence their electronic, optical, mechanical and thermal properties. Understanding of the impact of defects on the properties of the material, and the possibility of synthesizing crystalline materials with a good control over defect concentration permits material scientists to tailor the material properties and develop applications with improved functionality and reliability. Effects of defects can be quite significant in the stability and properties of low dimensional materials.

We have used a combination of first-principles calculations, modeling and Landau theory to (a) determine the effects of defects on the properties of bulk and 2-dimensional materials such as graphene, solid solution of graphene-hexagonal boron nitride, oxides and, (b) determine the origin of multiferroic behaviour in bulk oxides, 2-dimensional chalcogenides and elemental solids, and explore how it is influenced by defects. The thesis is divided into two main sections. The first part consisting of chapters 3, 4, and 5 focuses on the theoretical analysis of how defects and disorder influence technologically important properties of multifunctional materials such as oxides, elemental solids, graphene and solid solutions of graphene-hexagonal boron nitride systems. The second part consisting of chapters 6 and 7 explores the emergence of ferroelectricity and multiferroic behaviour in

bulk oxides and 2-dimensional materials such as a monolayer of MoS₂ and elemental selenium. In addition, we establish the inevitable role played by anti-site defects in emergence of multiferroic behaviour in (Al,Ga)FeO₃ compounds.

List of Publications

- (1) Rana Saha, Ajmala Shireen, A. K. Bera, Sharmila N. Shirodkar, Y. Sundarayya, Nandakumar Kalarikkal, S.M. Yusuf, Umesh V. Waghmare, A. Sundaresan, C. N. R. Rao, "Structure and magnetic properties of the $\text{Al}_{1-x}\text{Ga}_x\text{FeO}_3$ family of oxides: A combined experimental and theoretical study", *Journal of Solid State Chemistry* **184**, 494-501 (2011).
- (2) Indrani Chakraborty, Daniel Carvalho, Sharmila N. Shirodkar, Sandeep Lahiri, Somnath Bhattacharyya, Rajarshi Banerjee, Umesh Waghmare and Pushan Ayyub, "Novel hexagonal polytypes of silver: growth, characterization and first-principles calculations", *J. Phys. Condens. Matter* **23**, 325401 (2011).
- (3) Rana Saha, Ajmala Shireen, Sharmila N. Shirodkar, Mukta Shashi Singh, Umesh V. Waghmare, A. Sundaresan, and C. N. R. Rao, "Phase Transitions of AlFeO_3 and GaFeO_3 from the Chiral Orthorhombic (Pna21) Structure to the Rhombohedral (R3c) Structure", *Inorg. Chem.* **50**, 95279532 (2011).
- (4) Rana Saha, Ajmala Shireen, Sharmila N. Shirodkar, Umesh V. Waghmare, A. Sundaresan, C. N. R. Rao, "Effect of Cr and Mn ions on the structure and magnetic properties of GaFeO_3 : Role of the substitution site", *Journal of Solid State Chemistry* **184**, 2353-2359 (2011).
- (5) Pradeep Kumar, Achintya Bera, D. V. S. Muthu, Sharmila N. Shirodkar, Rana Saha, Ajmala Shireen, A. Sundaresan, U. V. Waghmare, A. K. Sood and C. N. R. Rao, "Coupled Phonons, Magnetic Excitations and Ferroelectricity in AlFeO_3 : Raman and First-principles Studies", *Physical Review B* **85**, 134449 (2012).
- (6) Sharmila N. Shirodkar and Umesh V. Waghmare, "Electronic and vibrational signatures of Stone-Wales defects in graphene: First-principles analysis", *Physical Review B* **86**, 165401 (2012).

- (7) Rana Saha, Ajmala Shireen, Sharmila N. Shirodkar, Umesh V. Waghmare, A. Sundaresan and C. N. R. Rao, "Multiferroic and magnetoelectric nature of GaFeO₃, AlFeO₃ and related oxides", *Solid State Communications* **152**, 1964-1968 (2012).
- (8) Nitesh Kumar, Kota Moses, K. Pramoda, Sharmila N. Shirodkar, Abhishek Kumar Mishra, Umesh V. Waghmare, A. Sundaresan and C. N. R. Rao, "Borocarbonitrides, B_xC_yN_z", *Journal of Materials Chemistry A* **1**, 5806 (2013).
- (9) Dattatray J. Late, Yi-Kai Huang, Bin Liu, Jagaran Acharya, Sharmila N. Shirodkar, Jiajun Luo, Aiming Yan, Daniel Charles, Umesh V. Waghmare, Vinayak P. David, and C. N. R. Rao, "Sensing Behavior of Atomically Thin-Layered MoS₂ Transistors", *ACS Nano* **7** (6), 4879 (2013).
- (10) Anirban Pal, Sharmila N. Shirodkar, Smita Gohil, Shankar Ghosh, Umesh V. Waghmare and Pushan Ayyub, "Multiferroic Behavior in Elemental Selenium below 40K: Effect of Electronic Topology", *Scientific Reports* **3**, 2051 (2013).
- (11) Sunita Dey, H. S. S. Ramakrishna Matte, Sharmila N. Shirodkar, Umesh V. Waghmare and C. N. R. Rao, "Charge-transfer interaction between few-layer MoS₂ and tetrathiafulvalene", *Chemistry- An Asian Journal* **8**, 1780 (2013).
- (12) K. Vasu, H.S.S.R. Matte, Sharmila N. Shirodkar, V. Jayaram, K. P. J. Reddy, Umesh V. Waghmare and C.N.R. Rao, "Effect of high-temperature shock-wave compression on few-layer MoS₂, WS₂ and MoSe₂", *Chemical Physics Letters* **582**, 105 (2013).
- (13) Indrani Charaborty, Sharmila Shirodkar, Umesh Waghmare and Pushan Ayyub, Detailed study of a stable, "A stable, quasi-2D modification of silver: Optical, electronic, vibrational and mechanical properties, and first principles calculations", *J. Phys.: Condens. Matter* **26**, 025402 (2014).
- (14) Vinay Hegde, Sharmila N. Shirodkar, Nacir Tit, Umesh Waghmare and Zain H. Yamani, "First Principles Analysis of Graphene and its Ability to Maintain Long-ranged Interaction with H₂S", *Surface Science* **621**, 168 (2014).
- (15) Indrani Chakraborty, Sharmila N. Shirodkar, Smita Gohil, Umesh V. Waghmare and Pushan Ayyub, "The nature of the structural phase transition from the hexagonal (4H) phase to the cubic (3C) phase of silver", *J. Phys.: Condens. Matter* **26**, 115405 (2014).
- (16) Kota Moses, Sharmila N. Shirodkar, Umesh V. Waghmare, C. N. R. Rao, "Composition-dependent photoluminescence and electronic structure of 2-dimensional borocarbonitrides, BC_xN (x= 1, 5)", *Mater. Res. Express* **1**, 025603 (2014).

- (17) Dattatray J. Late, Sharmila N. Shirodkar, Umesh V. Waghmare, Vinayak P. Dravid, and C. N. R. Rao, "Thermal Expansion, Anharmonicity and Temperature Dependent Raman Spectra of Single-and Few-layer MoSe₂ and WSe₂", *Chem. Phys. Chem* **15**, 1592 (2014).
- (18) Sharmila N. Shirodkar and Umesh V. Waghmare, "Emergence of Ferroelectricity at a Metal-Semiconductor Transition in 1T Monolayer of MoS₂", *Physical Review Letters* **112**, 157601 (2014).
- (19) Book Chapter: Sharmila N. Shirodkar and Umesh V. Waghmare, chapter titled "Stone-Wales Defects in Graphene and related Two-Dimensional Nanomaterials" in *Graphene: Synthesis, Properties, and Phenomena*, C. N. R. Rao and A. K. Sood, Wiley-VCH Verlag GmbH & Co. KGaA - A company of John Wiley & Sons, Inc., 2013, pp. 235-267.

List of Figures

1.1	Schematic of the coupling between various degrees of freedom in a material.	2
1.2	Main Theme.	3
1.3	Classification of defects.	3
1.4	Defect Thermodynamics.	4
2.1	Self consistent scheme used to solve the Kohn-Sham equations.	16
2.2	Pseudopotential and pseudo wavefunction	17
3.1	Structure of SW defect and variation in its formation energy with varying concentration	27
3.2	Phonon density of states of pristine and graphene with SW defect, and eigen-displacements of optical and acoustic modes in graphene.	29
3.3	Raman active phonon modes of graphene scattered by an SW defect.	31
3.4	Phonon modes that lead to structural instability of graphene with an SW defect.	33
3.5	Electronic density of states (DOS) of graphene with varying concentration of SW defects.	37
3.6	Electronic band structure of pristine graphene and graphene with SW defect.	41
3.7	Variation of band gap (E_g) of h-BN doped with graphene for different doping fractions (x).	48
3.8	Configurations of SW defects at the AC interface.	50
3.9	Configurations of SW defects at the ZZ interface.	51
3.10	Electronic Density of States (DOS) plots for SC1 without SW defect.	54
3.11	Electronic Density of States (DOS) plots for ZZ interface of SC2 without SW defect.	55
3.12	Charge density plots of HOMO (left panel) and LUMO (right panel) for all the armchair C-BN configurations with SW defects.	56
3.13	Charge density plots of HOMO (left panel) and LUMO (right panel) for zigzag C-BN configurations with SW defects.	57

3.14	Relaxed structures of CO ₂ on armchair C-BN configurations with SW defect.	59
3.15	Relaxed structures of CH ₄ on armchair C-BN configurations with SW defect.	60
3.16	Electronic Density of States (DOS) plots for CO ₂ adsorbed on the SW defect in the SC1 configuration.	61
4.1	Structure of 2H polytype of silver intercalated with oxygen and nitrogen impurities.	65
4.2	Calculated phonon dispersion curves for 2H and 4H polytypes of silver.	66
4.3	Calculated phonon dispersion curves for the 2H polytype of Ag for different values of uniaxial strain (ϵ_{zz}).	67
4.4	Fermi surface of 2H polytype of silver.	69
4.5	Electronic structure of pristine 4H polytype of silver.	73
4.6	Fermi surface plots of pristine 4H polytype of silver.	74
4.7	Phonon dispersion of pristine 4H polytype of silver.	75
4.8	Variation in stacking fault energy of 4H polytype with temperature.	76
4.9	Phase diagram for 3C and 4H polytypes of silver.	77
5.1	Orthorhombic and Corundum structures of AlFeO ₃ .	80
5.2	High-spin and low-spin state.	84
5.3	Electronic density of states for AFM and FM state of AlFeO ₃ .	85
5.4	Temperature dependence of Raman active phonons in AlFeO ₃ .	89
5.5	Distribution of phonons at Γ -point for AFM, FM and NM orderings with Fe2-Al2 anti-site defect in AlFeO ₃ .	91
5.6	First-order spin-phonon coupling (J_1) in different magnetic states in AlFeO ₃ .	94
5.7	Second-order spin-phonon coupling (J_2) in different magnetic states in AlFeO ₃ .	95
5.8	Variation of electric polarization as a function of temperature for AlFeO ₃ and GaFeO ₃ .	98
5.9	Magnetic structure of GaFeO ₃ with and without anti-site defect, and the variation of polarization with temperature for GaFeO ₃ .	100
6.1	Structure of polytypes of MoS ₂ monolayers.	106
6.2	Electronic structure of 1T-MoS ₂ .	107
6.3	Structural instabilities of the centrosymmetric 1T (<i>c1T</i>) structure of MoS ₂ .	108
6.4	Structure and properties of <i>d1T</i> -MoS ₂ .	109
6.5	Atomic displacements defining the order parameters of Landau theory of MoS ₂ .	112
6.6	Ferroelectric transition behavior, Landau free energy landscape and metallic states of <i>d1T</i> .	116
6.7	Ferroelectric domain wall in 1T-MoS ₂ .	118
6.8	Schematic of logic gates.	119

7.1	Magnetic and ferroelectric hysteresis, and magnetoelectric coupling in Se microtubes.	124
7.2	Isosurfaces of spin density of Se chains of different length with AFM and FM orderings.	126
7.3	Electronic and magnetic structure of Se (001) slab with 10 atomic planes and $U= 5$ eV.	127
7.4	Electronic structure of Se (001) slab with 10 atomic planes and $U= 3$ eV. .	129
7.5	Flowchart depicting the emergence of multiferroic behaviour in Se microtubes from half quantum of polarization.	130
7.6	Schematic depicting emergence of magnetoelectric coupling in Se microtubes.	133
7.7	Bulk phonon modes of selenium that couple with electric field applied along 'x', 'y' and 'z' directions.	136
7.8	Position vectors of Se with respect to cente of the helix.	137
7.9	Variation in the angle of rotation (per unit length) for bulk Se with frequency of incident electromagnetic radiation.	144
7.10	Flowchart depicting the emergence of magnetoelectric coupling and polarization rotation in trigonal bulk Se.	145
8.1	Schematic summarizing all the work.	149

List of Tables

1.1	Comparison between ferroelectrics and ferromagnets.	6
3.1	Structure of graphene with an SW defect: before and after relaxation. . . .	28
3.2	Frequencies of G and D Raman active modes in graphene with varying defect concentrations.	32
3.3	Cohesive energies of SZ and SD for different compositions (with GGA estimates).	46
3.4	Formation energy of SW defect at C-BN interface.	52
3.5	Bond lengths at the C-BN interface.	53
3.6	Band gaps observed in all the AC and ZZ configurations of SC1 and SC2. .	54
3.7	Energy and magnetic moments (μ) in the NM, FM and AFM configurations in ZIN_N supercell of 140 atoms.	58
5.1	Occupancy factors of $AlFeO_3$ at room temperature (RT) and at $T=30$ K. .	81
5.2	Energetics of magnetic configuration of $AlFeO_3$ and $GaFeO_3$	82
5.3	Total magnetic moments of $AlFeO_3$	83
5.4	Magnetic moments on individual Fe ions (μ_B) in $AlFeO_3$	83
5.5	Fe-O and Al-O bond lengths in $AlFeO_3$	85
5.6	List of the experimental observed frequencies at 5 K and calculated frequencies in $AlFeO_3$ for disordered AFM.	93
5.7	Modes coupling to spins at second order.	96
5.8	Magnetic moments on individual Fe ions (μ_B) in the ordered and disordered AFM state of $GaFeO_3$	99
6.1	In-plane Born effective charges ($Z_{\alpha,\beta}^*$, $\alpha, \beta = x, y$) of $d1T$ - MoS_2	110
6.2	Transformations of Γ_2^-, K_3 and K_3' modes.	113
6.3	Landau coefficients	114
6.4	Contribution of η_1 to η_5 to the ferroelectric up and down polarized states of MoS_2	117

6.5	Truth table for XNOR gate.	120
6.6	Truth table for NAND and OR gates.	120
7.1	The mode effective charges (Z^m) of Raman active E mode, and the changes due to freezing in the atomic displacements of the relevant Raman active E modes.	132
7.2	Born effective charges on all the three atoms in bulk Se.	135

Contents

Acknowledgements	v
Synopsis	vii
List of Publications	ix
List of Figures	xiii
List of Tables	xvii
1 Introduction	1
1.1 Defects	3
1.2 Ferroelectrics	5
1.3 Overview of the Thesis	8
2 Methods	11
2.1 First-principles Methods	12
2.1.1 Hohenberg and Kohn theorems	13
2.1.2 Kohn-Sham ansatz	14
2.1.3 Basis sets	17
2.2 Frozen Phonons	18
2.3 Density Functional Perturbation Theory	20
2.4 Self Consistent Ab Initio Lattice Dynamics	22
3 Graphene	25
3.1 Stone-Wales Defects in Graphene	25
3.1.1 Introduction	25
3.1.2 Computational Methods	26
3.1.3 Structure and Vibrational Spectrum	27
3.1.4 Electronic Signatures of SW Defects	36

3.1.5	Conclusions	43
3.2	Graphene- Boron Nitride (C-BN)	44
3.2.1	Introduction	44
3.2.2	Computational Methods	45
3.2.3	Chemical ordering of boron and nitrogen atoms in graphene	46
3.2.4	Variation in band gap with concentration: $C_x(BN)_{1-x}$	47
3.2.5	Structure of SW defects at the C-BN interface	49
3.2.6	Electronic structure of C-BN interface: effects of SW defects	52
3.2.7	Gas adsorption studies	58
3.2.8	Conclusions	60
4	Silver	63
4.1	Stability of 2H polytype	63
4.1.1	Introduction	63
4.1.2	Computational Methods	64
4.1.3	Stability: intercalating impurities?	64
4.1.4	Thermal Stability	65
4.1.5	Local stability of 2H polytype	66
4.1.6	Metastability of the 2H polytype	68
4.1.7	Conclusions	71
4.2	4H polytype	71
4.2.1	Introduction	71
4.2.2	Computational Methods	72
4.2.3	Electronic structure of pristine 4H polytype	73
4.2.4	Do stacking faults drive the structural phase transition?	75
4.2.5	Phase diagram of 3C and 4H polytype	77
4.3	Conclusions	78
5	Oxides	79
5.1	$Al_{1-x}Ga_xFeO_3$: structural, electronic and magnetic properties	79
5.1.1	Introduction	79
5.1.2	Computational Methods	80
5.1.3	Structure	80
5.1.4	$AlFeO_3$: Disorder, Magnetic Ordering and Stability	81
5.1.5	$GaFeO_3$: Disorder, Magnetic Ordering and Stability	86
5.1.6	Conclusions	87
5.2	$Al_{1-x}Ga_xFeO_3$: effect of anti-site disorder on spin-phonon coupling	88
5.2.1	Introduction	88
5.2.2	Computational Methods	90
5.2.3	Results and Discussion	90

5.2.4	Conclusions	97
5.3	$\text{Al}_{1-x}\text{Ga}_x\text{FeO}_3$: Multiferroic behaviour	97
5.3.1	Introduction	97
5.3.2	Computational Methods	98
5.3.3	Results and Discussion	99
5.3.4	Conclusions	104
6	Ferroelectricity in MoS_2	105
6.1	Introduction	105
6.2	Computational Methods	106
6.3	Polytypes of MoS_2	106
6.4	Electronic structure of 1T- MoS_2	107
6.5	Vibrational spectrum of $c1T$ - MoS_2 and properties of its cell tripled state . .	108
6.6	Landau Theory	112
6.7	Polarization switching	116
6.8	Dipolelectronic devices	119
6.9	Conclusions	120
7	Selenium	123
7.1	Multiferroic behaviour in elemental Selenium	123
7.1.1	Introduction	123
7.1.2	Computational Methods	125
7.1.3	Electronic structure and topology of Se	125
7.1.4	Origin of the magnetoelectric effect: spin-charge-phonon coupling . .	130
7.1.5	Conclusions	133
7.2	Optical Rotation in Selenium	134
7.2.1	Introduction	134
7.2.2	Computational Methods	134
7.2.3	Relation between Z^* and χ	135
7.2.4	Polarization rotation	143
7.2.5	Conclusions	144
8	Summary	147
	Bibliography	151

Chapter 1

Introduction

Technological growth has often been fueled by the discovery of materials exhibiting exotic properties and improved efficiency. With advances in computational resources and scientific theories, materials can be designed and their response to external stimuli can be determined through computer simulations. To this end, first-principles Density Functional Theory-based simulations have become powerful tools that enable accurate estimation of properties of materials. They permit prediction of the stability of new materials and their properties under the influence of external fields, and at the same time, provide access to atomistic information that is not readily accessible to experiments. In addition, these simulations can be used to evaluate a material's applicability and use in devices.

The physical laws that govern the properties of solids are well understood on the microscopic scale, and are described by the motion of atoms and electrons in the system (also known as first-principles methods). Since quantum mechanics governs the motion of electrons and atoms, most physical properties of a material in principle can be determined. However, evaluating and connecting the microscopic details of a solid to its macroscopic properties is a challenging task. The break-through in first-principles computational techniques was due to the Kohn-Sham [1] formalism of the density functional theory [2]. With advances in computational power, algorithms of first-principles techniques, most of the physical properties of materials can now be estimated with reliable accuracy. Some of these properties include electronic structure, stress, magnetic state, polarization, elastic

constants, vibrational frequencies, forces and bulk moduli, etc.

Behaviour of materials at the microscopic level is determined by various coupling between electronic charge, spins and lattice degrees of freedom (phonons) (see Figure 1.1). All real materials inherently possess lattice imperfections or defects, which influence their electronic, optical, mechanical and thermal properties. Effects of defects can be quite significant in determining the stability and properties of low dimensional materials in particular.

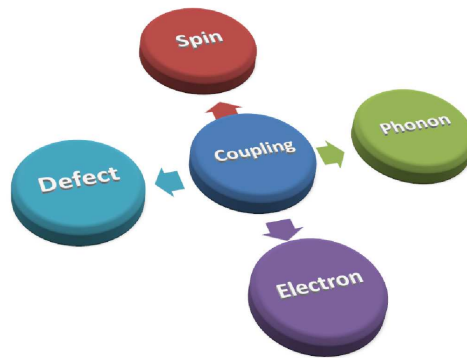


Figure 1.1: Coupling between various degrees of freedom in a material.

We have used a combination of first-principles calculations, modeling and phenomenological (e.g. Landau) theory to determine (a) effects of defects on the properties of bulk and 2-dimensional materials such as graphene, solid solution of graphene-hexagonal boron nitride, ternary oxides and, (b) the origin of multiferroic behaviour in elemental solids, 2-dimensional chalcogenides and bulk oxides, and identify the role of defects (see Figure 1.2). The thesis is divided into two main sections. The first part, consisting of chapters 3, 4, and 5.1 & 5.2, focuses on the theoretical analysis of how defects and disorder influence technologically important properties of multifunctional materials such as oxides, elemental solids, graphene and solid solutions of graphene-hexagonal boron nitride systems. The second part consisting of chapters 5.3, 6 and 7, explores the emergence of ferroelectricity and multiferroic behaviour in bulk oxides and 2-dimensional materials such as a monolayer of MoS₂ and elemental selenium. In addition, we establish the inevitable role played by anti-site defects in emergence of multiferroic behaviour in (Al,Ga)FeO₃ compounds.

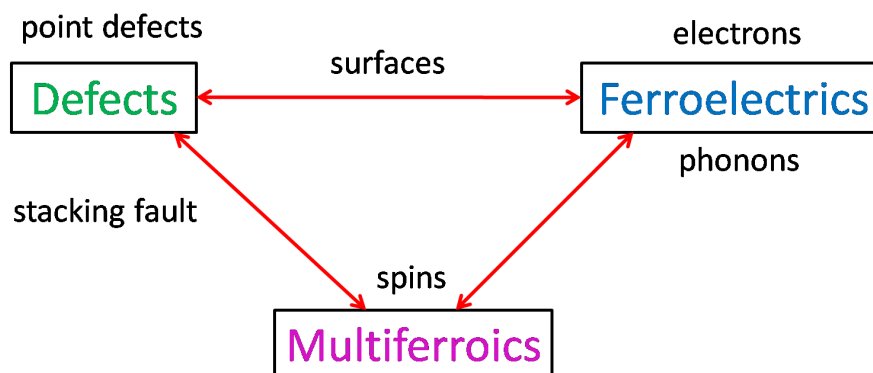


Figure 1.2: Schematic of main theme of thesis depicting the inter-relationship between defects in materials, and the emergence of ferroelectricity and multiferroic behaviour through coupling between various degrees of freedom.

1.1 Defects

Certain defects are necessary for the existence of individuality.

Johann Wolfgang von Goethe

Perfect crystals are very seldom found in nature. The properties of crystals are determined solely by their composition and crystal structure. However, all real materials inherently exhibit lattice imperfections or defects. Defects typically become a part of a material during its synthesis or treatment processes, and affect its electronic, optical, mechanical and thermal properties. Understanding of the impact of defects on the properties of the material, and the possibility of synthesizing crystalline materials with a good control over defect concentration is crucial for material scientists to tailor the material properties and develop applications with improved functionality and reliability.

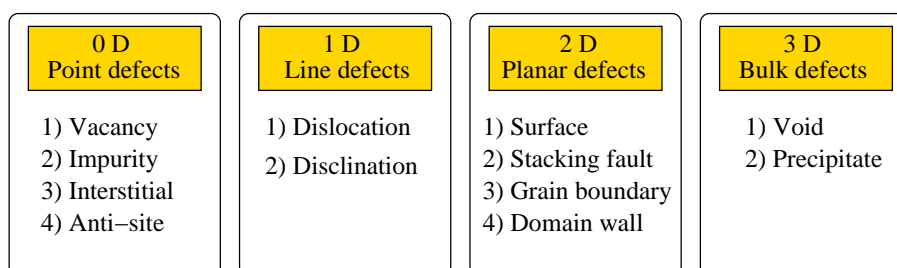


Figure 1.3: Classification of defects based on dimensionality.

Crystal lattice defects can be classified by their dimensionality as point, line, planar and bulk defects (see Figure 1.3). Point defects are 0-dimensional and involve isolated sites in the crystal structure. These defects include substitutional dopants, vacancies, interstitial impurities and anti-site defects. Line defects or dislocations are 1-dimensional defects introduced by Volterra in 1905, and are further classified into edge and screw dislocations. Surfaces, stacking faults and grain boundaries are examples of surface or 2-dimensional planar defects. The 3-dimensional defects (bulk defects) involve changes in the periodicity of the crystal over a finite volume. They include small volumes of different crystal structure or precipitates, as well as large voids or inclusions of second-phase particles.

Defect formation typically costs energy, and one expects that defect formation would be energetically unfavourable. However, defect formation is also accompanied by a change in the configurational entropy of the system which can lead to stabilization of defects in a crystal at elevated temperatures. Their stability is governed by the Gibbs free energy (G), and change in Gibbs free energy (ΔG) at temperature T is given by $\Delta G = \Delta H - T\Delta S$ (see Figure 1.4). Where ΔH is the enthalpy of defect formation, and ΔS is the accompanying change in the configurational entropy. Formation of a defect leads to increase in the configurational entropy of the system, and the equilibrium concentration of defects at finite temperatures is determined by the minimum of the Gibbs energy of the system.

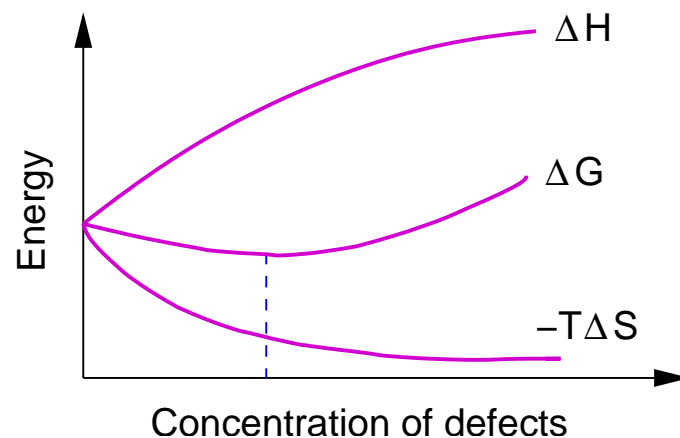


Figure 1.4: Defect Thermodynamics. Schematic of variation in Gibbs free energy (G), enthalpy (H) and configurational entropy (S) with concentration of defects. Dotted line indicates the equilibrium concentration of defects at finite temperature T .

Though defects are considered undesirable for certain physical properties of the system, defect engineering aims at manipulating these crystalline defects in order to control the behaviour of the material. Here is a quick overview of the effects of defects on physical properties solids. The diffusion rate of atoms in a solid is controlled by vacancy concentration [3, 4], whereas extrinsic defects such as interstitial [5] or substitutional dopants [6] control the electrical properties of semiconductors, and increase the mechanical strength of alloys [7]. The strength and ductility of metals [8, 9] are controlled by line defects such as edge and screw dislocations. The motion of these dislocations leads to plastic deformation of materials at lower stresses, and explains why crystals have lower strengths than the theoretically predicted values. Surfaces (planar 2-dimensional defects) are favourable sites for adsorption of molecules and atoms. Bulk defects include dispersants which may be grains, polygranular particles or large precipitates distributed through out the microstructure. Microstructure containing dispersants exhibits modified mechanical strength [10, 11] and electrical conductivity [12], which can be quite different from average of the properties of the dispersant and host phase.

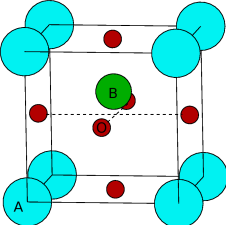
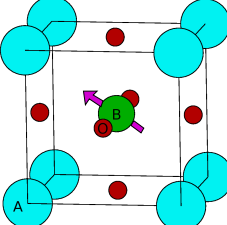
Our work investigates the effects of point defects on the electronic properties and structural stability of two dimensional materials and bulk oxides. We show that multiferroic behaviour in $(\text{Al,Ga})\text{FeO}_3$ oxides is a consequence of anti-site defects in these compounds. Our calculations also reveal that the switching of polarization in MoS_2 under experimentally achievable external fields is due to the presence of defects (domain walls) in the monolayer.

1.2 Ferroelectrics

Ferroelectrics are typically insulators that exhibit a macroscopic electric polarization arising from spontaneous ordering of electric dipoles which can be controlled with external electric and stress fields. Ferroelectrics transform from the high temperature paraelectric phase (with inversion symmetry) to the low temperature spontaneously polarized state (with broken inversion symmetry) across a transition temperature. These materials find applications in sensors, actuators and memories [13–15]. The first known ferroelectric was

the Rochelle salt, and its ferroelectricity was investigated in depth by Joseph Valasek [16]. However, Rochelle salt possesses a complex structure and is also unstable against dehydration. The breakthrough in ferroelectrics came from the discovery of ferroelectricity in potassium dihydrogen phosphate (KH_2PO_4) in 1935 by Busch and Scherer [17]. KH_2PO_4 has a relatively simple structure with ferroelectricity arising as a result of ordering of hydrogen bonds. The second world war triggered the interest in ferroelectrics, mainly for its use in sonar systems to detect submarines and other military applications, which led to the discovery of barium titanate (BaTiO_3) [18–20]. This discovery demonstrated for the first time that ferroelectricity could exist in oxide materials with relatively simple crystal structures, and that it was not always associated with hydrogen bonding. The most significant development in the theory of ferroelectricity occurred in 1960 with the formulation of the soft-mode description of the ferroelectric transition made independently by Cochran [21] and Anderson [22]. The theory explained that the ferroelectric phase transition is accompanied by softening of a transverse optic phonon mode, which freezes to distort the paraelectric phase, giving rise to a ferroelectric structure at a low temperature.

Table 1.1: Comparison between ferroelectrics and ferromagnets. The off-centering of the B cation in ABO_3 compound breaks the inversion symmetry of ferroelectrics. Whereas, the arrow at the B cation site in ferromagnets (eg. BiFeO_3) corresponds to the magnetic moment that breaks the time reversal symmetry.

	Ferroelectrics	Ferromagnets
Broken symmetry	Inversion	Time Reversal
Order parameter	Polarization (P)	Magnetization (M)
Structure		

An important signature of a ferroelectric is the breaking of inversion symmetry (which gives rise to a switchable spontaneous polarization) of the paraelectric structure at the ferroelectric transition temperature (see Table 1.1). Similarly, the magnetic analogues of ferroelectrics *i.e.* ferromagnets, that exhibit spontaneous magnetization in the absence of external magnetic fields, have broken time reversal symmetry below their magnetic transition temperature (see Table 1.1). The systems which exhibit both ferroelectricity and magnetism simultaneously are known as magnetoelectric-multiferroics. The magnetization in such materials can be controlled by external electric fields, and polarization with external magnetic fields.

From symmetry considerations, it is known that there are 21 non-centrosymmetric crystalline point groups in solids, of which 20 are piezoelectric. Out of these piezoelectric point groups, there are 10 that have a spontaneous electric polarization which varies with temperature, hence making them pyroelectric. Some of the pyroelectric materials are ferroelectric, of which only a small fraction of compounds are multiferroic. Due to symmetry restrictions and the need for complex chemical requirements for a material to be ferroelectric/multiferroic, these materials are mostly oxides with complex chemical and crystal structures. For example, ferroelectric BaTiO_3 , PbTiO_3 and KNbO_3 etc. and multiferroic BiFeO_3 , YMnO_3 and TbMnO_3 etc.

Ferroelectrics or multiferroics can be classified based on the fundamental mechanism through which inversion symmetry is broken. They can be classified as proper and improper ferroelectrics. In proper ferroelectrics, the polarization depends linearly on the degrees of freedom (electronic charge, electronic orbitals and phonons) relevant to the transition. For example, the breaking of inversion symmetry by a polar optical phonon associated with the displacement of the A/B-cation of the cubic perovskite (ABO_3) structure. Ferroelectricity in BaTiO_3 is an example of B-cation off-centering, whereas BiFeO_3 and PbTiO_3 get polarized due to A-cation off-centering. On the other hand, improper ferroelectrics are those in which polarization arises as a secondary order *i.e.* the polarization non-linearly couples with another degree of freedom. For example, ferroelectricity arising due to the breaking of inversion symmetry by charge ordering (LuFe_2O_4 [23]),

orbital ordering (SrCrO₃ [24]), magnetic ordering (TbMnO₃ [25]) or due to coupling of zone-boundary phonons (YMnO₃ [26,27]) is improper ferroelectricity. We have used first-principles calculations to understand the emergence of unexpected improper ferroelectricity and multiferroic behaviour in relatively simple (not complex oxide) materials such as elemental selenium, monolayer of MoS₂ and bulk (Al,Ga)FeO₃ compounds.

1.3 Overview of the Thesis

The objective of this thesis is to elucidate the physical properties and the behaviour of two dimensional as well as bulk materials with and without structural irregularities, using first-principles density theoretical calculations. The materials studied in this thesis are not only technologically important, but are also fundamentally interesting as they exhibit unusual phenomena which involve fascinating physics.

In chapter 2, we describe first-principles methods used in the work presented in the thesis. We first briefly lay the foundations of density functional theory (DFT), and then describe various methods used to calculate the response of a system to external perturbations. We start with discussion of Hohenberg-Kohn theorems and their implications, and then proceed to the Kohn-Sham approach which replaces the many body problem by an auxiliary independent particle problem. The approximations that form an inherent part of the formalism of DFT are discussed, and a self consistent scheme used to solve the Kohn-Sham equations will also be presented. We then proceed to discuss the various techniques that evaluate the system's response to external perturbations. Finally the chapter ends with a discussion on the Self Consistent Ab Initio Lattice Dynamics (SCAILD) method developed by Petros Souvatzis *et al.* [28] to study the lattice dynamics at finite temperatures.

In chapter 3, we present analysis of the effects of a topological defect *i.e.* the Stone-Wales (SW) defect on properties of graphene in the first part, and solid solution of graphene-boron nitride in the second. We have carried out an in-depth study of effects of SW defects on the structure and electronic & vibrational spectra of graphene, and identified the signatures of SW defects in Raman spectra and electronic density of states. We

present a quasi-continuum constitutive model which captures the mechanism of buckling of graphene associated with a SW defect based on the coupling between in-plane optical vibrational modes and the out of plane flexural mode. We have shown that the SW defects lead to a shift in the Dirac cone of graphene in k-space due to coupling of electronic structure with optical phonons. In the second part of the chapter, we discuss possible configurations of SW defects that occur at the interface between graphene and boron-nitride. We observe that the formation energies of SW defects at the interface are comparable to that in graphene, and the two-dimensional sheet buckles on the introduction of SW defects. Finally, we discuss effects of SW defects on adsorption of CO₂ and CH₄ gases at the graphene-boron nitride interface.

In chapter 4, we first analyze the stability of (a) an unusual 2H polytype of silver observed in experiments, and (b) the stability of the 4H polytype and its transformation from 4H to 3C structure. The first part of this chapter explores various possible factors such as defects, impurities, strain and anharmonic interactions that may control the stability of the 2H polytype at finite temperatures. We show that the 2H polytype has a rather flat energy landscape, and its metastability most likely arises due to the configurational entropy at finite temperatures. In the second part, we also predict the P-T phase diagram of the 3C and 4H polytypes of silver, and investigate the instability of electronic structure of the 4H polytype with respect to a Charge Density Wave (CDW), and discuss the possible mechanisms of the transformation from 4H to 3C polytype through formation of stacking faults.

In chapter 5, we discuss the effects of anti-site defects on electronic, magnetic and vibrational properties of ferrimagnetic (Al,Ga)FeO₃ orthorhombic oxides. Specifically, from the interplay between anti-site defects and vibrational spectrum of AlFeO₃, we show that a strong spin-phonon coupling in these compounds leads to the observed anomalies in its Raman spectrum. Lastly, we elucidate the role played by anti-site defects on the origin of spontaneous polarization in (Al,Ga)FeO₃ compounds, which makes them multiferroic. Using a phenomenological theory, we explain the observed polarization arising from the magnetic order and spin-phonon coupling. We demonstrate that anti-site defects play

an important role in the emergence of multiferroic/magnetoelectric behaviour in these compounds.

In chapter 6, we predict the emergence of robust ferroelectricity in a monolayer of the $1T$ form of MoS_2 as it undergoes a charge density wave transition from metallic to a semiconducting state. Our analysis shows that it originates from the nested geometry of electronic Fermi surface, and through a strong coupling of d -orbitals of Mo with valley phonons that induce an effective electric field. We use Landau theory to elucidate the improper nature of ferroelectricity predicted here. Our prediction of a 2-dimensional ferroelectric semiconductor may open up a new class of nano-scale *dipolelectronic* devices based on $1T$ - MoS_2 .

In chapter 7, we first describe the mechanism governing the emergence of multiferroic behaviour in elemental selenium. Its multiferroic behaviour is shown to be a consequence of its electronic topology, symmetry of its quasi-one dimensional chiral structure, and the coupling of phonons with electric field and spins. We show that Se possesses a half quantum of polarization *i.e.* electronic Berry phase of π , and associated metallic surface states and even number of band crossings making it a weak topological insulator. We use a Landau theory to uncover a new route to magnetoelectric behaviour in semiconductors with a chiral structure. In the second part, we show that the chiral structure of selenium makes it an optically active material in THz frequencies. We trace the origin of this optical rotatory ability to the magnetoelectric coupling that arises essentially from phonons that generate magnetic flux and couple with electric fields.

Chapter 2

Methods

Electrons and nuclei are the fundamental particles that determine most properties of atoms, molecules, thin-films and bulk materials. Many of the physical properties of materials can be determined from the derivatives of (difference between) the energy (which is the sum of electrostatic nuclear interaction energy and many-electron ground state energy) as a function of an external perturbation. For example, first derivatives of energy w.r.t. strain, magnetic field and atom positions give stress, magnetization and forces respectively. Whereas elastic constants, magnetic susceptibility and interatomic force constants are the second derivatives of energy w.r.t. strain, magnetic fields and atomic positions respectively.

In this chapter we discuss the theoretical method that has been employed in this thesis to determine the physical properties of materials. It is a quantum mechanical approach in which one considers the electrons to be in their ground state (*i.e.* adiabatic or Born Oppenheimer Approximation) for a given configuration of nuclei. In Section 2.1, we describe the ab-initio method(s) used to determine the total energy of the system. Section 2.2 describes a method *i.e.* the frozen phonon method to calculate the vibrational frequencies as an alternative to using Density Functional Perturbation Theory (DFPT). The Linear response theory or DFPT used to determine the response of a system to external perturbation is described in Section 2.3. Lastly, we describe a new quasi-harmonic method (SCAILD) developed by Souvatzis *et al.* [28] in Section 2.4 to calculate the vibrational

spectrum as a function of temperature.

2.1 First-principles Methods

To find the quantum mechanical ground state of a system of electrons and nuclei, we start with a many body Hamiltonian given by,

$$\begin{aligned} \hat{H} = & -\frac{\hbar^2}{2m_e} \sum_i \nabla_i^2 - \sum_{i,I} \frac{Z_I e^2}{|\mathbf{r}_i - \mathbf{R}_I|} + \frac{1}{2} \sum_{i \neq j} \frac{e^2}{|\mathbf{r}_i - \mathbf{r}_j|} \\ & - \frac{\hbar^2}{2M_I} \sum_I \nabla_I^2 + \frac{1}{2} \sum_{I \neq J} \frac{Z_I Z_J e^2}{|\mathbf{R}_I - \mathbf{R}_J|}, \end{aligned} \quad (2.1)$$

where \hbar is the Planck's constant, m_e and M_I are the masses of electron and I^{th} ion respectively, e is the charge of an electron, and Z_I is the charge of the I^{th} ion. \mathbf{r}_i and \mathbf{R}_I are the position vectors of i^{th} electron and I^{th} ion respectively. The first and the third terms in equation 2.1 are the kinetic and potential energies of electrons. Whereas, fourth and fifth are the kinetic and potential energy of ions. The second term describes the interaction between ions and electrons, and is treated as an external potential (V_{ext}), and also includes external perturbations such as electric or magnetic fields. Since $M_I \gg m_e$ and electrons being very fast as compared to nuclei, they are expected to follow nuclear motion instantaneously *i.e.* they always remain in their ground state. This is known as the Born-Oppenheimer approximation [29] or the adiabatic approximation. The many body wavefunction of equation 2.1 can be approximated as the product of electronic and nuclear wave functions,

$$\Psi(\mathbf{R}, \mathbf{r}) = \sum_n \phi_n(\mathbf{R}) \psi_n(\mathbf{R}, \mathbf{r}), \quad (2.2)$$

where $\psi_n(\mathbf{R}, \mathbf{r})$ is the electronic wavefunction dependent on the nuclear positions $\{\mathbf{R}\}$, and $\phi_n(\mathbf{R})$ are nuclear wavefunctions independent of electronic positions. The time independent Schrödinger's equation is given by,

$$\hat{H}\Psi(\mathbf{R}, \mathbf{r}) = \epsilon\Psi(\mathbf{R}, \mathbf{r}). \quad (2.3)$$

Substituting equation 2.1 and 2.2 in 2.3 we get,

$$\left[-\frac{\hbar^2}{2m_e} \sum_i \nabla_i^2 - \sum_{i,I} \frac{Z_I e^2}{|\mathbf{r}_i - \mathbf{R}_I|} + \frac{1}{2} \sum_{i \neq j} \frac{e^2}{|\mathbf{r}_i - \mathbf{r}_j|} + \frac{1}{2} \sum_{I \neq J} \frac{Z_I Z_J e^2}{|\mathbf{R}_I - \mathbf{R}_J|} \right] \psi_n(\mathbf{R}, \mathbf{r}) \quad (2.4)$$

$$= E_n \psi_n(\mathbf{R}, \mathbf{r}),$$

and

$$\left[-\frac{\hbar^2}{2M_I} \sum_I \nabla_I^2 + E_n \right] \phi_n(\mathbf{R}) = \epsilon \phi_n(\mathbf{R}). \quad (2.5)$$

The Born Oppenheimer approximation hence reduces the problem to solving for the electronic ground state (equation 2.4) for a given set of ionic positions. For a system with N_e number of electrons, $\psi_n(\mathbf{R}, \mathbf{r})$ is a many body wavefunction which cannot be solved exactly, and hence other approximations have to be employed to solve the eigenvalue problem.

2.1.1 Hohenberg and Kohn theorems

In 1964, Hohenberg and Kohn [2] proposed a new approach to solving the ground state properties of an electron gas in an external potential. The two theorems that constituted their ground breaking work can be stated as follows:

Theorem 1

The external potential $V_{ext}(\mathbf{r})$ of an interacting gas of electrons can be uniquely determined, except for a constant, by the ground state particle density $n_o(\mathbf{r})$.

Since all the properties are related to the energy differences, the constant shift of energy does not affect the estimation of properties.

Theorem 2

A universal functional for the energy $E[n]$ in terms of the density $n(\mathbf{r})$ can be defined, valid for any external potential $V_{ext}(\mathbf{r})$. For a given $V_{ext}(\mathbf{r})$, the exact ground state energy of

the system is the global minimum of $E[n]$, and the density that minimizes it is the exact ground state density $n_o(\mathbf{r})$.

Based on the above two theorems, we can see that the problem of functions of $3N_e$ number of variables in equation 2.4 has been reduced to functions of only 3 variables in $n(\mathbf{r})$. Since the total energy is now a functional of only the density, the theory is known as the Density Functional Theory (DFT). The total energy functional ($E_{HK}[n]$) is given by,

$$\begin{aligned} E_{HK}[n] &= T[n] + E_{ee}[n] + \int d\mathbf{r} V_{ext}(\mathbf{r})n(\mathbf{r}) + E_{ion-ion}, \\ &= F_{HK}[n] + \int d\mathbf{r} V_{ext}(\mathbf{r})n(\mathbf{r}) + E_{ion-ion}. \end{aligned} \quad (2.6)$$

Here $T[n]$ and $E_{ee}[n]$ are the kinetic and potential energies of electrons, respectively, and $E_{ion-ion}$ is the Coulomb ion-ion interaction energy. The functional F_{HK} is universal since it is only a functional of the density. However, these theorems do not provide a practical way to determine the $F_{HK}[n]$ functional or the ground state density $n_o(\mathbf{r})$. Kohn and Sham in 1965 proposed an ansatz to determine the ground state density $n_o(\mathbf{r})$.

2.1.2 Kohn-Sham ansatz

Kohn and Sham [1] gave a formalism that mapped a given many body interacting system to an auxiliary system which is a fictitious non-interacting system with exactly the same ground state density. Thus, solution of the non-interacting problem gives the ground state charge density of the real system, which can be used to determine its total energy and hence its physical properties.

In the Kohn-Sham formulation, the total energy functional can be written as,

$$\begin{aligned} E_{KS}[n] &= T_s[n] + \frac{1}{2} \int d\mathbf{r} d\mathbf{r}' \frac{n(\mathbf{r})n(\mathbf{r}')}{|\mathbf{r} - \mathbf{r}'|} + \int d\mathbf{r} V_{ext}(\mathbf{r})n(\mathbf{r}) + E_{XC}[n] + E_{ion-ion}, \\ &= T_s[n] + E_{Hartree}[n] + \int d\mathbf{r} V_{ext}(\mathbf{r})n(\mathbf{r}) + E_{XC}[n] + E_{ion-ion}, \end{aligned} \quad (2.7)$$

where $E_{Hartree}$ and E_{XC} are the Hartree and exchange correlation contributions to the total energy. Many body effects of exchange and correlation are grouped into the E_{XC}

term. The charge density $n(\mathbf{r})$ in the Kohn-Sham formalism is given by,

$$n(\mathbf{r}) = \sum_{i=1}^{N_e/2} \psi_i^*(\mathbf{r})\psi_i(\mathbf{r}), \text{ and } N_e = \int d\mathbf{r} n(\mathbf{r}), \quad (2.8)$$

where $\psi_i(\mathbf{r})$ are the single electron wavefunctions in the Kohn-Sham formalism. The Kohn-Sham single particle Hamiltonian, and the Kohn-Sham equations are:

$$\begin{aligned} H_{KS} &= -\frac{\hbar^2}{2m_e}\nabla^2 + V_{KS}(\mathbf{r}), \text{ where} \\ V_{KS}(\mathbf{r}) &= \int d\mathbf{r}' \frac{n(\mathbf{r}')}{|\mathbf{r}-\mathbf{r}'|} + V_{ext}(\mathbf{r}) + V_{XC}[n(\mathbf{r})], \text{ and} \\ H_{KS} \psi_i &= \epsilon_i \psi_i. \end{aligned} \quad (2.9)$$

The self consistent scheme used to solve the Kohn-Sham equations is illustrated in Figure 2.1. On subtracting equation 2.6 from 2.7, E_{XC} can be estimated as,

$$\begin{aligned} E_{XC}[n] &= T[n] - T_s[n] + E_{ee}[n] - E_{Hartree}, \text{ and} \\ V_{XC}[n(\mathbf{r})] &= \frac{\delta E_{XC}[n]}{\delta n}. \end{aligned} \quad (2.10)$$

The exchange correlation energy functional is not exactly known, and hence the accuracy is limited by the approximations made in the formulation of the functional. Local density approximation (LDA) [1] and generalized gradient approximations (GGA) [30,31] are the two commonly used approximations that determine the accuracy of a solution. In LDA, the exchange correlation energy density is the same as that of a homogenous electron gas of that density. In GGA, one considers the exchange correlation energy density as a function of both, the density and the gradient of density, and can be a marked improvement over LDA [32,33].

The next approximation in the DFT is that of the pseudopotential. It is known that most of the properties of a system are determined by its valence electrons with little or no contribution from its core electrons. The pseudopotential approximation exploits this aspect of solids, and replaces the core electrons and the nucleus with an effective potential which mimics how the valence electrons experience the potential of the nucleus

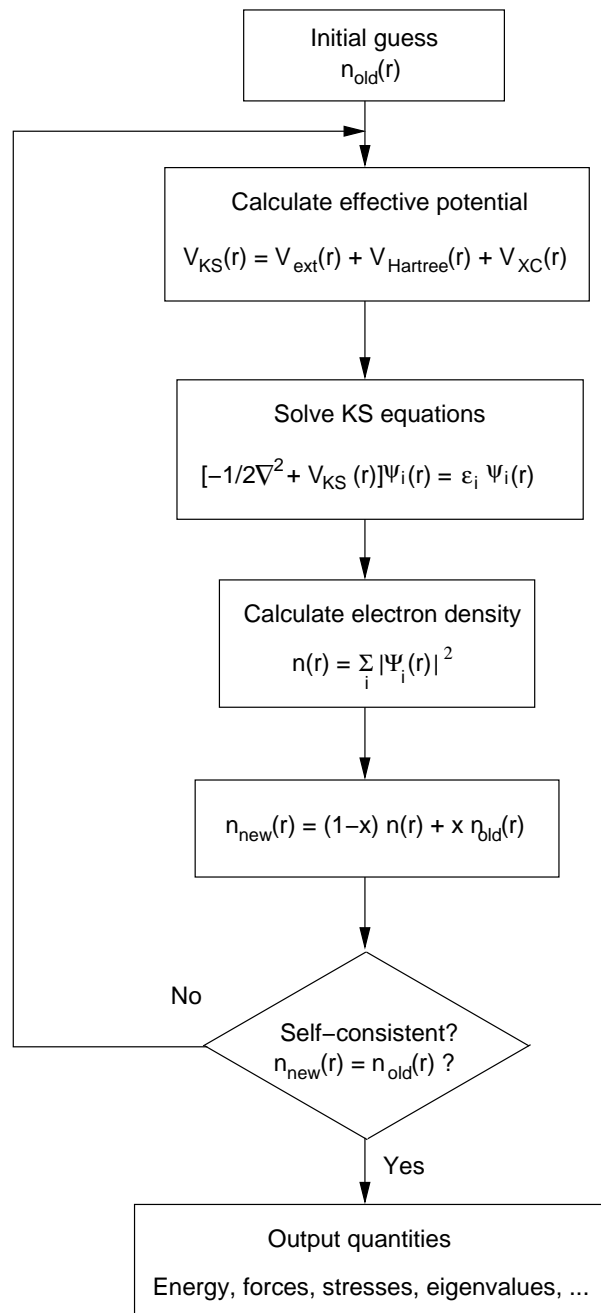


Figure 2.1: Self consistent scheme used to solve the Kohn-Sham equations.

due to screening by the core electrons. The core electrons are hence ‘frozen in’, and are considered along with the nucleus as a rigid core. Since V_{ext} diverges at the nucleus, the electronic wavefunctions near the nucleus exhibit very large oscillations. This makes their representation and hence the computational time and cost unfeasible for large systems.

A pseudopotential circumvents this problem by replacing the strong ionic potential by a weaker pseudopotential that works on the pseudo wavefunctions instead of the valence wavefunctions.

The pseudopotential is constructed by considering a cutoff radius (r_c), the region within r_c is the core region and the one beyond it is the valence region (refer to Figure 2.2). The actual (all electron) valence and pseudo wavefunctions are the same beyond r_c , whereas in the core region, the pseudo wavefunctions are constructed such that the eigenvalues and scattering properties are conserved. The total charge of each pseudo wave function is equal the charge of the actual wave function in a normconserving pseudopotential, whereas ultrasoft pseudopotentials [34] relax this criterion. However, ultrasoft pseudopotentials require a augmented charge in the core to conserve total charge. The advantage of ultrasoft pseudopotentials over normconserving is that it reduces computational cost significantly, while maintaining transferrability.

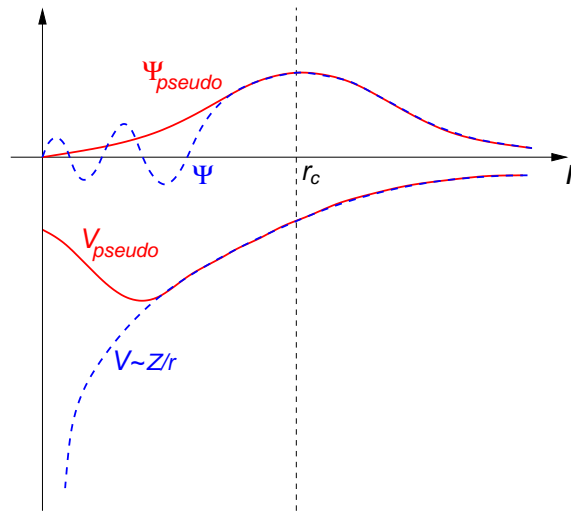


Figure 2.2: Ψ is the real wavefunction in the Coulomb potential (blue) and Ψ_{pseudo} is the pseudo wavefunction (red). The real and the pseudo wavefunction and potentials match above the cutoff radius r_c .

2.1.3 Basis sets

There are three methods used to calculate the Kohn-Sham electronic wavefunctions in materials. All three methods are equally accurate provided they are applied carefully and

are converged. These methods are distinguished based on the basis sets used to expand the independent-particle wavefunctions in the Kohn-Sham formalism. The commonly used basis sets are plane waves, atomic orbitals or a combination of both (known as mixed basis).

Plane waves are used widely for their simplicity, absence of Pulay correction [35], and are a natural basis for description of bands in sp-bonded metals and semiconductors. The KS wavefunction $[\psi_i(\mathbf{r})]$ in the plane wave basis can be expanded as follows,

$$\psi_i(\mathbf{r}) = \sum_{\mathbf{k}, \mathbf{G}} C_i(\mathbf{k} - \mathbf{G}) e^{i(\mathbf{k} - \mathbf{G}) \cdot \mathbf{r}}. \quad (2.11)$$

\mathbf{G} are the reciprocal lattice vectors and \mathbf{k} the wavevectors. In theory, an infinite number of k-points (belonging to Brillouin zone) can account for the infinitely many unit cells in extended systems. However, using a finite mesh of k-points makes it computationally feasible, under the condition that the total energy is converged with respect to the mesh size. Similarly for \mathbf{G} , the number of reciprocal lattice vectors can be limited by including all those vectors which satisfy the condition,

$$\frac{\hbar^2}{2m_e} |\mathbf{k} + \mathbf{G}|^2 \leq E_{cut}. \quad (2.12)$$

The cutoff energy (E_{cut}) is increased until the calculated total energy converges.

The atomic orbital basis captures the essence of atomic-like features of wavefunctions of molecules and solids. Mixed basis is a more general basis where the atomic-like features are incorporated near the core, and smoothly varying (plane waves) away from the nucleus [36]. We have employed plane wave basis in our first-principles calculations.

2.2 Frozen Phonons

Phonons are collective vibrations of atoms/ions in a crystal. Under the Born-Oppenheimer Approximation the electrons are in their ground state, and hence the total energy is only a function of ionic positions, $E(\{\mathbf{R}_I\})$. The adiabatic motion of the ions lies on the Born-Oppenheimer energy surface given by $E(\{\mathbf{R}_I\})$. The amplitude of vibrations is assumed

to be small as compared to the interionic spacing. With both the above assumptions, we can label the position of I^{th} ion by \mathbf{R}_I , and its displacement by \mathbf{u}_I such that $\mathbf{R}_I = \mathbf{R} + \mathbf{u}_I$. Here, \mathbf{R} is the equilibrium position of the I^{th} ion *i.e.* the position at which the forces acting on the ion are zero. The potential energy of the system on Taylor expansion in \mathbf{u} is given by,

$$V = V_o + \sum_{I,\alpha} \left. \frac{\partial E}{\partial \mathbf{R}_{I,\alpha}} \right|_{u=0} u_{I\alpha} + \frac{1}{2} \sum_{I,J,\alpha,\beta} \left. \frac{\partial^2 E}{\partial \mathbf{R}_{I,\alpha} \partial \mathbf{R}_{J,\beta}} \right|_{u=0} u_{I\alpha} u_{J\beta} + O(u^3). \quad (2.13)$$

The term linear in \mathbf{u} is the force exerted on an ion when all ions placed in their equilibrium positions (\mathbf{R}). Since there is no net force on any ion in its equilibrium position, the linear term in \mathbf{u} vanishes. Ignoring the constant term V_o and $O(u^3)$, equation 2.14 has only the quadratic term, and the force constant matrix $K_{IJ,\alpha\beta}$ is given by,

$$\begin{aligned} V &= \frac{1}{2} \sum_{I,J} \sum_{\alpha,\beta} \left. \frac{\partial^2 E}{\partial \mathbf{R}_{I,\alpha} \partial \mathbf{R}_{J,\beta}} \right|_{u=0} u_{I\alpha} u_{J\beta}, \\ &= \frac{1}{2} \sum_{I,J} \sum_{\alpha,\beta} K_{I\alpha,J\beta} u_{I\alpha} u_{J\beta}. \end{aligned} \quad (2.14)$$

Solving the equation of motion for harmonic oscillator we get,

$$M_I \frac{\partial^2 u_{I\alpha}}{\partial t^2} = - \sum_{J,\beta} K_{I\alpha,J\beta} u_{J\beta}. \quad (2.15)$$

$u_{I\alpha}$ has the following time dependence

$$\mathbf{u}_I(t) = \hat{u}_I e^{i\omega t}. \quad (2.16)$$

and hence equation 2.15 reduces to,

$$\omega^2 M_I \hat{u}_{I\alpha} = \sum_{J,\beta} K_{I\alpha,J\beta} \hat{u}_{J\beta}. \quad (2.17)$$

Solving the above eigenvalue equation gives the frequencies (ω) and eigenvectors (\hat{u}) of the phonons. For a system with N atoms, the force constant matrix is $3N \times 3N$ dimensional and has $3N$ number of modes. The structural stability of a crystal is determined by the

value of its phonon frequencies. In a stable system, the excitation of any phonon mode with frequency ω increases the energy of the system *i.e.* $M\omega^2 > 0$. In an unstable system, finite amplitude of certain (unstable) phonon modes results in lowering of total energy of the system *i.e.* $M\omega^2 < 0$, thus implying that ω is imaginary.

In the frozen phonon approach, the total energy and/or forces are calculated by displacing the atoms (*i.e.* freezing in the atomic displacements). Then the relevant quantities are defined as numerical derivatives of displacements using the following equation,

$$\begin{aligned} K_{I\alpha,J\beta} &\approx -\frac{\Delta F_{I,\alpha}}{\Delta \mathbf{R}_{J,\beta}}, \\ &\approx -\frac{\Delta F_{I,\alpha}}{2\tau}, \end{aligned} \quad (2.18)$$

where τ is the amplitude of ionic displacement that is frozen in. $\Delta F_{I,\alpha}$ is the change in the force acting on the I^{th} ion in the α direction when the J^{th} ion is displaced by $\pm\tau$ in the β direction ($\Delta \mathbf{R}_{J,\beta} = 2\tau$). To determine the phonons at wavevector \mathbf{q} using frozen phonon method, the inequivalent planes of atoms are displaced perpendicular to the direction of (\mathbf{q}) and the force acting on all atoms (see equation 2.18) have to be calculated. For $\mathbf{q} \neq \mathbf{0}$, the number of unit cells required to express the displacements should be commensurate with the wavevector. This increases the supercell size, and hence the computational cost and time. Density Functional Perturbation Theory is a technique that overcomes this drawback of the frozen phonon method.

2.3 Density Functional Perturbation Theory

Density Functional Perturbation Theory (DFPT) is a linear response technique used to compute the second derivatives of the ground state energy w.r.t. external perturbation $\lambda \equiv \{\lambda_i\}$. The first and second derivatives of the ground-state energy read as

$$\begin{aligned} \frac{\partial E}{\partial \lambda_i} &= \frac{\partial E_{ion-ion}}{\partial \lambda_i} + \int d\mathbf{r} \frac{\partial V_{ext}(\mathbf{r})}{\partial \lambda_i} n(\mathbf{r}), \\ \frac{\partial^2 E}{\partial \lambda_i \partial \lambda_j} &= \frac{\partial^2 E_{ion-ion}}{\partial \lambda_i \partial \lambda_j} + \int d\mathbf{r} \frac{\partial^2 V_{ext}(\mathbf{r})}{\partial \lambda_i \partial \lambda_j} n(\mathbf{r}) + \int d\mathbf{r} \frac{\partial n(\mathbf{r})}{\partial \lambda_i} \frac{\partial V_{ext}(\mathbf{r})}{\partial \lambda_j}. \end{aligned} \quad (2.19)$$

The electron density response $\partial n(\mathbf{r})/\partial\lambda_i$ appearing in equation 2.19 can be evaluated by linearizing equation 2.8 as

$$\Delta n(\mathbf{r}) = 2Re \sum_{i=1}^{N_e/2} \psi_i^*(\mathbf{r}) \Delta\psi_i(\mathbf{r}). \quad (2.20)$$

Here $\Delta n(\mathbf{r}) \leftrightarrow \partial n(\mathbf{r})/\partial\lambda$ in the linear approximation. The variation, $\Delta\psi_i(\mathbf{r})$ can be evaluated by standard first-order perturbation theory:

$$\begin{aligned} (H_{KS} - \epsilon_i)|\Delta\psi_i\rangle &= -(\Delta V_{KS} - \Delta\epsilon_i)|\psi_i\rangle, \\ (H_{KS} - \epsilon_i)|\Delta\psi_i\rangle &= -\hat{P}_{empty} \Delta V_{KS}|\psi_i\rangle, \end{aligned} \quad (2.21)$$

here, ΔV_{KS} is the change in the effective Kohn-Sham potential, and the first-order variation of the Kohn-Sham eigenvalue (ϵ_i) is $\Delta\epsilon_i = \langle\psi_i|\Delta V_{KS}|\psi_i\rangle$. \hat{P}_{empty} is the projector onto the empty states manifold, and given by the projector onto the occupied states as follows

$$\hat{P}_{occ} = \sum_{i=1}^{N_e/2} |\psi_i\rangle\langle\psi_i|; \quad \hat{P}_{empty} = 1 - \hat{P}_{occ}. \quad (2.22)$$

The variation in the Kohn-Sham potential is given by,

$$\Delta V_{KS}(\mathbf{r}) = \Delta V_{ext}(\mathbf{r}) + e^2 \int d\mathbf{r}' \frac{\Delta n(\mathbf{r}')}{|\mathbf{r} - \mathbf{r}'|} + \left. \frac{dV_{XC}}{dn} \right|_{n=n(\mathbf{r})} \Delta n(\mathbf{r}). \quad (2.23)$$

By selfconsistently solving the set of linear equations 2.21 (for $\Delta\psi_i$) and equation 2.23 (for ΔV_{KS}), Δn can be evaluated using equation 2.20. On reaching a reasonable accuracy, Δn is used to evaluate the second derivative of total energy using equation 2.19.

DFPT is used to evaluate the phonon frequencies by calculating the second derivatives of energy w.r.t. atomic positions (refer to equation 2.14, where the perturbation is the displacement of ions). DFPT is also used to calculate the Born effective charges ($Z_{i,\alpha,\beta}^*$) which are mixed second derivatives of total energy w.r.t. uniform static electric field (ϵ_α)

and the zone center TO modes ($u_{i\beta}$) given by,

$$Z_{i,\alpha,\beta}^* = -\frac{\partial^2 E}{\partial \varepsilon_\alpha \partial u_{i\beta}}. \quad (2.24)$$

One of the greatest advantages of DFPT over other non-perturbative methods for calculating phonon frequencies of crystalline solids (such as the frozen-phonon method) is that within DFPT, the responses to perturbations at arbitrary wave vectors \mathbf{q} (which are incommensurate with the underlying crystal periodicity) can be calculated. This avoids the use of supercells, allows the calculation of phonon frequencies at arbitrary \mathbf{q} , and makes the intensity of the calculation essentially independent of the phonon wavelength.

2.4 SCAILD

In DFPT or frozen phonon methods, phonons frequencies are calculated under the harmonic approximation *i.e.*, there exists no scattering between phonons; *i.e.* the terms of order (u^3) and higher are ignored (since the oscillations are small) in the calculation of the force constant matrix (refer to equation 2.13). However, there are many physical phenomena such as thermal expansion, thermal conductivity and even structural stability of certain crystals that can only be explained by the inclusion of anharmonic terms in the ionic interaction energy. Self Consistent Ab Initio Lattice Dynamics (SCAILD) [28] is an approach used to capture the effects of anharmonic interaction between ions, and has successfully predicted the correct structures of group IV elements which stabilize in the bcc phase due to entropy at high temperatures [37,38]. The formalism of this method is briefly explained here.

The displacement vector \hat{u}_I in equation 2.16 can be expressed as,

$$\hat{u}_I = \frac{1}{\sqrt{MN}} \sum_{\mathbf{q},s} \vartheta_{\mathbf{q},s} \xi_{\mathbf{q},s} e^{i\mathbf{q}\cdot\mathbf{R}_I}, \quad (2.25)$$

where $\xi_{\mathbf{q},s}$ is the eigenvector at wavevector \mathbf{q} and eigenmode s , and $\vartheta_{\mathbf{q},s}$ is the new canonical coordinate. At high enough temperature, the canonical coordinate $\vartheta_{\mathbf{q},s}$ can be replaced

with a real number

$$\begin{aligned}\vartheta_{\mathbf{q},s} &\approx \pm \sqrt{\langle \vartheta_{\mathbf{q},s}^2 \rangle}, \\ &\approx \pm \sqrt{\frac{\hbar}{\omega_{\mathbf{q},s}} \left[\frac{1}{2} + \bar{n} \left(\frac{\hbar \omega_{\mathbf{q},s}}{k_B T} \right) \right]},\end{aligned}\quad (2.26)$$

where, \bar{n} is the Bose-Einstein distribution function. Thus, equation 2.14 reduces to a mean field potential V^{MF}

$$V^{MF} = \frac{1}{2} \sum_{\mathbf{q},s} \bar{\omega}_{\mathbf{q},s}^2 \vartheta_{\mathbf{q},s}^2, \quad (2.27)$$

with

$$\bar{\omega}_{\mathbf{q},s}^2 = \omega_{\mathbf{q},s}^2 \left(1 + \frac{1}{2} \sum_{\mathbf{q}_1, \mathbf{q}_2} \sum_{s_1, s_2} A(\mathbf{q}, \mathbf{q}_1, \mathbf{q}_2, s, s_1, s_2) \frac{\vartheta_{\mathbf{q}_1, s_1} \vartheta_{\mathbf{q}_2, s_2}}{\vartheta_{\mathbf{q},s} \omega_{\mathbf{q},s}^2} + \dots \right), \quad (2.28)$$

where $A(\mathbf{q}, \mathbf{q}_1, \mathbf{q}_2, s, s_1, s_2)$ is the coefficient of the third order term in equation 2.13, and is given as

$$\begin{aligned}A(\mathbf{q}, \mathbf{q}_1, \mathbf{q}_2, s, s_1, s_2) &= \frac{1}{(MN)^{3/2}} \sum_{\mathbf{R}, \mathbf{R}_I, \mathbf{R}_J} \sum_{\alpha, \beta, \gamma} \frac{\partial^3 E}{\partial \mathbf{R}_\gamma \partial \mathbf{R}_{I,\alpha} \partial \mathbf{R}_{J,\beta}} \\ &\quad \xi_{\mathbf{q},s,\gamma} \xi_{\mathbf{q}_1,s_1,\alpha} \xi_{\mathbf{q}_2,s_2,\beta} e^{i(\mathbf{R}\mathbf{q} + \mathbf{R}_I \mathbf{q}_1 + \mathbf{R}_J \mathbf{q}_2)}.\end{aligned}\quad (2.29)$$

The phonon frequencies $\bar{\omega}_{\mathbf{q},s}$ can be expressed as a function of forces

$\mathbf{F}_q (= - \sum_s M \bar{\omega}_{\mathbf{q},s}^2 \vartheta_{\mathbf{q},s} \xi_{\mathbf{q},s})$ as

$$\bar{\omega}_{\mathbf{q},s}^2 = - \frac{1}{M} \frac{\xi_{\mathbf{q},s} \mathbf{F}_q}{\vartheta_{\mathbf{q},s}} \quad (2.30)$$

The self-consistent cycle used in SCAILD method for solving equations 2.27 to 2.29 is as follows:

1. A supercell calculation is carried out to estimate the frequencies $\omega_{\mathbf{q},s}$ and eigenvectors $\xi_{\mathbf{q},s}$.
2. The frequencies $\omega_{\mathbf{q},s}$ and eigenvectors $\xi_{\mathbf{q},s}$ are then used in equation 2.25 and 2.26 to

evaluate \hat{u}_I of the supercell. The \pm signs are chosen at random with equal probability for either sign, and the atoms are displaced according to \hat{u}_I .

3. The Hellman-Feynman forces are calculated on the displaced atoms of the supercell by an ab-initio code.
4. From the fourier transform of forces and using it in equation 2.30, a new set of eigenvalues $\bar{\omega}_{\mathbf{q},s}$ are calculated.
5. From the eigenvalues of step 4 a set of symmetry restored frequencies $\Omega_{\mathbf{q},s}(i) = 1, \dots, N$ are calculated.

$$\Omega_{\mathbf{q},s}^2 = \frac{1}{m_q} \sum_{S \in S(\mathbf{q})} \bar{\omega}_{S^{-1}\mathbf{q},s}, \quad (2.31)$$

where $S(\mathbf{q})$ is the symmetry group of the wavevector \mathbf{q} , and m_q the number of elements of the group. The mean value of all iterations supplies a set of frequencies $\omega_{\mathbf{q},s}$,

$$\omega_{\mathbf{q},s}^2 = \frac{1}{N} \sum_{i=1}^N \Omega_{\mathbf{q},s}^2(i) \quad (2.32)$$

The new set of frequencies in equation 2.32 are then used in step 2 to calculate a new set of displacements, and the cycle is continued until self-consistency is reached. The set of $\omega_{\mathbf{q},s}$ obtained after achieving self consistency with a reasonable accuracy are the new frequencies which include the effects of anharmonic terms in the ionic interaction energy.

In the case of dynamically unstable systems, the imaginary frequencies $\omega_{\mathbf{q},s}$ are replaced with the absolute value $|\omega_{\mathbf{q},s}|$ in step 2, keeping the rest of the procedure the same. This method has correctly predicted the stability of group IV elements such as Ti, Zr, Hf in the bcc phase at temperatures of 1293 K, 1188 K and 2073 K respectively [38]. We utilize the SCAILD method to estimate the phonon dispersion and hence the dynamic stability of 2H-polytype of silver at room temperature, which is explained in detail in Chapter 4.

Chapter 3

Graphene

3.1 Stone-Wales Defects in Graphene: A First-principles Analysis Of Its Vibrational and Electronic Signatures *

3.1.1 Introduction

Exotic electronic and thermal properties [40] of Graphene (a two dimensional/2D honeycomb lattice of carbon atoms) have opened doors to new physics and technological applications [41–43]. According to the Mermin-Wagner theorem, the long wavelength fluctuations destroy the long range order in 2D materials [44]. However, the anharmonic coupling between bending and stretching modes [45] suppress these fluctuations and give rise to strong height fluctuations (rippling). Since rippling has been observed experimentally in graphene [46] and also has a significant impact on its transport properties, a deeper understanding of its origin is required. The height of ripples purely due to thermal fluctuations [47] is grossly underestimated in theory. Ripples or out-of-plane deformation of graphene can originate also from defects [48,49], adsorption of molecules [50] and in-plane strain [51].

We explore the effects of an intrinsic defect like Stone-Wales (SW) defect on the rippling behaviour of graphene. An SW defect in graphene is obtained by 90° rotation of a

*This work has been published in part in Physical Review B [39]. Copyright (2012) by the American Physical Society.

C-C bond, and formation of an adjoining pair of pentagons and heptagons. SW defects have been observed experimentally [52], and are formed in graphene when under irradiation or during rapid quenching from high temperature. Since an SW defect does not involve application of external stress or adsorption of foreign atoms/molecules, its effect on structural deformation leads to sort of intrinsic to rippling behavior of graphene. We use quasi-continuum analysis to show that the origin of structural instabilities leading to rippling associated with SW defects in graphene [53] is in the coupling between in-plane strain and Raman active G bands.

We also investigate SW defects for a possible opening of a band gap in the electronic structure of graphene, to make it better suitable as a semiconductor for use in transistors. Previous studies [54,55] report opening of a band gap at the Dirac point due to an array of SW defects. We show that the effects of SW defects on the electronic structure are quite subtle and need deeper understanding. This chapter aims at using first-principles analysis and simple models to explore the effects on a SW defect on (a) structure and vibrational properties, (b) electronic structure, and finally (c) identification of its signatures in both vibrational and electronic spectra of graphene.

3.1.2 Computational Methods

Our first-principles calculations were based on density functional theory (DFT) as implemented in the Quantum ESPRESSO [56] code with a plane wave basis set. The interaction between ionic cores and valence electrons was captured with an ultra-soft pseudopotential [34]. Exchange-correlation energy of electrons was treated within a Local Density Approximated (LDA) functional of Perdew-Zunger (PZ) parameterized form [57] which has been effectively used in previous works [58,59]. Energy cutoff of 30 Ry was used for the truncation of plane wave basis representing wave functions, and 180 Ry for that used to represent charge density. Structures were determined through minimization of energy until Hellman-Feynman forces on each atom were smaller than 0.03 eV/Å in magnitude. The 2D sheet was simulated using a supercell geometry, with a vacuum layer of 10 Å separating adjacent periodic images of the sheet. The supercell size was varied from 3x3

to 8×8 with one SW defect in the supercell to simulate different SW defect concentrations (*i.e.* 11.11% to 1.56%). With decreasing supercell size, the in-plane distance between the periodic images of a defect decreases, and their effective concentration increases. Brillouin zone integrations were sampled over a $3 \times 3 \times 1$ mesh of k-points for a $7 \times 7 \times 1$ supercell. The dynamical matrices and phonons for pristine graphene unit cell at the wavevectors on a mesh were determined using DFT linear response as implemented in the Quantum ESPRESSO package. The phonon calculations were carried out with a uniform $21 \times 21 \times 1$ mesh of k-points in self consistent field (scf) calculations, and dynamical matrices were determined over a mesh of $7 \times 7 \times 1$ k-points.

3.1.3 Structure and Vibrational Spectrum

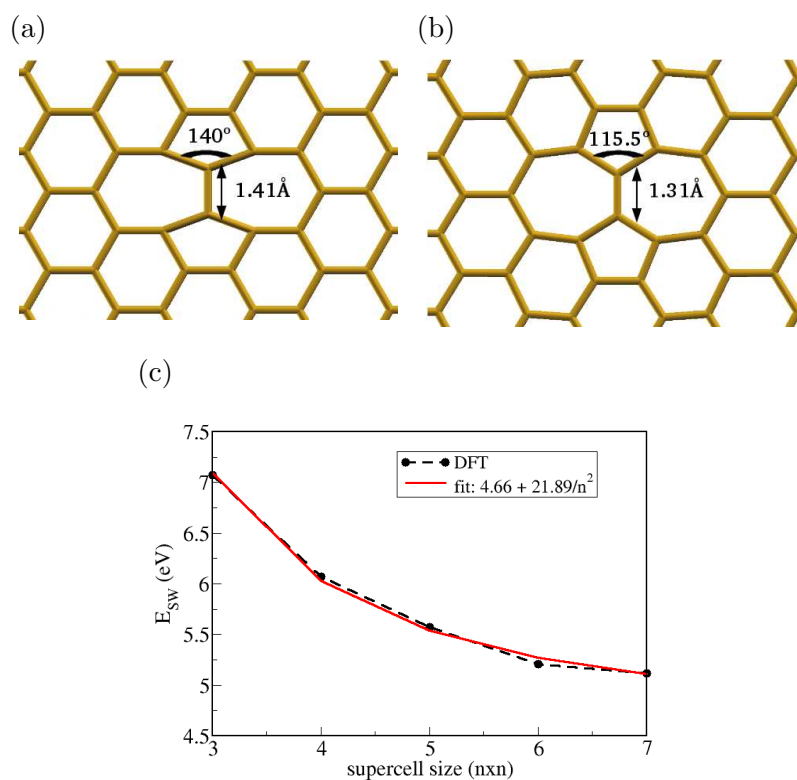


Figure 3.1: (a) Structure before relaxation and (b) after relaxation of graphene with SW defect. (c) Variation in SW defect formation energy with decreasing concentration of defects. The supercell size is given on the x axis in (c), *i.e.* separation between the defects (d). Dotted line (black) denotes the data from first-principles calculations whereas solid line (red) is the fit. Copyright (2012) by the American Physical Society [39].

The in-plane rotation of C-C bond by 90° involved in the formation of a SW defect (also known as a topological defect), transforms 4 hexagons into two pentagons and two heptagons (see Figures 3.1a and 3.1b). A pair of pentagons and heptagons makes a dislocation in graphene, and SW defect forms a dislocation dipole with two dislocations of opposite burgers' vector separated by the shortest possible distance. Mechanical and electronic properties [49, 60] are significantly affected by the orientation of the pentagon/heptagon with respect to the armchair or zigzag edges of the graphene sheet (boundary conditions). Due to periodic boundary conditions employed in our simulations (*i.e.* a periodic array of SW defects), our results are immune to edge effects particularly at low concentrations, but the anisotropy of SW defects is captured by them.

Table 3.1: Structure of graphene with an SW defect: before and after relaxation. Copyright (2012) by the American Physical Society [39]).

Property	Before	After	Difference
Pressure (kbar)	2.77	5.95	115%
Bond length (Å)	1.41	1.31	-7.1%
Bond angle	140°	115.5°	-18.2%

Upon structural relaxation, the rotated C-C bond at the centre of the SW defect shortens from 1.4 \AA to 1.31 \AA (see Table 3.1 and Figures 3.1a and 3.1b). This compares well with compression from 1.42 \AA to 1.32 \AA as reported by Jie Ma *et al.* [53]. Upon relaxation, the bond angle at the apex of the pentagon reduces from 140° to 115.5° *i.e.* \approx by -18.5%. These changes in the bond length and bond angle impose a stress, that varies from 2.77 kbar before relaxation to 5.95 kbar after relaxation for 2.04% defect concentration. Tensile and compressive stresses develop along and perpendicular to the direction of the rotated bond, respectively. As reported in the earlier work [49], a graphene nano-ribbon reduces this in-plane stress by out of plane buckling (*i.e.* by forming a non-planar structure). The formation energy of a SW defect reduces by a factor of 2.24 (also

due to structural relaxation), which is equivalent to a lowering of energy by ≈ 6.4 eV. The formation energy of a SW defect in a 7×7 supercell is ≈ 5.16 eV. We note that the formation energy of an SW defect is dependent on its concentration, *i.e.* the in-plane separation between the defects, the boundary conditions and the periodicity of the SW defects. From our simulations (involving a periodic array of SW defects), we find that the interaction between two SW defects is repulsive, implying that SW defects would minimize energy by maximizing the separation between them. This interaction energy falls off as $1/d^2$, and its coefficient is proportional to the shear modulus for graphene (refer to equation (5) in the previous work [61]). The formation energy reaches a constant value of 4.66 eV at the limit of infinite separation (see Figure 3.1c). Even though the formation energy of SW defects is high, these defects do form during synthesis or under irradiation (by electrons) and have been observed experimentally [52].

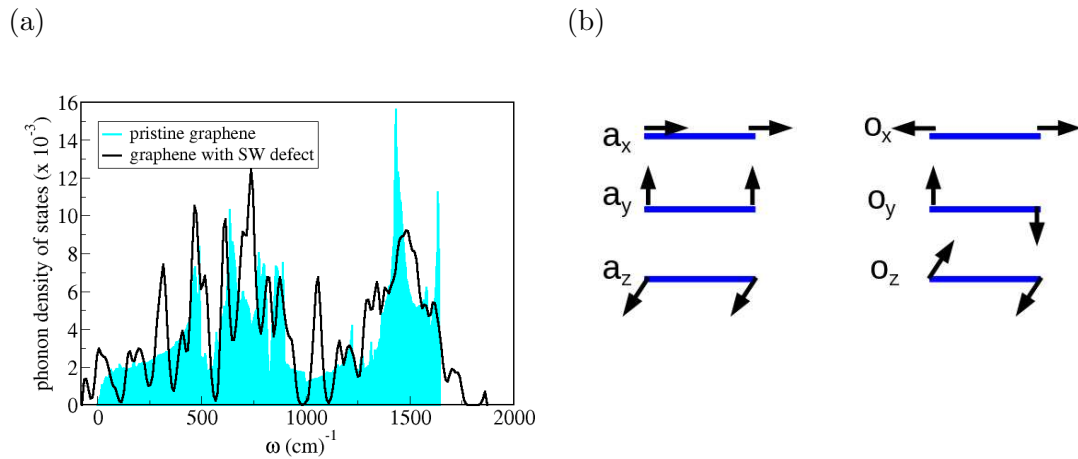


Figure 3.2: (a) Phonon density of states of pristine graphene and graphene with SW defect (for 2.04 % concentration of defects). Light blue and black denote phonon density of states for pristine graphene and graphene with SW defect respectively. (b) Eigen-displacements of optical and acoustic modes in graphene. Copyright (2012) by the American Physical Society [39].

The structural changes accompanying a SW defect in graphene lead to changes in its vibrational spectrum, and can be identified in its Raman spectra. A SW defect in graphene is reflected in changes in its vibrational spectrum leading to unstable and high frequency defect modes (see Figure 3.2a). Phonons associated with G and D bands of graphene are

scattered by an SW defect, reflected in changes in their frequency and eigen-displacements near the SW defect. We analyze this with the spectrum obtained with frozen phonon calculations (at Γ -point) for a 7x7 supercell with SW defect concentration of 2.04% (*i.e.* 1 defect per 7x7 supercell). Due to BZ folding, the D band at K-point in the BZ of the unit cell gets folded back onto the K-point in the BZ of 7x7 supercell. Since the BZ of 7x7 supercell is small, its K and Γ -points lie rather close to one another, and this makes the atomic displacements in the eigen-vectors of phonons in a given branch for K and Γ -points to be similar. Hence, we consider that the D band of a 7x7 supercell with a defect is very similar to the one of its Γ -point phonon modes. We project the normal-modes of graphene with SW defect onto those of pristine graphene to indentify the G and D bands in graphene. This is achieved by calculating an overlap or correlation matrix given by,

$$S_{\alpha\beta} = \langle e_{\alpha} | e'_{\beta} \rangle, \quad (3.1)$$

where e'_{β} is the eigen-vector of graphene with SW defect and e_{α} is the eigen-vector of pristine graphene. The G and D bands of graphene with SW defect are identified as those with the largest overlap with the G and D eigen-vectors of pristine graphene (see Figure 3.3).

The doubly degenerate in-plane stretching mode, *i.e.* G band of frequency 1582 cm^{-1} dominates the Raman spectrum of pristine graphene. The D band (defect mode) at the frequency of 1350 cm^{-1} at K-point is a mode that becomes Raman active in the presence of defects. The defect concentration in graphitic materials is typically characterized using the ratio of integrated Raman intensities of D band and G band. We show that the frequencies of G and D bands shift with varying defect concentration. Atomic displacements in the D band are localized at the SW defect, while those in the G band are excluded at the defect (refer to Figures 3.3a to 3.3c). Symmetry equivalence of the x and y directions in the hexagonal lattice is broken by the anisotropy of the SW defect, lifting the degeneracy of G band. While the D band hardens from 1324 cm^{-1} to 1337 cm^{-1} , frequency of the G band lowers noticeably from 1582 cm^{-1} to 1544 cm^{-1} for vibrations with atomic displacements along the rotated C-C bond, and from 1582 cm^{-1} to 1556 cm^{-1} for vibrations

perpendicular to the rotated C-C bond.

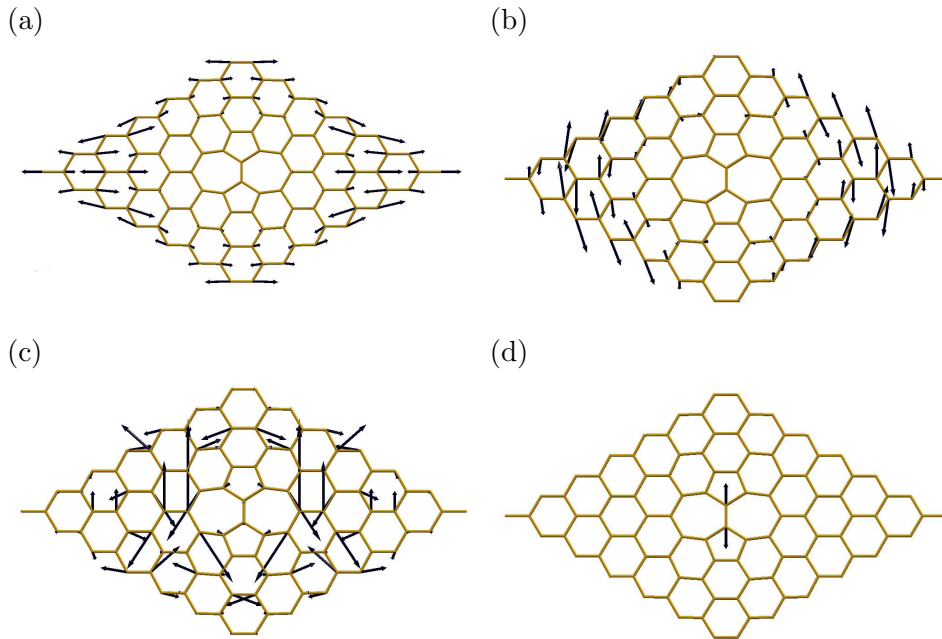


Figure 3.3: Raman active phonon modes of graphene scattered by an SW defect (for 2.04 % concentration of defects). G band: (a) mode with atomic displacements along the unrotated C-C bonds, of frequency $\approx 1556 \text{ cm}^{-1}$, and (b) mode with atomic displacements perpendicular the unrotated C-C bonds, of frequency $\approx 1544 \text{ cm}^{-1}$. (c) D band is attracted to the SW defect and its frequency hardens to $\approx 1337 \text{ cm}^{-1}$. (d) Highest frequency defect mode of graphene with an SW defect. This mode at 1861 cm^{-1} involves stretching of the stiff rotated C-C bond at the centre of the defect. Copyright (2012) by the American Physical Society [39]).

The red shift in G band found here is consistent with earlier reports [55], however no explanation for the observed shift in frequencies had been reported. We explain the softening of G band and hardening of D band frequencies in terms of the structural changes occurring at the SW defect. The rotated C-C bond at the centre of SW defect is 7% shorter, and hence it is stiffer than the unrotated C-C bonds. The stiffness of this bond is evident from the high frequency defect mode (of frequency 1861 cm^{-1} , and compares well with reported value [53]) which is entirely localized to the rotated bond of the defect (see Figure 3.3d). The stress built up by the bond contraction is released to the bonds surrounding the SW defect. Hence, the stiffness of bonds in the neighbourhood of the defect is less as compared to that of the rotated C-C defect bond. As a result, the D band localized at

the SW defect hardens, and G band excluded by the defect softens.

Table 3.2: Frequencies of G and D Raman active modes in graphene with varying defect concentrations. Vibrations of G_1 band are perpendicular and vibrations of G_2 band are parallel to the rotated C-C bond of the SW defect. Copyright (2012) by the American Physical Society [39]).

Supercell size	G_1 (cm^{-1})	G_2 (cm^{-1})	D (cm^{-1})
Pristine graphene	1582	1582	1324
3x3	1599	1783	1277
5x5	1577	1526	1367
7x7	1556	1544	1337

We have carried out similar analysis of the vibrational spectrum of graphene with higher defect concentration, *i.e.* one defect in a 5x5 supercell. This too shows a similar behaviour *i.e.* the softening of G band, and hardening of the D band (refer to Table 3.2). The magnitude of frequency shifts of G and D bands in this case is larger, due to higher concentration of SW defects, *i.e.* 4%. The frequency of the G band lowers and splits into 1577 cm^{-1} and 1526 cm^{-1} , for vibrations along the unrotated C-C bond and along the rotated C-C bond respectively. In the case of the 3x3 supercell, *i.e.*, 11.11% concentration of defects, the average distance between SW defects becomes comparable to the length scale at which these modes are scattered, and hence they show contrasting behavior. The G band hardens to 1783 and 1599 cm^{-1} , for vibrations along the rotated C-C bond and along the unrotated C-C bond, respectively. On the other hand, the D band softens to 1277 cm^{-1} (refer to Table 3.2).

Two phonon modes appear with imaginary frequencies in the vibrational spectrum of graphene with an SW defect, revealing its structural instability. These two phonon modes involve out-of-plane displacement of atoms and cause the graphene with an SW defect to buckle. One mode has sine wavelike ($\approx 65i \text{ cm}^{-1}$) (odd) deformation and the other has

cosine wavelike ($\approx 53i \text{ cm}^{-1}$) (even) deformation (for 7×7 supercell with 1 SW defect). These modes will be referred to as odd and even unstable modes (refer to Figure 3.4a, 3.4b and 3.4c, 3.4d) respectively.

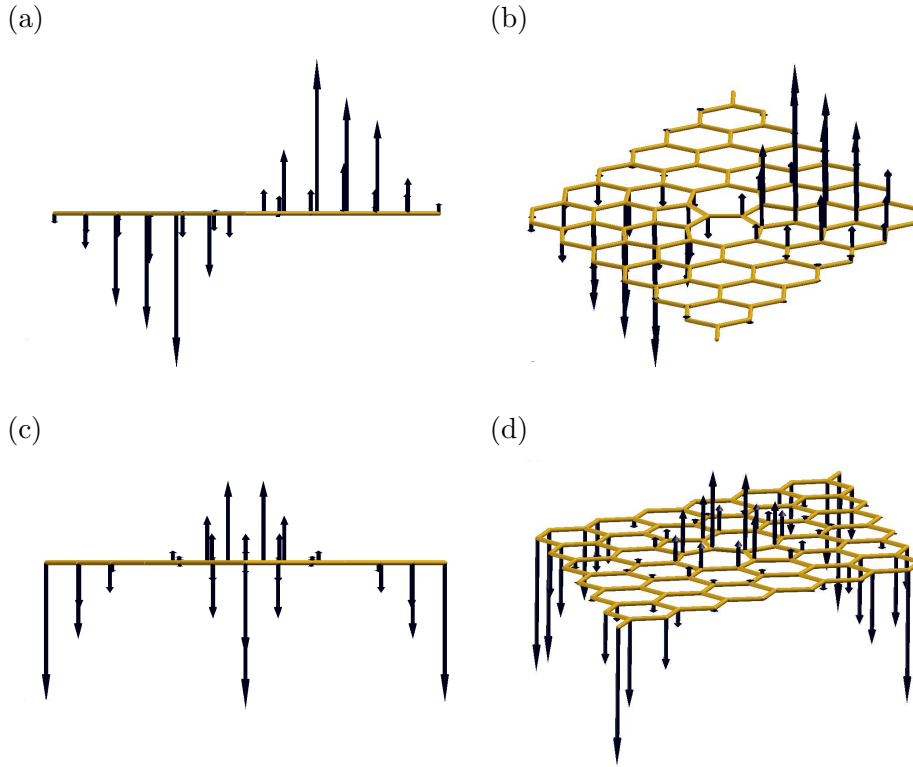


Figure 3.4: Phonon modes that lead to structural instability of graphene with an SW defect (for 2.04 % concentration of defects). (a) and (b) are two views of the atomic displacements of the odd mode with frequency $\approx 65i \text{ cm}^{-1}$. (c) and (d) are two views of the atomic displacements of the even mode with frequency $\approx 53i \text{ cm}^{-1}$. Copyright (2012) by the American Physical Society [39]).

Earlier theoretical study [53] supports our findings of odd and even unstable phonon modes. On freezing in small eigen-displacements of the lower energy unstable mode *i.e.* odd mode followed by structural relaxation, the graphene sheet with SW defect buckles *i.e.* becomes non-planar. The difference in z co-ordinate of positions of the highest and lowest carbon atoms is 1.3 \AA , and the energy gained by buckling is $\approx 280 \text{ meV}$ (*i.e.* 17.6 mJ/m^2 for 7×7 supercell with 1 SW defect). This compares well with the GGA estimate of 253 meV (for 8×8 supercell with 1 SW defect) and 1.40 \AA , as reported in the earlier work [53]. An experimental estimate of the out of plane deformation is $\approx 10 \text{ \AA}$ for suspended

graphene [46]. Our results shows that the rippling behavior associated with SW defects is at a shorter length scale, and with a smaller amplitude (of out of plane deformation). However, the physical origin of ripples due to SW defects or suspended graphene is the same *i.e.*, coupling of out of plane displacement with in-plane strain [47]. In the case of higher defect concentration, *i.e.* one defect in a 5x5 supercell (3x3 supercell), amongst the two unstable modes with odd and even symmetry, the odd mode is more stable than the even mode. Since the two modes differ in frequency by only $6i \text{ cm}^{-1}$ ($9i \text{ cm}^{-1}$), we expect the system ripples through a linear combination of both the unstable modes.

We now present a quasi-continuum analysis that helps (a) understand the origin of these rippling instabilities and (b) explore if they survive in the infinite size limit. In the continuum limit, the buckling arises out of the coupling between optical modes and strain fields. Let o_x , o_y , o_z and a_x , a_y , a_z represent displacements of atoms in a C-C bond associated with optical and acoustic modes in the x, y and z directions respectively (see Figure 3.2a). A linear combination of o_x and o_y displacements of carbon atoms represent the bond rotation that gives an SW defect (see Figure 3.6a). The strain $\epsilon_{\alpha\beta}$ that preserves the invariance of hamiltonian under rigid body rotation of a 2D sheet is given as [51],

$$\epsilon_{\alpha\beta} = \frac{1}{2} \left(\frac{\partial a_\alpha}{\partial x_\beta} + \frac{\partial a_\beta}{\partial x_\alpha} + \frac{\partial a_z(\mathbf{r})}{\partial x_\alpha} \frac{\partial a_z(\mathbf{r})}{\partial x_\beta} \right), \quad (3.2)$$

where $\alpha, \beta = x, y, z$.

Using symmetry, energy of the coupling between strain (acoustic modes) and optical is given by,

$$H(o - \epsilon) = \iint dx dy [g_1(o_x^2(\mathbf{r})\epsilon_{xx}(\mathbf{r}) + o_y^2(\mathbf{r})\epsilon_{yy}(\mathbf{r})) + g_2(o_y^2(\mathbf{r})\epsilon_{xx}(\mathbf{r}) + o_x^2(\mathbf{r})\epsilon_{yy}(\mathbf{r})) \\ + 4g_3 o_x(\mathbf{r})o_y(\mathbf{r})\epsilon_{xy} + g_4 o_z^2(\mathbf{r})(\epsilon_{xx}(\mathbf{r}) + \epsilon_{yy}(\mathbf{r}))]. \quad (3.3)$$

Since o_x and o_y are non-zero for a system with SW defect, a part of the first term gives,

$$g_1 o_x^2 \left(\frac{\partial a_z(\mathbf{r})}{\partial x} \right)^2. \quad (3.4)$$

For a wave with wave vector ‘ \mathbf{q} ’,

$$a_\alpha(\mathbf{R}) = e^{i\mathbf{q}\cdot\mathbf{R}}\epsilon_\alpha,$$

where ϵ the eigen-vector of the acoustic mode and \mathbf{R} is the supercell lattice vector. In the long wavelength limit,

$$o_x^2 \left(\frac{\partial a_z(\mathbf{r})}{\partial x} \right)^2 = g_1 o_x^2 q^2 a_z^2, \quad (3.5)$$

$$o_x^2 \left(\frac{\partial a_z(\mathbf{r})}{\partial x} \right)^2 = \frac{1}{\lambda^2} g_1 o_x^2 a_z^2, \quad (3.6)$$

where λ is the wavelength and $q = \frac{2\pi}{\lambda}$. The parameter g_1 is proportional to the change in frequency of o_y or o_x mode with ϵ_{yy} or ϵ_{xx} strain in pristine graphene. From first-principles calculation we get, $g_1 \approx -0.99 \text{ eV}/\text{\AA}^2$. Since $g_1 < 0$, we see that the G band (o_x and o_y) softens with in-plane strain (equation 3.6). In the long wavelength limit, it represents the out of plane deformation of graphene due to SW defect, *i.e.* the flexural mode which becomes unstable. Thus, coupling between optical modes and inplane strain in the system leads to rippling of graphene in the presence of SW defect.

Earlier works [62–65] report spatial confinement of electrons in graphene due to strain induced strong pseudo-magnetic fields. A similar effect of pseudo-magnetic field is expected from the rippling of graphene with an SW defect due to in-plane strain (equation 3.3), which too gives rise to a pseudo-magnetic field (B_{ps}). We use the formulation of Kim *et. al.* [65] to estimate the magnitude of B_{ps} produced by the out of plane rippling of graphene. We approximate the deformation field (s_z) associated with the odd mode (refer to Figures 3.4a and 3.4b) as follows,

$$s_z(x, y) = a_o \exp\left(-\frac{y^2}{\sigma_y^2}\right) \sin(qx), \quad (3.7)$$

where σ_y gives the extent of localization of the ripple, along direction perpendicular to the direction of the rotated C-C bond at the center of the defect (*i.e.* ‘y’ direction or

the heptagonal axis), and a_o is the maximum out of plane displacement of carbon atoms (0.7 Å). We have used σ_y to 7 Å, the distance between the opposite vertices of the two heptagons along the direction perpendicular to the rotated C-C bond at the centre of the SW defect (refer to Figure 3.4b). q is the wave vector associated with the periodicity of the deformation along the direction of the rotated C-C bond at the center of the defect (*i.e.* ‘x’ direction or the pentagonal axis), and directly proportional to the square root of concentration of SW defects in graphene. The pseudo-magnetic field is given by,

$$B_{ps}^z(x, y) = \frac{t\beta}{e v_F} \left(\frac{2a_o^2 e^{-\frac{2y^2}{\sigma_y^2}} q^2 y \cos^2(qx)}{\sigma_y^2} + \frac{4a_o^2 e^{-\frac{2y^2}{\sigma_y^2}} y \sin^2(qx)}{\sigma_y^4} - \frac{8a_o^2 e^{-\frac{2y^2}{\sigma_y^2}} y^3 \sin^2(qx)}{\sigma_y^6} + 2a_o^2 e^{-\frac{2y^2}{\sigma_y^2}} \frac{q^2 y}{\sigma_y^2} (\cos^2(qx) - \sin^2(qx)) \right). \quad (3.8)$$

Here $t= 2.8$ eV is the electron hopping energy between the nearest π orbitals, and $\beta \approx 2-3$ is a dimensionless coupling parameter [65] for the lattice deformation. v_F is the Fermi velocity and e the electronic charge. Thus, B_{ps} produced by the buckling is proportional to the concentration of SW defects, *i.e.* inversely proportional m^2 (m is the supercell size). For supercells of size greater than $m= 25$ (low defect concentrations), the value of $1/m^2$ becomes small and peak value of B_{ps} becomes a constant. Also, the maxima of the pseudo-magnetic field shifts to the pentagonal axis located half way between the two adjacent defects for low concentration of SW defects, from the heptagonal axis for high concentrations. Our estimate of the peak value of B_{ps} for defect concentrations of $\approx 10^{11} \text{cm}^{-2}$ is approximately 65 Tesla, comparable to the B_{ps} in a nanobubble of length 4 nm and height 0.5 nm which is of the order of 100 T [62].

3.1.4 Electronic Signatures of SW Defects

On comparing the electronic density of states (see Figure 3.5) of pristine graphene with that of graphene with SW defects, it is clear that SW defects give rise to a defect band ≈ 0.5 eV above the Fermi level [66]. The width and height of this band is dependent on the

concentration of defects in the sample. The p_z orbitals of the carbon atoms of the rotated C-C bond at the centre of the SW defect, contribute predominantly to this defect band. With increasing defect concentration, both the density of states and the width of the defect band increase. This defect band is hence useful for the experimental characterization of SW defects, and their concentration in graphene.

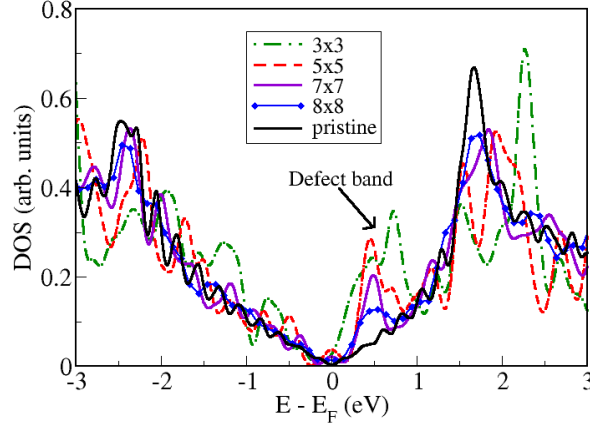


Figure 3.5: Electronic density of states (DOS) of graphene with an SW defect per $m \times m$ periodic supercell (for varying concentration of defects). The defect band due to SW defect is at ≈ 0.5 eV above the Fermi level. The width and density of states of the defect band increases with increasing SW defect concentration. The DOS for different supercells with varying sizes is scaled to that of 1×1 supercell. Copyright (2012) by the American Physical Society [39]).

Previous studies report opening of a band gap with the inclusion of SW defect in 4×4 [54] and 5×5 [55] supercells of graphene, and is contradictory to our finding of zero band gap for the same supercells. We have therefore carried out a detailed investigation of the electronic structure of graphene with an SW defect for varying supercell sizes (ranging from 3×3 to 8×8 unit cells). Due to BZ folding, the sizes of supercells fall under three categories: $(3m) \times (3m)$, $(3m+1) \times (3m+1)$ and $(3m+2) \times (3m+2)$ where m is an integer. We label supercells as $3m$, $3m+1$ and $3m+2$. We refer to k -points in the unit cell BZ with subscript ‘uc’ and k -points in the supercell BZ with subscript ‘sc’. High symmetry K_{uc} and K'_{uc} -points fold onto Γ_{sc} in the case of $3m$ -supercell. For $3m+1$ and $3m+2$ supercells, the (K_{uc}, K'_{uc}) fold onto (K_{sc}, K'_{sc}) and (K'_{sc}, K_{sc}) points respectively.

The SW defect potential ($V_{SW}(\mathbf{r})$) is defined as,

$$V_{SW}(\mathbf{r}) = V_{SW}^{KS}(\mathbf{r}) - V_{pristine}^{KS}(\mathbf{r}), \quad (3.9)$$

where $V_{SW}^{KS}(\mathbf{r})$ and $V_{pristine}^{KS}(\mathbf{r})$ are the Kohn-Sham potentials of graphene with and without SW defect respectively. Due to periodic boundary conditions, $V_{SW}(\mathbf{r})$ is periodic with the supercell *i.e.*

$$V_{SW}(\mathbf{r}) = \sum_{\mathbf{G}_{sc}} V_{SW}(\mathbf{G}_{sc}) e^{i\mathbf{G}_{sc} \cdot \mathbf{r}}, \quad (3.10)$$

where \mathbf{G}_{sc} is the reciprocal space lattice vector of the supercell. Since an SW defect is anisotropic, it breaks the symmetry of the lattice, which is reflected in the electronic energy states. Effects of the SW defect potential on the electronic states can be estimated through perturbation theory. Since we are interested in the possible opening of a gap, we focus on the degeneracy at the Dirac point. The first order correction to the energy of degenerate electronic states with wave vectors \mathbf{q} and \mathbf{q}' is given by,

$$\Delta E^{q,q'} = \langle u_{\mathbf{q}} e^{i\mathbf{q} \cdot \mathbf{r}} | V_{SW}(\mathbf{r}) | u_{\mathbf{q}'} e^{i\mathbf{q}' \cdot \mathbf{r}} \rangle, \quad (3.11)$$

$$\Delta E^{q,q'} = \langle u_{\mathbf{q}} | \sum_{\mathbf{G}_{sc}} V_{SW}(\mathbf{G}_{sc}) e^{i(\mathbf{G}_{sc} - (\mathbf{q} - \mathbf{q}')) \cdot \mathbf{r}} | u_{\mathbf{q}'} \rangle, \quad (3.12)$$

where $u_{\mathbf{q}}(\mathbf{r})$ is the cell periodic part of the Bloch function of the supercell. $\Delta E^{q,q'}$ is non-zero iff $(\mathbf{q} - \mathbf{q}')$ is a reciprocal lattice vector belonging to the supercell. For a pristine 3m supercell the K_{uc} and K'_{uc} -points fold onto Γ_{sc} -point, hence the Dirac cone appears at Γ_{sc} . When $(\mathbf{q}, \mathbf{q}') = (K_{uc}, K'_{uc})$, $\mathbf{q} - \mathbf{q}' = \Gamma_{sc} - \Gamma_{sc} = \mathbf{0}$. Hence, $\Delta E^{\Gamma_{sc}, \Gamma_{sc}} \neq 0$ by symmetry and the degeneracy at the Dirac point breaks. The two degenerate bands thus have energies $E \pm \Delta E$, opening a gap of ≈ 0.288 eV (≈ 0.01 eV) in 3x3 (6x6 supercells) (see Figures 3.6c and 3.6f) at Γ_{sc} .

For 3m+1 and 3m+2 supercells, the K_{uc} -point folds onto K_{sc} and K'_{sc} -points respectively. Here, $(K_{uc} - K'_{uc}) = \pm (K_{sc} - K'_{sc})$, is not a reciprocal lattice vector of the 3m+1 or 3m+2 supercell. Therefore, $\Delta E^{K_{uc}, K'_{uc}}$ is zero for these two cases, *i.e.* there exists no

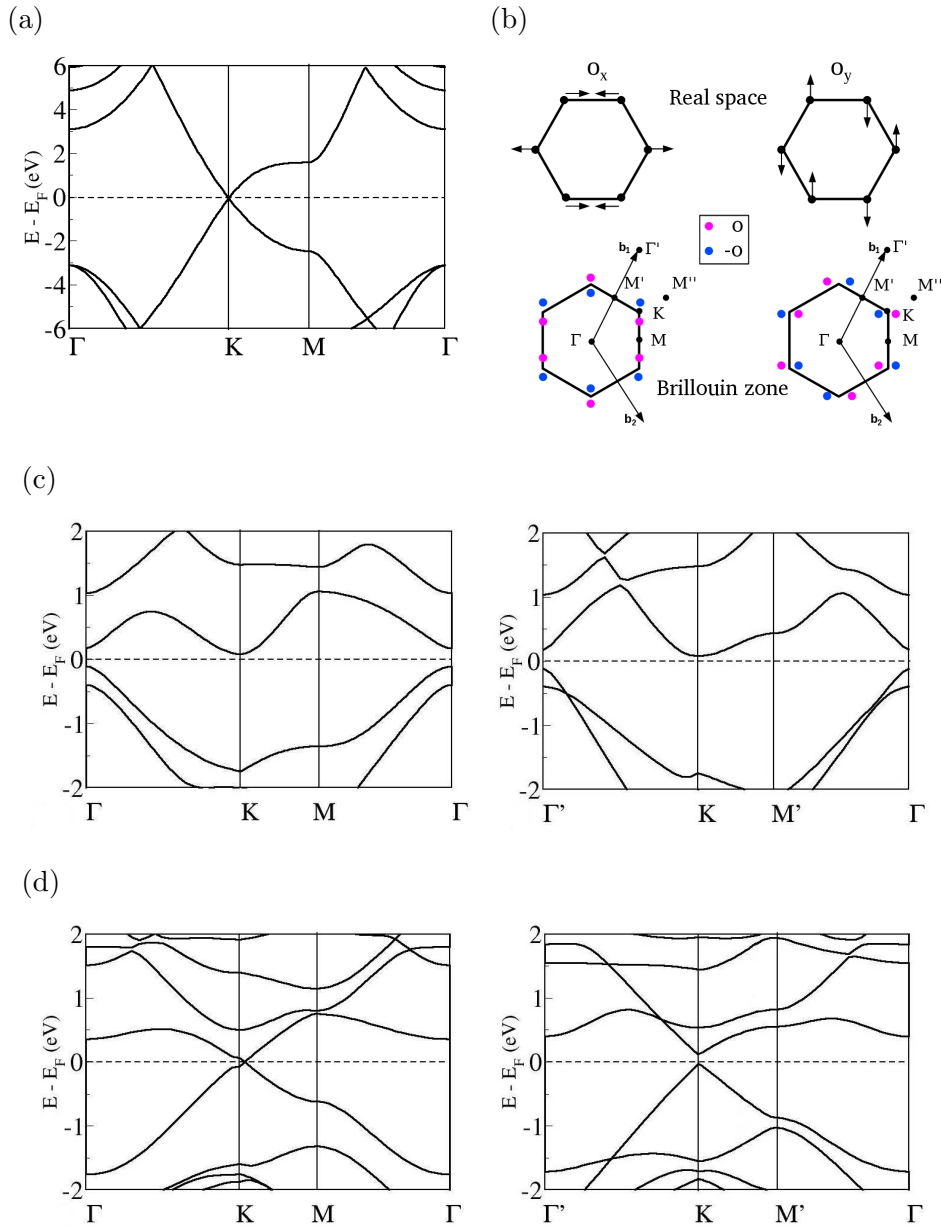


Figure 3.6

coupling between the degenerate states at K_{sc} and K'_{sc} -points. This implies that no gap opens at the Dirac points in the electronic structure of graphene with SW defect in these supercells. However there is a shift in the Dirac points from K_{sc} in the BZ to $K_{sc} \pm \delta k_{sc}$, corresponding to opening of a gap at K_{sc} that closes at $K_{sc} \pm \delta k_{sc}$. We now determine its origin in the structure of the SW defect. The coupling of electronic states at the Fermi level of graphene with its Γ -point phonon modes [67, 68], and lead to the observed shifts

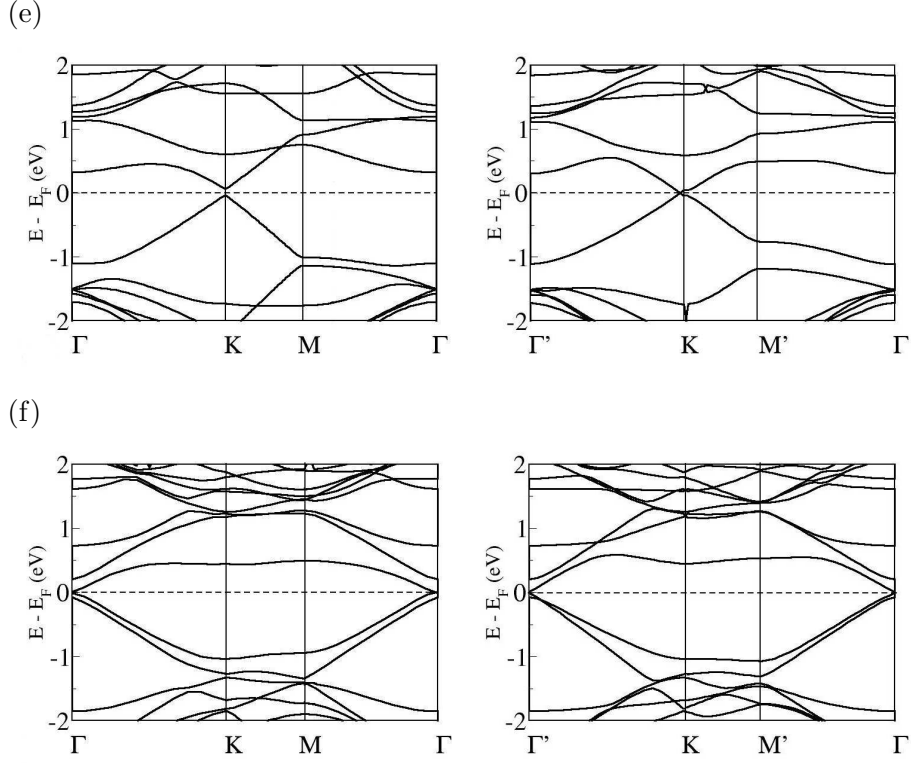


Figure 3.6

in the Dirac cone from K to $K_{sc} \pm \delta k_{sc}$. The 90° bond rotation involved in the formation of SW defect can be expressed as a linear combination of Γ -point phonon modes (localized to a unit cell) of pristine graphene as mentioned earlier, with optical modes o_x and o_y (see Figure 3.6b) giving non-zero contribution. This coupling of o_x and o_y displacements associated with an SW defect with electronic states at the Fermi level lead to a shift in the Dirac points. However o_y displacement opens up a gap at the shifted Dirac point. The shifts are shown in Figure 3.6b by pink and blue dots. Magnitude of the shift is proportional to the SW defect potential V_{SW} [69], *i.e.* the deformation potential of o_x and o_y modes.

Though the SW defect breaks the rotational symmetry in the system, the reflection symmetry $\bar{y}z$ and $x\bar{y}z$ are still preserved (with the origin at the centre of the rotated bond). While the reflection symmetry is retained by the o_x mode, it is broken by the o_y mode (in Figure 3.6b lower panel, refer to only the pink (light grey) or blue (dark grey) dots). Thus, the Dirac cones shift according to o_x displacements and a gap opens

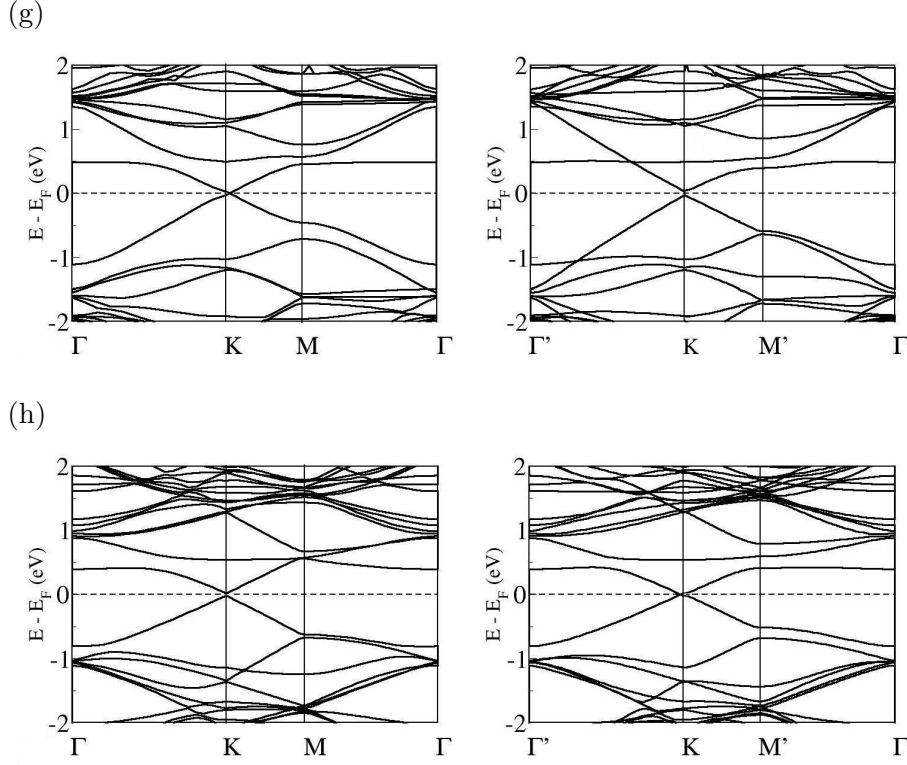


Figure 3.6: Electronic band structure of (a) pristine graphene; shows zero band gap. (b) top panel shows atomic displacements (left o_x and right o_y) and bottom panel shows shift of Dirac points from K and K' -points (left for o_x and right for o_y) in the BZ of the supercell. Pink and blue solid circles correspond to the shift in the Dirac points on the reversal of displacements *i.e.* $\pm o$. Band structure of graphene with SW defect in (c) 3x3 supercell, (d) 4x4 supercell, (e) 5x5 supercell, (f) 6x6 supercell, (g) 7x7 supercell and (h) 8x8 supercell is shown along two different directions in the reciprocal space. Copyright (2012) by the American Physical Society [39].

up at the points corresponding to o_y displacements. Due to difference in BZ folding for $3m+1$ and $3m+2$ supercells, the Dirac cone shifts are opposite in direction for the two cases. $3m+1$ follows pink (light grey) and $3m+2$ follows blue (dark grey) as shown in Figure 3.6b left panel. Since the authors of previous works [54, 55] did not investigate the band structure along these symmetry inequivalent directions in the reciprocal space, the subtlety of anisotropic shifts in the Dirac point was missed. This led the authors to mistakenly conclude opening of a gap in graphene with SW defects. Thus, SW defects lead to opening of a band gap only for a $3m$ supercell, whereas the Dirac cones are shifted from the high symmetry K and K' points in the BZ for $3m+1$ and $3m+2$ supercells.

We also studied the shift in the Dirac cone with concentration of SW defects. Concentration of SW defect was varied by including only one defect per supercell of size 3×3 , 4×4 , 5×5 , 6×6 , 7×7 and 8×8 (see Figures 3.6c to 3.6h). All the three types of configurations $(3m) \times (3m)$, $(3m+1) \times (3m+1)$ and $(3m+2) \times (3m+2)$, are present in these choices of supercells. For configurations with 3×3 and 6×6 supercells containing a SW defect, a gap of ≈ 0.288 eV and ≈ 0.01 eV respectively opens up at Γ_{sc} (see Figures 3.6c and 3.6f). The band gap decreases with decreasing SW defect concentration due to weakening of V_{SW} . For $(3m+1) \times (3m+1)$ supercells, the gap closes along the K to M direction *i.e.* the Dirac cone shifts from K-point towards M-point in the BZ (see Figures 3.6e and 3.6f). On the other hand, the Dirac cone shifts from K-point towards the Γ' -point in the BZ of $(3m+2) \times (3m+2)$ supercell (see Figures 3.6d and 3.6g). We find that the extent of shift δk_{sc} increases with decreasing size of the supercell. For an infinitely large supercell with lattice constant l , the supercell reciprocal lattice vector is given by $2\pi/l$. This implies that the reciprocal lattice vectors are arbitrarily small in length (since $l \rightarrow \infty$), and $\Delta E^{q,q'} \neq 0$ for $(\mathbf{q}, \mathbf{q}') = (\mathbf{K}_{sc}, \mathbf{K}'_{sc})$ (refer to equation 3.12). This implies that a band gap opens up at \mathbf{K}_{sc} , but will be vanishingly small since decreasing defect concentration implies a decreasing band gap. As the rotated bond in the SW defect equivalent to freezing in of the o_x vibrations, the gap will be shifted from \mathbf{K}_{sc} to $\mathbf{K}_{sc} \pm \delta \mathbf{k}_{sc}$ (where $\delta \mathbf{k}_{sc} \rightarrow 0$ as $l \rightarrow \infty$). Thus for an infinitely large supercell with an SW defect, a vanishingly small band gap will open up at $\mathbf{K}_{sc} \pm \delta \mathbf{k}_{sc}$ (where $\delta \mathbf{k}_{sc}$ is infinitesimally small in magnitude).

Our work, along with other works [54, 55], involves a periodic array of SW defects. But in practice, SW defects are randomly distributed in a real sample. While our results should be applicable to determine the effects of randomly distributed SW defects on vibrational spectrum of graphene, our analysis of electronic spectrum needs to be interpreted with care. Each carbon atom in graphene forms three C-C bonds with its nearest neighbours, and the angle between any two C-C bonds is 120° . Depending on which of these three bonds is rotated, the SW defects formed can have three different orientations. All the three orientations of the SW defect lead to shifts in the Dirac points, and the shifts are such that they too are rotated by 120° . When the C-C bond along x axis is rotated by 90° ,

the Dirac point shift is along K-M direction in the BZ (as shown in Figure 3.6b lower left panel). Whereas, the rotation of the other two bonds leads to shift of Dirac points along K-M' and K-M'' directions in the BZ (see Figure 3.6b). Assuming that the SW defect concentration is large enough, a band gap will open up at the K-point for a real sample with all the three orientations of SW defects, and the gap will be shifted towards M or M' or M''-points in the BZ. For a real sample (with non-periodicity arrangement of all three SW defect orientations), a gap is expected to open up at K-point which will reduce and close along K-M or K-M' or K-M'' directions in the BZ.

3.1.5 Conclusions

From first-principles, we have determined signatures of an SW defect in the vibrational and electronic properties of graphene. We showed that the G band gets scattered away by the SW defect and softens, and the D band that is attracted/localized at the defect hardens. Since SW defects are hopping defects, their effects on the Raman spectrum of graphene are enhanced w.r.t. adatoms and vacancies [70]. Hence, the G and D band frequency shifts can be used to characterize SW defects in graphene from Raman spectroscopy.

An SW defect gives rise to two structural instabilities, which are seen in the imaginary frequencies in the phonon spectrum of graphene. The origin of these unstable modes has been identified from our quasi-continuum analysis as the coupling of in-plane optical modes with strain in the system. One of these modes shows out of plane cosine wavelike deformation and the other shows sine wavelike deformation. These instabilities are shown (using a quasi-continuum model) not to vanish in the infinite size limit, and be responsible for the intrinsic rippling of graphene due to SW defects.

Previous studies SW defects involving their effects on the electronic structure of graphene were carried on systems with $3m+1$ [54] and $3m+2$ [55] supercells. Since the symmetry non-equivalent directions in Brillouin zone were inadequately explored, these studies were misled to conclude a band gap opening. We find (a) opening of a band gap for $3m$ supercells, and (b) a vanishing band gap with shifted Dirac point in the BZ of $3m+1$ and $3m+2$ supercells. Our study highlights the subtlety in the electronic structure of graphene with

an SW defect due to its anisotropy. Our analytical and computational studies prove that effects of SW defects on electronic structure of graphene are dependent on the supercell size and the orientation of the SW defect. A defect band arises in the electronic structure of graphene about 0.5 eV above the node of the Dirac cone. The width and density of states of this defect band increase with increasing concentration of defects, and hence can be used for experimental characterization of SW defects in graphene.

3.2 Graphene- Boron Nitride (C-BN) [†]

3.2.1 Introduction

To make graphene a zero band gap semiconductor with high carrier mobility ($\sim 10,000$ cm²/Vs) at room temperature [40], suitable for use in transistors, it is desirable to open up a band gap [72]. A solid solution of hexagonal BN (h-BN) and graphene results domains of BN in the matrix of graphene [73, 74], and subsequently in interesting changes in its electronic properties [75] such as band gap opening. The size, shape and interfaces (zigzag or armchair) made by BN domains with graphene, critically determine the properties of the C-BN. Zigzag (ZZ) interface of C-BN has localized edge states at the graphene edge, which are absent in armchair (AC) interfaces. Due to the electric field arising from the polarity of a BN domain, these edge states conditionally give rise to half metallicity in graphene [76]. Hence, we study variation in the band gap with different concentrations of h-BN for both zigzag and armchair interfaces.

Ribbon-like domains of BN embedded in the graphene matrix making AC interfaces are non-magnetic (NM). Whereas, similar ribbon-like domains of BN making ZZ interface with graphene are anti-ferromagnetic (AFM) half-metals when the number of zigzag chains of BN are ≥ 6 and, the number of zigzag chains of C are ≤ 8 [76]. Due to a slight mismatch between the C-C and B-N bond lengths, we expect that defects are likely to form at the C-BN interface. This is interesting because a common known SW defect does not form readily in h-BN. One of our goals here is to assess whether a topological defect such as

[†]This work has been published in part in Journal of Materials Chemistry A. [71]-Reproduced by permission of The Royal Society of Chemistry (2013).

an SW defect can form possibly at the interface of graphene and BN (C-BN). To study the effects of SW defects on both non-magnetic (SC1) and magnetic (SC2) configurations, we have considered two supercells with varying widths of graphene and BN stripes. Since the defect states typically arise at the Highest Occupied Molecular Orbital (HOMO) and Lowest Unoccupied Molecular Orbital (LUMO), and get localized to the SW defect, we expect these defect sites to adsorb gases effectively. To this end, we study the efficacy of such interfacial SW defect sites to adsorb CO₂ and CH₄ gas molecules.

In this chapter, we explore the changes in (a) electronic structure of graphene doped with varying concentration of h-BN, (b) structural and electronic changes accompanied by SW defects at ZZ and AC interfaces, and (c) the gas adsorption capability of C-BN with SW defects.

3.2.2 Computational Methods

See section 3.1.2 for details of the first-principles calculations. Here, we employed the Local Density Approximation (LDA) [1] with Ceperley- Alder functional for exchange correlation energy [77].

For the AC interface, unit cell of SC1 consisted of 3 AC chains of graphene and 3 AC chains of BN along y direction. Supercells SC1 and SC2, were constructed by repeating the unit cell 4 times and 5 times along x axis respectively. Brillouin zone integrations were carried out with a 3x3x1 mesh of k-points for both SC1 and SC2. Similarly for the ZZ interface, unit cell of SC1 consisted of 4 ZZ chains of graphene and 4 ZZ chains of BN (both with ZZ edges) and SC2 consists of 5 ZZ chains of graphene and 9 ZZ chains of BN, both along y direction. Supercells SC1 and SC2, were constructed by repeating the unit cell 6 times and 5 times along x axis respectively. Brillouin zone integrations were sampled over a 3x3x1 and 12x5x1 mesh of k-points for SC1 and SC2 respectively. Since magnetic calculations critically depend on the k-point sampling, a large number of k-points were considered for SC2, which shows a stable AFM state without the SW defect.

In simulations of gas adsorption, we include semiempirical dispersion interactions (vdW) within the Grimme [78] scheme, along with a generalized gradient approximation

(GGA) [30] to exchange correlation energy of electrons and ultrasoft pseudopotentials [34] to represent interaction between ionic cores and valence electrons. Supercell SC1 with an AC interface was considered for the gas adsorption study at the SW defects. Integrations over Brillouin zone for SC1 was sampled over a $3 \times 3 \times 1$ mesh of k points.

3.2.3 Chemical ordering of boron and nitrogen atoms in graphene

Monte Carlo simulations [79–81] and recent experiments [82] predict formation of BN domains in graphene. When the ratio of number of boron to nitrogen atoms is ≈ 1 ($B/N=1$), $C_{1-x}(BN)_x$ shows segregation of BN islands in graphene (for carbon rich samples) or graphene islands in BN matrix (for BN rich samples) [71, 80]. For nitrogen rich samples however, carbon atoms get dispersed into the BN lattice [80], favoured by energetically favourable C-N bonds. Depending on the kinetics involved in experimental synthesis of C-BN however, some degree of randomness in chemical ordering of B and N is expected.

Table 3.3: Cohesive energies of SZ and SD for different compositions (with GGA estimates in paranthesis). [71]-Reproduced by permission of The Royal Society of Chemistry (2013).

Concentration (x)	Energy (eV/atom)	
	SZ	SD
0	-9.45 (-8.66)	-9.45 (-8.66)
0.083	-9.45	-9.41
0.166	-9.48 (-8.68)	-9.41 (-8.60)
0.25	-9.52	-9.45
0.333	-9.56 (-8.74)	-9.45 (-8.64)
0.417	-9.60	-9.50
1.0	-9.97 (-9.10)	-9.97 (-9.10)

We have simulated two types of chemically ordered periodic supercells of $C_x(\text{BN})_{1-x}$. In the first one (SZ configuration), we replace zigzag chains of BN by zigzag chains of graphene chains (refer to Figure 3.7d). The chemical ordering in SZ configuration is such that the zigzag chains of BN are adjacent to one another, *i.e.* a zigzag stripe of graphene in h-BN. In the second case (SD configuration), a pair of boron and nitrogen atoms were replaced with two carbon atoms at a time such that they form segregated carbon islands [80] (where the largest domain is $5 \text{ \AA} \times 6 \text{ \AA}$ in size) in BN matrix, which also maintains the stoichiometry, *i.e.* the ratio of B/N= 1.

From the cohesive energies of SZ and SD configurations for different concentrations (see Table 3.3), we conclude that configurations with domains of carbon atoms in h-BN sheet are not as energetically favourable as those with zigzag interfaces between BN and graphene, since the number of energetically less favourable C-N and C-B (where bonds stability is given by $\text{B-N} > \text{C-C} > \text{C-N} > \text{C-B} > \text{B-B} > \text{N-N}$ [81]) are more in the SD configurations. Since interface energy of armchair edge is 0.39 eV/\AA as compared to 0.58 eV/\AA of the zigzag edge, armchair interface is even lower in energy than the zigzag interface between BN and graphene. However, the disorder in the positions of substituted atoms and associated entropy favor formation of graphene domains over zigzag stripes in experimentally synthesized $C_x\text{BN}_{1-x}$ [80].

3.2.4 Variation of band gap with concentration: $C_x(\text{BN})_{1-x}$.

The electronic properties of C-BN are naturally affected by the domain structure. In BN-rich systems, the segregated carbon domains give rise to narrow quantum-dot-type energy bands just above and below the Fermi level in the midgap region of BN. In contrast, nitrogen rich C-BN ($\text{B/N} < 1$) exhibit a narrow half-filled band (disorder band) at the Fermi level. The width of which is dependent upon the disorder associated with carbon atoms in the BN matrix. The width of this disorder band decreases with increase in the ordering of carbon (order corresponds to the formation of a crystalline structure of C atoms) in BN [80].

We have determined the electronic gap as a function of concentration for the two types

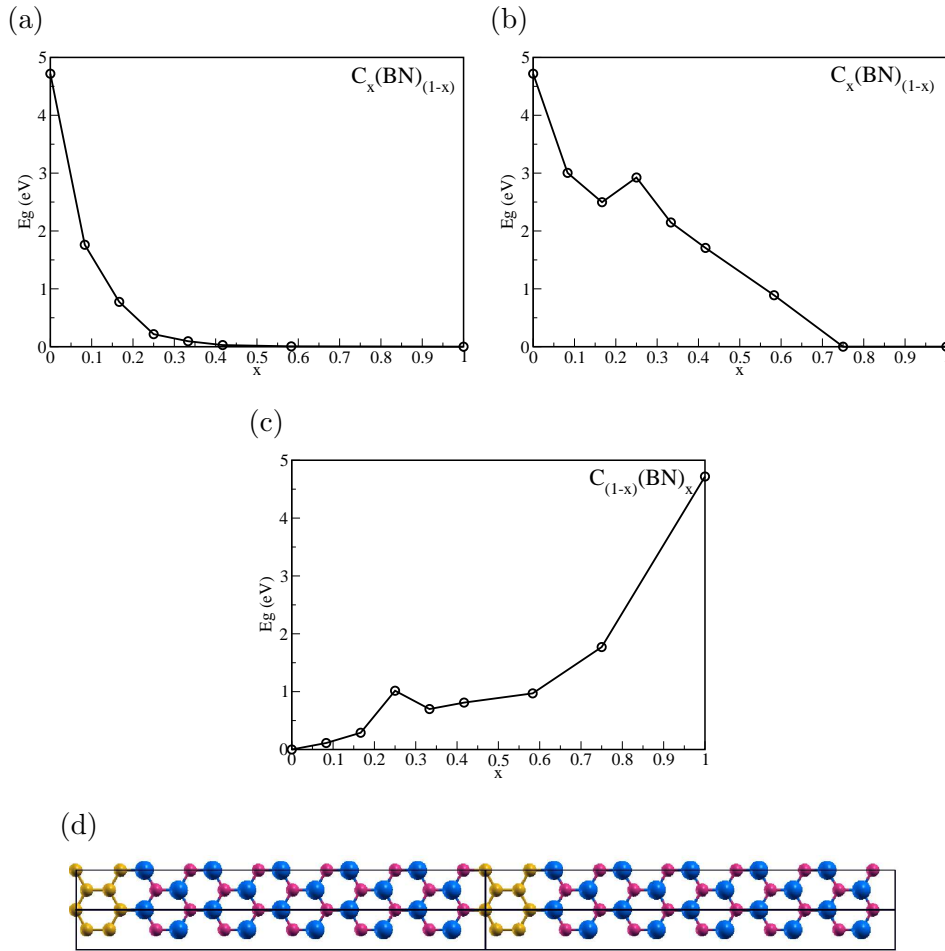


Figure 3.7: Variation of band gap (E_g) of h-BN doped with graphene for different doping fractions (x). (a) and (b) are for SZ and SD configurations respectively. (c) denotes the variation of band gap of graphene doped with BN in the SD configuration, and (d) shows the SZ supercell periodically repeated along x and y directions for C_xBN_{1-x} (the black curve denotes a single SZ supercell). [71]-Reproduced by permission of The Royal Society of Chemistry (2013).

of domain structures (SZ and SD). A polar interface of BN with graphene is formed in the SZ configuration due to the zigzag interface, and the electric field induced by the B and N edges opens a gap between the electronic states at the zigzag edges of graphene [76]. The band gap increases with increasing concentration of BN, as expected. From the calculated band gap of SZ-system with varying concentration of carbon (see Figure 3.7a), we observe that the band gap decreases rapidly as the concentration of graphene (x) increases beyond 0.17. This is because (a) electric field responsible for opening the gap decreases as the

concentration of carbons increases and (b) electronic states of graphene dominate the electronic structure near the fermi level, and percolate.

As compared to the SZ configuration, the decrease in band gap of the SD configuration with x is gradual (refer to Figure 3.7b). The sudden increase in band gap at $x=0.25$ arises from the formation of a six membered hexagonal ring of carbon atoms. A configuration with a domain is more favourable or stable than a random configuration [80], hence exhibits a larger band gap [83]. Similarly, we have simulated graphene lattice with domains of BN (*i.e.* $C_{(1-x)}BN_x$) in the SD configuration (refer to Figure 3.7c). As expected, the band gap vanishes at $x=0$, and increases with increasing concentration of BN, *i.e.* the size of BN domain.

3.2.5 Structure of SW defects at the C-BN interface

An SW defect in C-BN involves an in-plane 90° rotation of a carbon-carbon (C-C), boron-nitrogen (B-N), carbon-boron (C-B) or carbon-nitrogen (C-N) bond, resulting in the formation of a pair of pentagons and heptagons (pair of 5/7 dislocations). Since the formation of an SW defect in pure h-BN is unfavourable, SW defect is more likely to form at the armchair or zigzag interfaces of C-BN.

The hierarchy of energetic stability of the bonds, $B-N > C-C > C-N > C-B > B-B > N-N$ [81] (energy increases from BN to NN), implies that larger the number of B-N and C-C bonds, greater is the stability of the structure. We have used this hierarchy to explain the stability of different types of SW defects at C-BN interfaces. Configurations with armchair interfaces are denoted as ‘AI’ and those with B or N terminated zigzag interfaces by ZIB or ZIN respectively. Since the structure at the interface of SC1 and SC2 configurations is the same, we discuss here bonding and formation energies of various defect configurations only for SC1 (the same arguments work for SC2).

We investigate three configurations of an SW defect with C-C (AI_C), C-B (AI_B) and C-N (AI_N) bond rotations (refer to Figures 3.8a, 3.8b and 3.8c). The formation energy of an SW defect in these three configurations is 4.29 eV, 4.66 eV, 5.66 eV respectively (refer to Table 3.4). Since AI_C has a larger number of C-C bonds, it has greater stability.

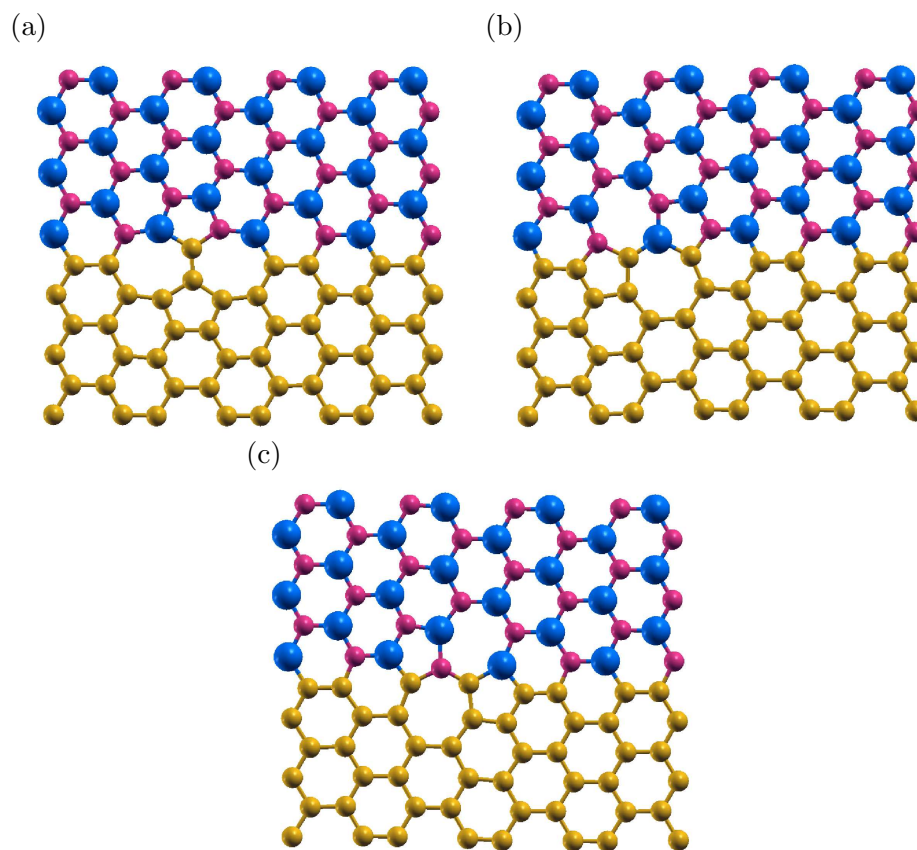


Figure 3.8: Configurations of SW defects at the AC interface. (a) AI_C : C-C bond rotated, (b) AI_B : C-B bond rotated, and (c) AI_N : C-N bond rotated. Colour code: C= yellow, B= blue and N= pink. [71]-Reproduced by permission of The Royal Society of Chemistry (2013).

Though AI_N has more C-N bonds than AI_B , it is less stable since the most stable bond (*i.e.* BN bond) in AI_N and AI_B is stretched by 6.6%, and unstretched relative to its equilibrium bond length respectively (refer to Table 3.5 for bond lengths).

Two configurations at the nitrogen terminated interface are ZIN_N (C-N bond rotated) and ZIN_C (C-C bond rotated) (refer to Figures 3.9a and 3.9b respectively), and the other two configurations at the boron terminated zigzag interface are ZIB_B (C-B bond rotated) and ZIB_C (C-C bond rotated) (refer to Figures 3.9c and 3.9d respectively). The formation energies for ZIN_N , ZIN_C , ZIB_B and ZIB_C are 4.48 eV, 4.34, 5.77 eV and 4.38 eV respectively (refer to Table 3.4). ZIB_C and ZIN_C are more stable than ZIB_B and ZIN_N since they have larger number of C-C bonds at the defect. ZIN_N is more stable than ZIB_B

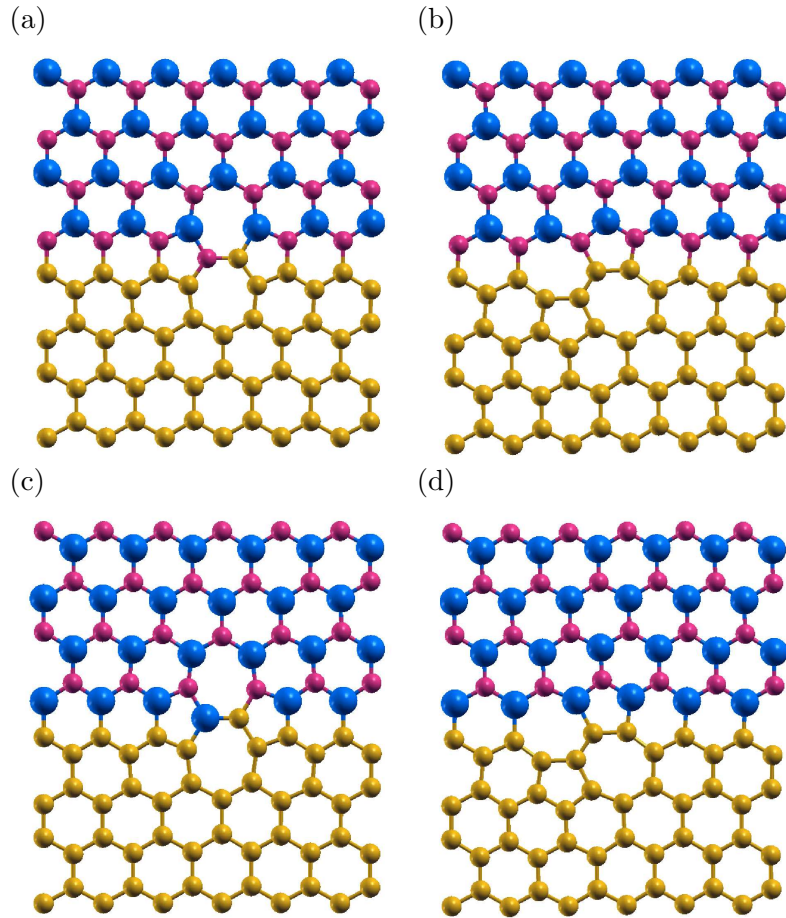


Figure 3.9: Configurations of SW defects at the ZZ interface. (a) ZIN_N : nitrogen terminated C-N bond rotated, (b) ZIN_C : nitrogen terminated C-C bond rotated, (c) ZIB_B : boron terminated C-B bond rotated and (d) ZIB_C : boron terminated C-C bond rotated. Colour code: C= yellow, B= blue and N= pink. [71]-Reproduced by permission of The Royal Society of Chemistry (2013).

since the C-N bond in ZIB_B is stretched by $\sim 6\%$ which leads to increase in the formation energy (refer to Table 3.5 for bond lengths).

The formation energies of SW defect at the C-BN interfaces and graphene are comparable [85] (refer to Table 3.4 for both SC1 and SC2). However, most configurations in SC2 have larger formation energies than that of SC1. The larger number of BN chains in SC2 leads to an increased potential difference across the graphene stripe which in-turn increases the formation energy of an SW defect at the interface (except for ZIB_C and ZIN_C). The bond rotation for ZIB_C and ZIN_C happens inside the graphene sheet, and hence does not drastically affect the B or N terminated edge. Therefore the formation energies of ZIB_C

Table 3.4: Formation energy of SW defect at C-BN interface. [71]-Reproduced by permission of The Royal Society of Chemistry (2013).

Configuration	Formation Energy	
	SC1 (eV)	SC2 (eV)
AI_C	4.29	4.71
AI_B	4.66	5.29
AI_N	5.66	6.02
ZIB_B	5.77	6.34
ZIB_C	4.38	4.04
ZIN_N	4.48	4.92
ZIN_C	4.34	3.94

and ZIN_C are smaller than the other configurations. As for SC1 and SC2, the formation energies of ZIB_C and ZIN_C are smaller in SC2 than in SC1. It can be reasoned that the decrease in the formation energy is due to larger graphene nanoribbon in SC2. Our work shows that the likely presence of SW defects at the C-BN interfaces ($C_{1-x}(BN)_x$) and their stability is determined by the type of bonds involved and the associated strain.

3.2.6 Electronic structure of C-BN interface: effects of SW defects

Band gap opens up in graphene by breaking of its A-B sublattice symmetry. In h-BN, a band gap opens up at the Dirac point due to breaking of this symmetry. As seen earlier, the magnitude of this band gap C-BN and distribution of mid-gap states depend upon the number of B and N atoms doped in graphene [86]. As electron-hole symmetry is preserved due to substitution of equal number of B (holes) and N (electrons) atoms, the electronic states above and below Fermi energy level is nearly symmetric (refer to Figures 3.10a and 3.10b). With excess of N relative to B (or excess of B relative to N) the electron-hole symmetry is broken, and the system becomes n-type (or p-type).

There are electronic states mainly localized at the ZZ edges of graphene, and are

Table 3.5: Bond lengths at the C-BN interface in Å. The equilibrium bond lengths are $d(\text{C-B})= 1.54 \text{ \AA}$, $d(\text{C-N})= 1.34 \text{ \AA}$, $d(\text{C-C})= 1.42 \text{ \AA}$, $d(\text{B-N})=1.45 \text{ \AA}$ [84]. [71]-Reproduced by permission of The Royal Society of Chemistry (2013).

Configuration	SC1				SC2			
	C-B	C-N	C-C	B-N	C-B	C-N	C-C	B-N
AI_C	1.55	1.39	1.31 1.45 1.47	-	1.55	1.39	1.31 1.45 1.47	-
AI_B	1.42 1.53	1.4	1.42	1.45	1.40 1.51	1.41	1.42	1.46
AI_N	1.54	1.29 1.39	1.46	1.55	1.54	1.29 1.39	1.46	1.55
ZIB_B	1.41 1.54	1.42	1.44	1.47	1.40 1.54	1.41	1.44	1.46
ZIB_C	1.57	-	1.33 1.42 1.45 1.46	-	1.58	-	1.34 1.42 1.45 1.48	-
ZIN_N	1.53	1.31 1.39	1.39	1.47	1.52	1.30 1.39	1.40	1.46
ZIN_C	-	1.40	1.33 1.42 1.44 1.46	-		1.41	1.34 1.42 1.43 1.47	-

absent in the AC edges [87]. These edge states give rise to magnetism in graphene nanostructures with ZZ edges [88]. A ZZ graphene nanoribbon has an AFM ground state [89] where the opposite edges have anti-parallel spins, and the system turns half-metallic upon application of an in-plane external electric field [90]. On embedding ZZ graphene nanoribbon between ZZ BN nanoribbon, the potential drop across the B-terminated edge to the N-terminated edge generates an in-plane electric field and the system turns half-metallic, which is determined by a critical number of ZZ chains of graphene (n), and BN (m). Systems with $n \leq 8$ and $m \geq 6$ are expected to show half-metallicity [76]. Hence, SC1 is non-magnetic with a direct band gap, while SC2 is a half-metallic anti-ferromagnet

Table 3.6: Band gaps observed in all the AC and ZZ configurations of SC1 and SC2. [71]-Reproduced by permission of The Royal Society of Chemistry (2013).

Configuration	SC1 (eV)	SC2 (eV)
pristine AC interface	1.3	1.4
AI_C	0.97	1.2
AI_B	1.09	1.2
AI_N	0.24	0.3
pristine ZZ interface	0.4	half-metal
ZI_B	0.25	metal
ZI_C	0.24	metal
ZI_N	0.13	metal
ZI_C	0.2	metal

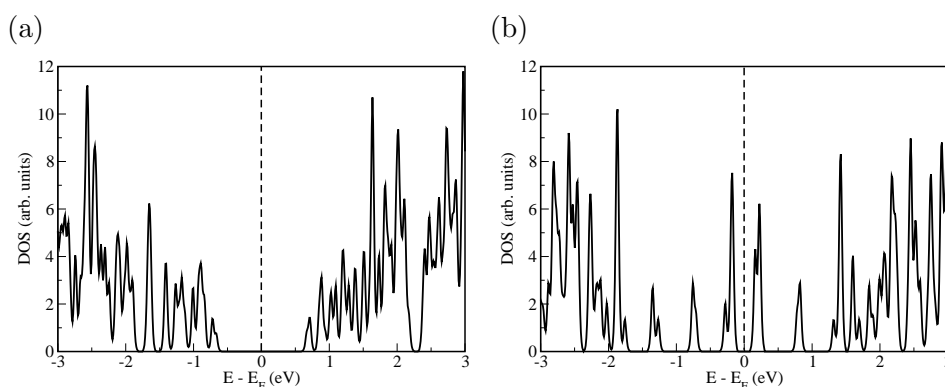


Figure 3.10: Electronic Density of States (DOS) plots for SC1 without SW defect. (a) AC interface (b) ZZ interface. SC1 in (a) consists of 3 AC chains of graphene and 3 AC chains of BN, and 4 ZZ chains of graphene and 4 ZZ chains of BN in (b). [71]-Reproduced by permission of The Royal Society of Chemistry (2013).

(refer to Figure 3.10b and 3.11b).

Now, we present the effects of SW defects on these properties. For SC1, a band gap persists in the system even with the inclusion of a SW defect (refer to Table 3.6). Since all the configurations included here have equal number of B and N atoms, the electron-hole symmetry is preserved (see Figure 3.10) and the conduction and valence band states are symmetrically distributed around the Fermi level. Also, visualization of charge density

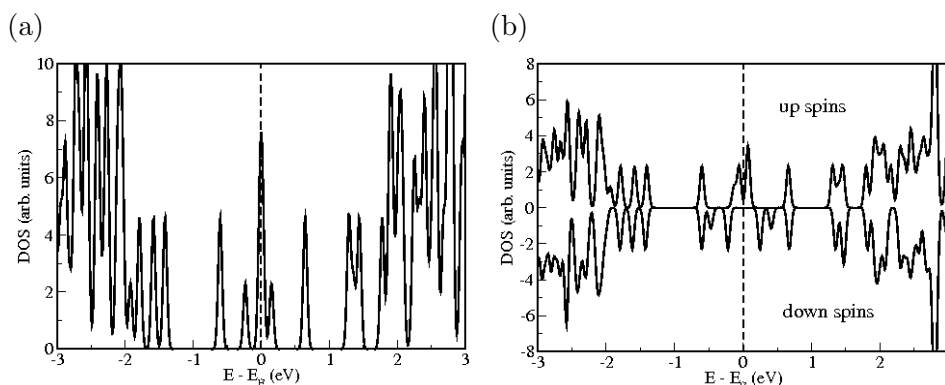


Figure 3.11: Electronic Density of States (DOS) plots for ZZ interface of SC2 without SW defect under the generalized gradient approximation: (a) NM configuration and (b) AFM configuration. The NM configuration is metallic and the AFM configuration is half-metallic. In (b) the up spin and down spin channels are denoted by positive and negative values of DOS respectively. The up spin channel is conducting whereas, there exists a gap in the DOS for down spin channel, making zig-zag interface of SC2 half-metallic. SC2 consists of 5 ZZ chains of graphene and 9 ZZ chains of BN. [71]-Reproduced by permission of The Royal Society of Chemistry (2013).

shows that the states above and/or below the Fermi are localized at the defect (refer to Figures 3.12 and 3.13), making these defects good adsorption sites for ad-atoms and impurities.

All the configurations corresponding to SC1 are non-metallic. We now investigate their charge density distribution for the highest occupied molecular orbitals (HOMO) and lowest unoccupied molecular orbitals (LUMO) (refer to Figure 3.12 and 3.13). In the case of zigzag interfaces without defects, the HOMO and LUMO states are localized at the boron and nitrogen terminated interfaces respectively. At the interface, the ‘p’ orbitals of B, N, and C mix giving rise to four sets of bands which are the bonding and antibonding states between C-B and C-N. The anti-bonding C-N band lies just above Fermi level and the bonding C-B band lies just below it (Figure 3.10), and leads to localization of HOMO and LUMO states at the interface. However with the inclusion of a SW defect, the HOMO state and LUMO states get localized at the defect for ZIB edge and ZIN edge, respectively. The same holds for armchair interfaces. The HOMO and LUMO states get localized at the defect for AI_C , AI_B and AI_N configurations. This localization is more pronounced for AI_N , and leads to higher formation energy of the SW defect.

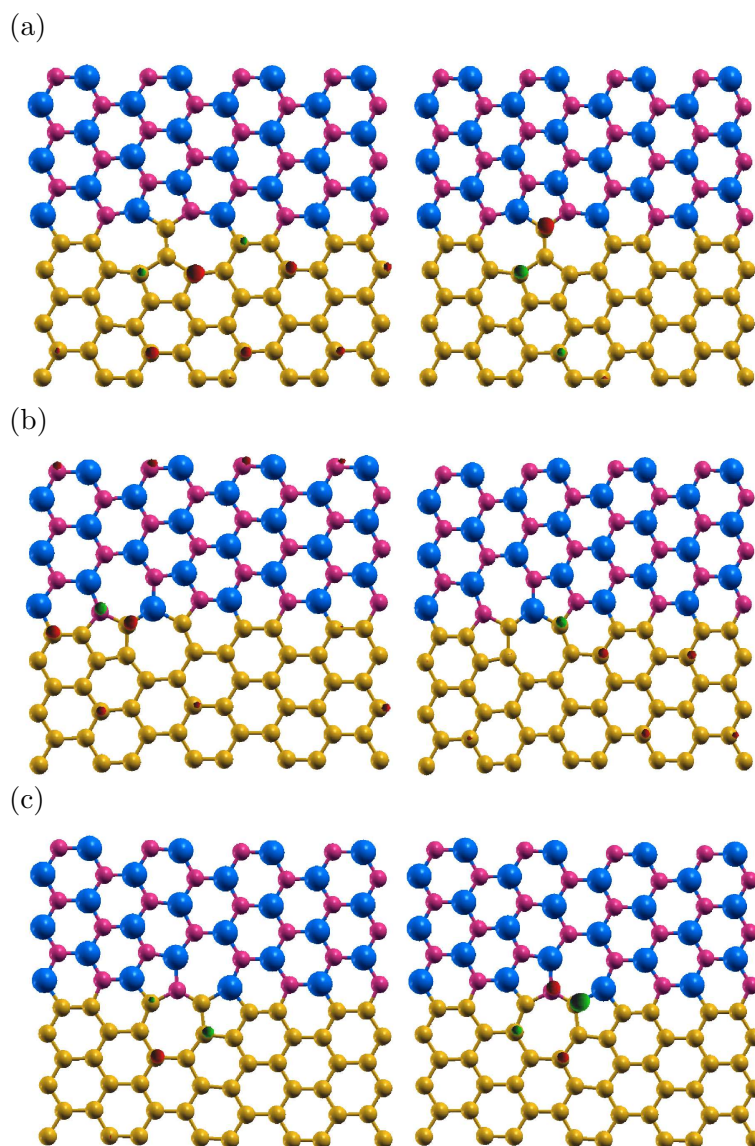


Figure 3.12: Charge density plots of HOMO (left panel) and LUMO (right panel) for configurations (a) AI_C , (b) AI_B and (c) AI_N in SC1. The HOMO and LUMO of all the three configurations are localized to the SW defect. SC1 consists of 3 AC chains of graphene and 3 AC chains of BN. Colour code: C = yellow, B= blue and N= pink. [71]-Reproduced by permission of The Royal Society of Chemistry (2013).

The AC configurations of SC2 type exhibit band gaps in the presence or absence of SW defects. However, the ZZ configuration without a SW defect shows metallic behaviour in the NM state (refer to Figure 3.11a). Due to potential difference generated by the C-N and C-B edges, graphene zigzag nanoribbons embedded in zigzag BN nanoribbons turn half-metallic [76]. In the AFM state, the up spins conduct and down spins show a

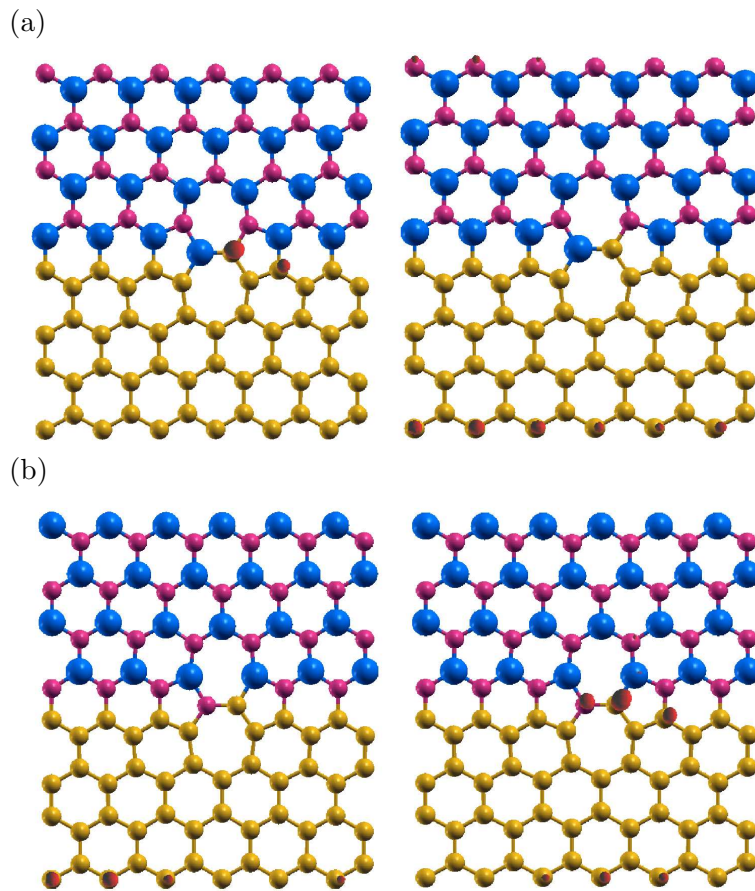


Figure 3.13: Charge density plots of HOMO (left panel) and LUMO (right panel) for configurations (a) ZIB_B and (b) ZIN_N in SC1. The HOMO and LUMO of ZIB_B configuration in (a) are localized to the defect and nitrogen edge respectively. Whereas the LUMO and HOMO of all the ZIN_N configuration in (b) are localized to the defect and boron edge respectively. SC1 consists of 4 ZZ chains of graphene and 4 ZZ chains of BN. Colour code: C= yellow, B= blue and N= pink. [71]-Reproduced by permission of The Royal Society of Chemistry (2013).

finite energy gap in its electronic structure (half-metallicity, refer to Figure 3.11b). The AFM state is 15.4 meV higher in energy than the NM state, and in contrast to previous theoretical calculations [91]. This discrepancy is due to the LDA exchange-correlation energy functional used in our calculations. Our calculations with GGA show that the AFM configuration is 10.1 meV lower in energy than the NM configuration.

To check for magnetic ground states we have initialized the spins of the C atoms parallel (FM) and anti-parallel (AFM) on the opposite edges for all defect configurations. Out of all the defect configurations of SC2 supercell with zig-zag interfaces, only ZIN_N configuration

Table 3.7: Energy and magnetic moments (μ) in the NM, FM and AFM configurations in ZIN_N supercell of 140 atoms. [71]-Reproduced by permission of The Royal Society of Chemistry (2013).

Configuration	Energy (eV/atom)	total μ (μ_B /cell)	absolute μ (μ_B /cell)
NM	-170.36	-	-
FM	-170.36	0.13	0.23
AFM	-170.36	0.04	0.07

converged to both FM and AFM states with negligible magnetic moment per supercell (refer to Table 3.7). However, the energies of the NM and the magnetic configurations are about the same, indicating that the magnetic moment may be an artefact of the calculations. Thus, SW defects annihilate half-metallicity and have a weakening effect on magnetism in C-BN systems.

3.2.7 Gas adsorption studies

Based on experiments, Kumar *et. al.* [71] report energies of adsorption of CO_2 and CH_4 on C-BN is ≈ 14 -19 kJ/mol (at coverage of 7 and 3.7 wt % of CO_2 and CH_4 , respectively). Since the HOMO and LUMO of C-BN are localized to the SW defect, we explore the effects of a SW defect on the gas adsorption capabilities of C-BN. We choose two configurations, AI_C and AI_N in SC1, which have the minimum and maximum formation energies. The adsorption energy (E_{ads}) of CO_2 and CH_4 gas molecules on C-BN was estimated with,

$$E_{ads} = - [E_{Complex} - (E_{C-BN} + E_{Gas})], \quad (3.13)$$

where $E_{Complex}$, E_{C-BN} and E_{Gas} are energies of C-BN and gas molecule complex, C-BN and of an isolated gas molecule respectively. We simulated adsorption of CO_2 and CH_4 gases at various sites near the pentagonal ring of the SW defect.

On the introduction of a SW defect, the C-BN sheet becomes dynamically unstable

and hence it bends [39]. For a planar sheet with SW defect with no symmetry breaking displacement (*i.e.* out of plane deformation) or field (such as a molecule), the system remains planar. However, on the introduction of a gas molecule, the symmetry breaks and the sheet bends. The extent of bending or the height difference between the most displaced atoms is ≈ 1.2 to 1.8 Å, and the energy gained (only due to bending) is 63 kJ/mol. We now consider the adsorption energies w.r.t. the bent C-BN sheet.

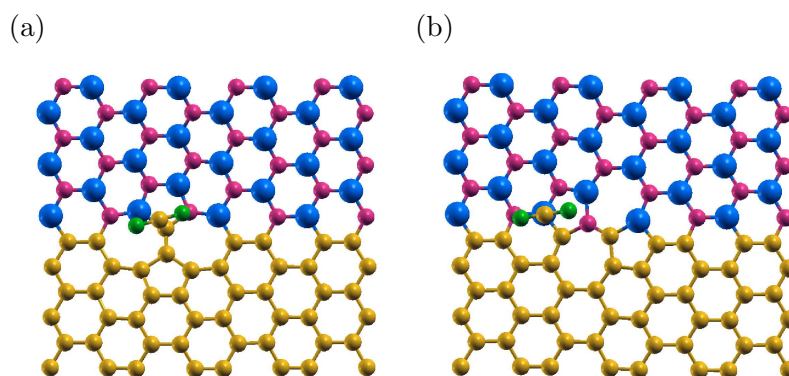


Figure 3.14: Relaxed structures of CO_2 on (a) Al_C and (b) Al_N . Colour code: C = yellow, B= blue, N= pink and O= green. [71]-Reproduced by permission of The Royal Society of Chemistry (2013).

For one CO_2 molecule per cell, which corresponds to ~ 3.6 wt%, adsorption energies are 19 kJ/mol and 22 kJ/mol for Al_C and Al_N configurations respectively (refer to Figure 3.14). The shortest distance of an atom of CO_2 molecule is 3.25 and 3.14 Å respectively for Al_C and Al_N configurations. For a CH_4 molecule (1.35 wt %), the adsorption energies are 34 kJ/mol and 17 kJ/mol with distances between molecule and C-BN sheet of ~ 2.73 Å and 2.75 Å for Al_C and Al_N configurations respectively (refer to Figure 3.15). The adsorption energies of CH_4 and CO_2 at the defect sites are approximately 1.5 times the adsorption energy at a non-defective site. This is because, the electronic states of the molecules interact more strongly with the defect electronic states which are localized in the plane of C-BN, and relatively more extended in the direction perpendicular to the plane (where the molecular states lie).

We note that the contribution of Van der Waals interactions to the adsorption energy is ~ 20 -25 kJ/mol. From the electronic density of states (DOS) of these structures, we

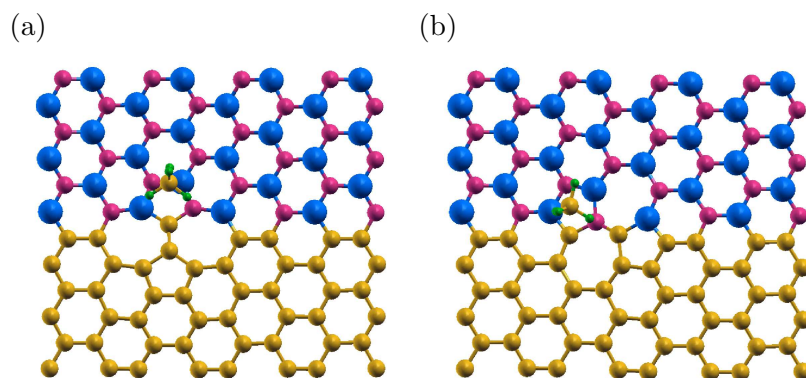


Figure 3.15: Relaxed structures of CH_4 on (a) Al_C and (b) Al_N . Colour code: C= yellow, B= blue, N= pink and H= green. [71]-Reproduced by permission of The Royal Society of Chemistry (2013).

find that the interaction of molecules with the C-BN layer results in the shifting of states that are just above the Fermi level towards it. Since all the configurations with CO_2 and CH_4 show similar trends in the nature of the DOS, we only discuss the interaction of CO_2 with C-BN in the Al_C configuration. From the DOS of C-BN with and without CO_2 (see Figure 3.16), the contribution of the CO_2 molecule to the total DOS is projected out (Figure 3.16, the HOMO states of C-BN+ CO_2 and CO_2 were aligned with the HOMO of C-BN with zero as the Fermi level of C-BN). The binding between CO_2 and the C-BN layer is strong, when the CO_2 molecule is placed near the sites that contribute to the LUMO of Al_C (refer to Figure 3.12a and Figure 3.14a). A noticeable change is observed in the peaks of the bands in C-BN which overlap with those of CO_2 (at ~ 3.5 eV and ~ -5 eV in Figure 3.15), confirming the existence of weak overlap of wavefunctions of CO_2 and C-BN at the SW defect leading to stronger binding and a decrease in the band gap of ~ 0.1 eV for CO_2 on Al_C . This is because the defect electronic states are localized in the plane of C-BN, but relatively more extended in the direction perpendicular to the plane.

3.2.8 Conclusions

We predict the occurrence of SW defects at these interfaces with formation energies ranging from 4 to 6 eV, and comparable to that of a SW defect in graphene. Formation energy of SW defect in ZIN_C and ZIB_C configurations is lower than that in graphene, reflecting

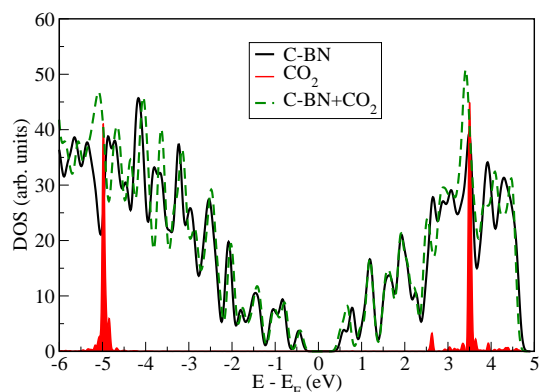


Figure 3.16: Electronic Density of States (DOS) plots for CO_2 adsorbed on the SW defect in the SC1 configuration. Red filled curve (grey) is the projected DOS of CO_2 molecule on C-BN, green (grey) curve is the DOS of C-BN without molecule and black curve is the DOS for C-BN + CO_2 . [71]-Reproduced by permission of The Royal Society of Chemistry (2013).

the strong probability of SW defect formation at the C-BN interface. The variation and trends in the formation energies of SW defects at different interfaces (AC and ZZ) can be understood in terms of the type of bonds involved and associated strain. Secondly, we note that SW defects eliminate or weaken the half-metallic properties of C-BN systems.

We find that the adsorption of CO_2 and CH_4 gases at defects in C-BN is 1.5 times stronger than that at an interface without defects. The adsorption energy of these gases is $\sim 14\text{-}34$ kJ/mol (at coverages of 3.6 and 1.35 wt % of CO_2 and CH_4 , respectively) for C-BN with SW defects, as compared to 14-19 kJ/mol (at coverage of 7 and 3.7 wt % of CO_2 and CH_4 , respectively) for C-BN interface without defect. Hence, SW defects at C-BN interfaces improve its gas storage capabilities, and should be exploited for enhancement in adsorption efficiencies of these materials.

Chapter 4

Silver

4.1 Stability of 2H polytype *

4.1.1 Introduction

Silver (Ag) in its bulk form has the FCC structure, with (ABCABC...) periodic stacking of its close-packed (111) planes, which is also known as the 3C structure. Polytypes are structures that involve different stacking sequence of these close-packed planes. However, these polytypes differ in their electronic and mechanical properties, and provide diversity to their applications. For eg. silicon carbide has more than 170 known polytypes, among which the important ones (3C, 2H, 4H and 6H) differ in their electronic and optical properties [93,94]. The most commonly observed polytypes of Ag are 4H [95] and 9H [96]. In recent experiments, Chakraborty *et al.* [92] have synthesized an interesting 2H (ABAB...) polytype of silver with anomalously large inter-planar spacing (almost 35% larger than the one in its bulk FCC phase). We use first-principles calculations to investigate stability of this reported 2H structure with lattice parameters $a= 2.83 \text{ \AA}$ and $c= 6.38 \text{ \AA}$. We have assessed the local stability of this 2H polytype through determination of phonon dispersion and estimated a critical uniaxial tensile strain above which the structure becomes unstable at $T= 0 \text{ K}$. Electronic origin of this can be traced to Peirel's instability emerging

*This work has been published in part in Journal of Physics: Condensed Matter [92]. Copyright (2011) by Institute of Physics (IOP).

at a critical strain indicating that the system would double its periodicity to attain stability. Further, phonon spectra were obtained using SCAILD at $T= 400$ K to check for the stability of the experimentally observed 2H polytype due to anharmonic effects at finite temperature. Based on these, we suggest a possible mechanism of its stability.

4.1.2 Computational Methods

See section 3.1.2 for details of the first-principles calculations. The exchange-correlation energy of electrons was treated within a GGA functional of Perdew Burke Ernzerhof parametrized form [30]. In the investigation of the stability of 2H structure with intercalated oxygen or extended defects, a $4 \times 4 \times 1$ supercell was constructed and the integration over the Brillouin zone were sampled a $3 \times 3 \times 6$ mesh of k-points. The Density Functional Perturbation Theory (DFPT) calculations were carried out for two atoms basis cell with a uniform $6 \times 6 \times 4$ mesh of k-points in self consistent field (scf) calculations, determining the dynamical matrices using DFPT over a mesh of $3 \times 3 \times 2$ k-points. For lattice dynamical analysis at finite temperature, we used the Self Consistent Ab Initio Lattice Dynamics (SCAILD) code of Souvatzis *et al.* [28], interfacing it with QE to obtain phonons using DFPT.

4.1.3 Stability: intercalating impurities?

Since the films studied here are grown in gaseous (N and O) ambiance, we first explore if trapping of any impurities of N or O between two close-packed planes of the 2H polytype (intercalation) can give rise to stability of the observed 2H polytype with the unusually larger inter-planar separation. We use a $4 \times 4 \times 1$ supercell and place impurities (or defects) interstitially far from one another, one above the A plane and the other above the B plane, amounting to an impurity concentration of 6.25%. While this is much larger than that possible in the films in experiments, our goal is to study its effects on the structure noting that they may be overestimated. Use of such a supercell allows us to use a smaller ($3 \times 3 \times 6$) mesh of k-points.

Our simulations with structural relaxation resulted in structures (see Figure 4.1) that

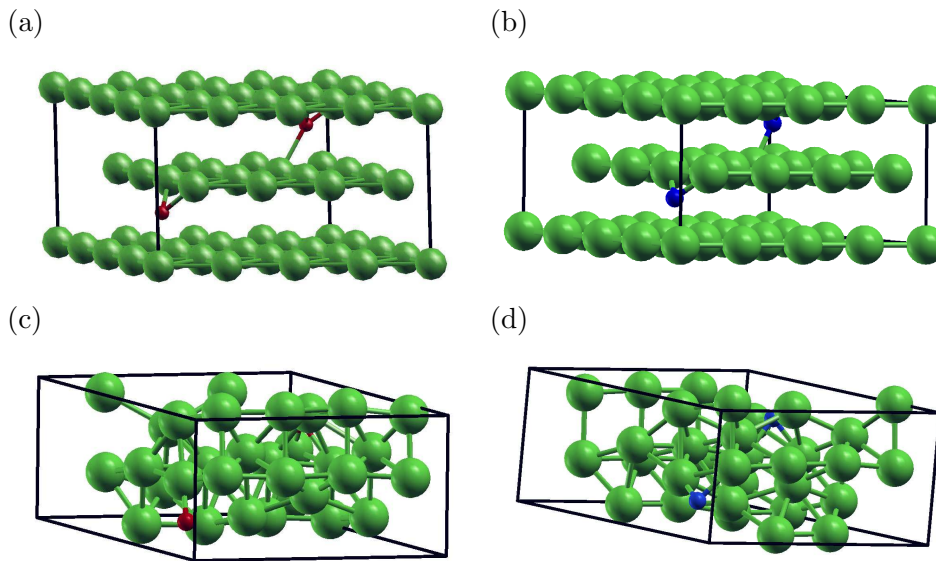


Figure 4.1: Structure of 2H polytype of silver intercalated with oxygen and nitrogen impurities. Structure with (a) O and (b) N impurity before relaxation. Structure with (c) O and (d) N impurity after relaxation. Colour code: Ag= green, O= red and N= blue. Note that the structure distorts completely and loses all the symmetries of 2H after relaxation. Copyright (2011) by Institute of Physics (IOP) [92].

are significantly distorted and have a much lower symmetry than the parent structure of the 2H-polytype. These should have been readily noticed in structural characterization in experiments. Chemically, our results are understandable as each of the close-packed planes of silver when far from each other, would be chemically active and interact with impurities like N and O strongly. Hence, we exclude the possibility of intercalated N and O (or silver) as a possible cause for stability of the 2H structure with anomalous $c = 6.38 \text{ \AA}$.

4.1.4 Thermal Stability

To explore whether the observed 2H structure could be possibly stabilized by thermal fluctuations or vibrational entropy, we undertook SCAILD [28] based calculations of phonon dispersion at $T = 400 \text{ K}$ using a $3 \times 3 \times 2$ supercell of observed 2H polytype. In this mean-field analysis of phonons, the lattice structure is still preserved and renormalized frequencies of phonons are obtained. Such an approach has been successful in showing how a few BCC

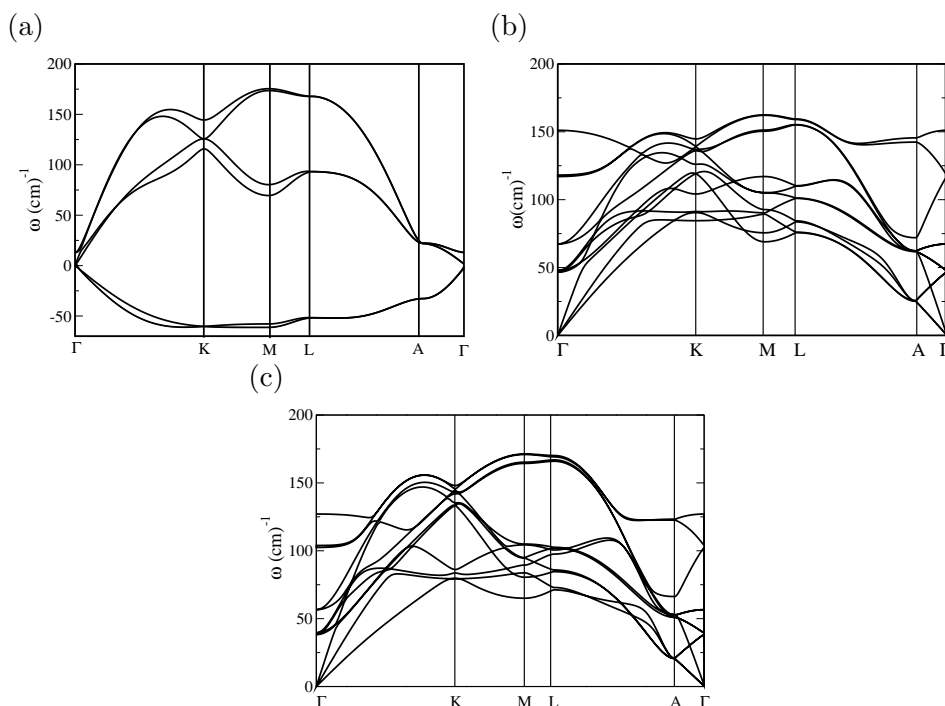


Figure 4.2: Calculated phonon dispersion curves for (a) the 2H polytype of Ag at 400 K. Also shown are calculations at 0 K for the 4H polytype with (b) optimized parameters ($a = 0.292$ nm, $c = 0.967$ nm), and (c) experimental parameters ($a = 0.283$ nm and $c = 1.0$ nm). Copyright (2011) by Institute of Physics (IOP) [92].

metals which are unstable at $T = 0$ K become stable due to thermal entropy at high temperature. Our SCAILD calculations show that the unstable modes (modes with imaginary frequencies) persist in phonon dispersion at 400 K (see Figure 4.2a). A similar analysis at $T = 1000$ K showed imaginary frequencies (unstable modes), suggesting that thermal fluctuations or entropy are not adequate in stabilizing the observed 2H structure.

4.1.5 Local stability of 2H polytype

Finally, we determine the largest inter-planar separation a 2H polytype can have while maintaining its local stability (at 0 K). A structure is locally unstable, if it is not a local minima of energy, *i.e.* any structural distortion through atomic displacements lowers its energy. While the forces on each atom in the relaxed structure vanish within a tolerance, the structure can still be unstable if the second derivative of energy with respect to certain atomic displacements is negative. Precise information of such *unstable* structural

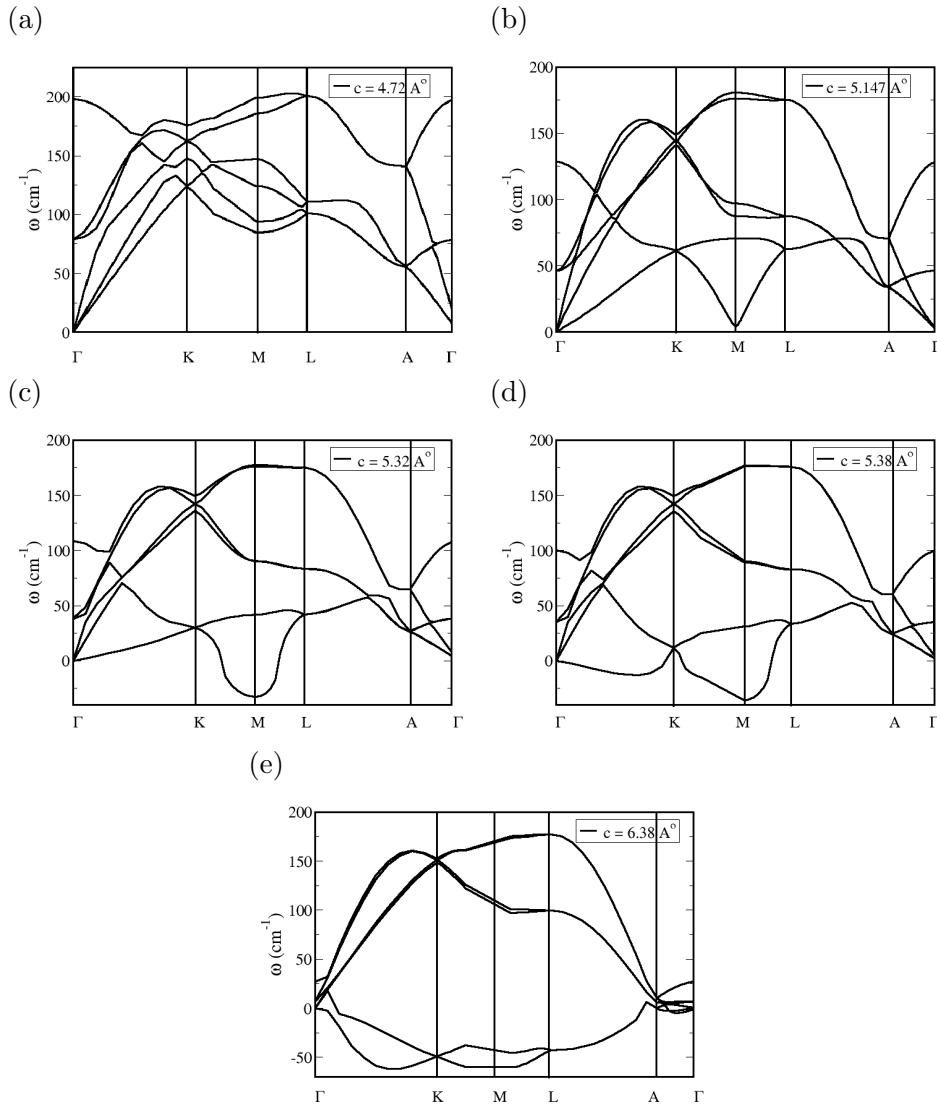


Figure 4.3: Calculated phonon dispersion curves for the 2H polytype of Ag for different values of uniaxial strain (ϵ_{zz}), corresponding to different values of the c-parameter: (a) $\epsilon_{zz} = 0$, $c = 4.72 \text{ \AA}$, (b) $\epsilon_{zz} = 0.09$, $c = 5.147 \text{ \AA}$, (c) $\epsilon_{zz} = 0.13$, $c = 5.32 \text{ \AA}$, (d) $\epsilon_{zz} = 0.14$, $c = 5.38 \text{ \AA}$, and (e) $\epsilon_{zz} = 0.35$, $c = 6.38 \text{ \AA}$. Copyright (2011) by Institute of Physics (IOP) [92].

distortions can be efficiently obtained from phonon dispersion of the structure, in which they manifest as modes with imaginary frequencies $\omega^2 < 0$. This means that the structure is a *saddle point* with respect to atomic displacements corresponding to the unstable mode. Thus, to investigate local stability of the 2H polytype as a function of inter-planar distance, we obtained phonon dispersion of the 2H-polytype as a function of inter-planar separation (see Figure 4.3).

For a fixed in-plane lattice constant a , we changed the interplanar distance amounting to deforming the 2H polytype uniaxially. Phonon dispersion of the 2H polytype as a function of interplanar spacing (d), shows no unstable modes for uniaxial strain (ϵ_{zz}) from 0 ($d = 2.36 \text{ \AA}$) $\leq \epsilon_{zz} \leq 0.09$ ($d = 2.57 \text{ \AA}$). For $\epsilon_{zz} > 0.09$, a transverse optical (TO) branch exhibits an onset of instability (see Figure 4.3b) at M point. At higher strain $\epsilon_{zz} > 0.13$, a transverse acoustic TA branch also becomes unstable (see Figure 4.3c). We find weakly unstable modes in the phonon dispersion of the experimentally observed structure with value of inter planar spacing ($d = 3.19 \text{ \AA}$ and $\epsilon_{zz} = 0.35$, see Figure 4.3e).

Electronic origin of the structural instability can be traced to the Fermi surface of the structure with $d = 2.57 \text{ \AA}$ *i.e.* $\epsilon_{zz} = 0.09$. The Fermi surface is hexagonal (see Figure 4.4a and 4.4b); its two-dimensional nature means there is little bonding across the close packed planes, and hence the structure will not conduct along c -axis. Fermi surface clearly exhibits *NESTING* between its opposite surfaces supporting Peirels instability in the structure. The nesting wave vector corresponds to the M point, which is the wave vector of instability we found above. Structural distortion associated with the unstable M -mode leads to cell doubling along one of its in-plane lattice vector with atomic displacements along z -direction (which alternate in sign in neighbouring unit cells), thus effectively reducing the interplanar distance between A and B planes (see Figures 4.4c and 4.4d) by almost 10 %. Calculated phonon dispersion of this distorted cell-doubled structure using DFPT clearly shows that the instability at M point weakens upon distortion. However, the structure still remains unstable (see Figure 4.4e). We repeated this process of freezing in the distortions of the unstable modes of the structure in Figures 4.4c and 4.4d and find that (a) the instabilities further weaken, and (b) effective interplanar distance reduces, and (c) symmetry of the 2H polytype is reduced to some extent.

4.1.6 Metastability of the 2H polytype

We now present a possible scenario for the metastability of the observed 2H polytype with anomalously large inter-planar spacing. The analysis of in-plane phonon modes at

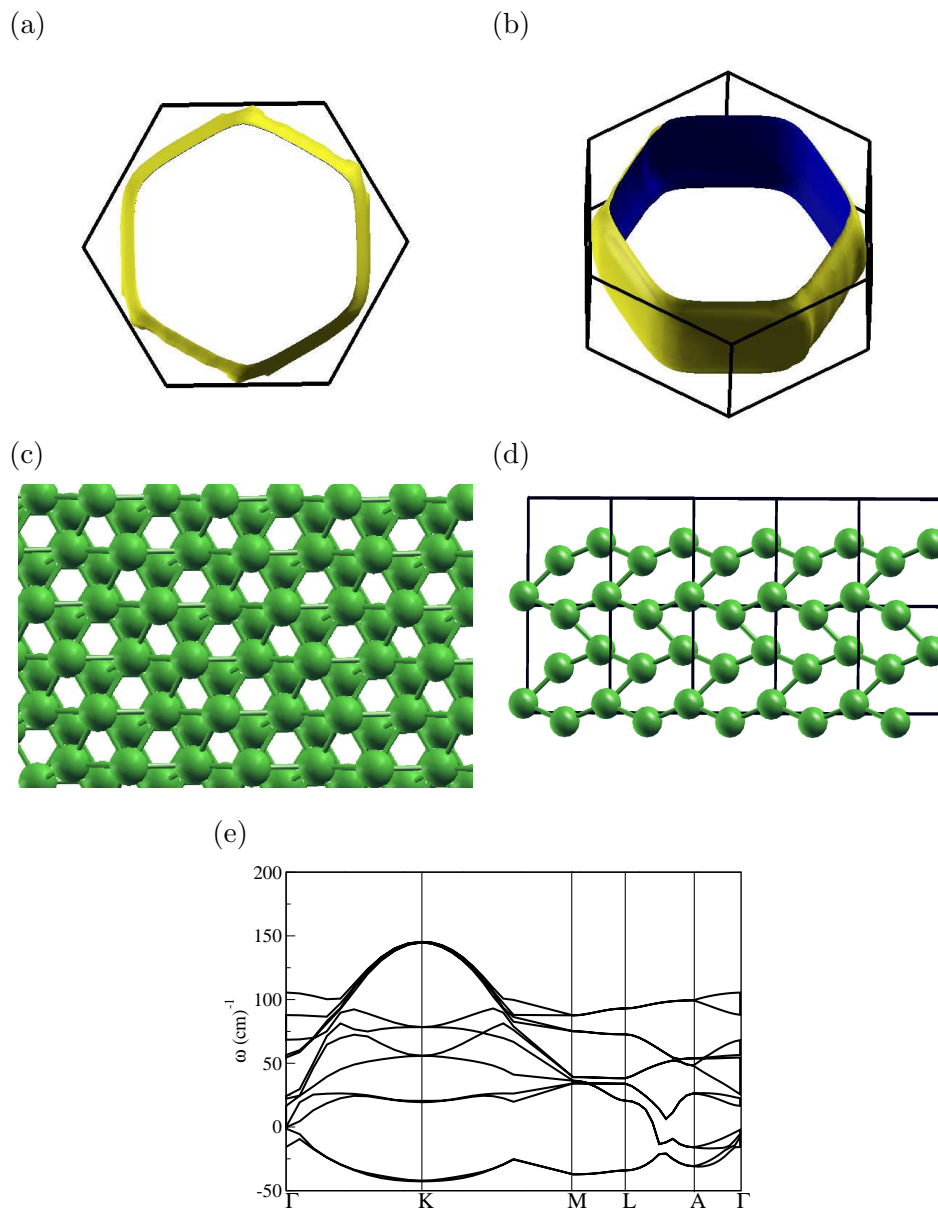


Figure 4.4: Views of the Fermi surface (a) from the top, and (b) at an angle, clearly indicate flat surface nesting. (c) Top view, and (d) side view of the lattice distorted by M point phonon that conserves AB stacking symmetry. The distortion in the z-direction leads to a reduction in the spacing between the A and B planes. (e) The phonon dispersion of the crystal lattice distorted by the M point phonon mode. Copyright (2011) by Institute of Physics (IOP) [92].

the M point of the 2H polytype, reveals that the modes remain hard or harden with increasing inter-planar spacing (d), reflecting an increased strength of in-plane bonding among the atoms (see Figure 4.3). On the other hand, the modes with out-of-plane atomic

displacements soften rapidly as d increases, and their band width at the Γ -point reduces from 10 meV in the optimized structure to just 3 meV in the observed structure. As pointed out earlier, the structural instability is led by the z-polarized modes at M point and followed by the modes at K and L points, while those at A point remain stable. Since, M and K points lie in the ‘ab’-plane, and L and A out of it, this reflects also on the 2D nature of the region in the Brillouin zone in which structural instabilities develop. Hardening of the modes with in-plane displacements and softening of the others can be understood in terms of strengthening of in-plane bonds, while the instabilities at the M point arise from Fermi surface nesting.

As thermodynamic arguments based on the vibrational contribution to free energy, possible structural distortions and impurity intercalation cannot explain the occurrence of the 2H polytype with large d , we suggest that it arises from truly special kinetic conditions (the unusually slow growth process). It is reasonable to conclude that its metastability is probably due to the relatively large configurational entropy that is expected from a rather flat energy surface with shallow wells and low bumps (small energy barriers and shallow energy wells) associated with very soft and marginally unstable (< 5 meV) vibrational modes seen in our calculated spectra. This becomes particularly relevant when we allow the structure to distort using eigenvectors of modes at M point. Hopping between these shallow energy minima allows the apparent inter-planar distance to be small kinetically (over short time scales) while it remains large when seen as a thermodynamic average. In a way, the structure resembles an ‘ordered glass’ or an ‘ordered supercooled liquid’, which is metastable for a much shorter time than the typical time scale of a glass, which is not surprising as it is quite ordered.

Based on the fact that gold (rather than silver) has been known to exhibit a planar structure in both clusters and complexes, we might expect the ‘graphitic’ 2H polytype to be comparatively more stable in the case of gold. This encouraged us to also determine the energetics of the 2H, 3C, 4H, and 6H polytypes of gold. The structures were fully relaxed with respect to atomic positions and lattice vectors, and their cohesive energies determined. We find expectedly that 3C is the most stable structure, while the other

polytypes lie within a few meV/atom of 3C. The order of stability (binding energy) is $3C > 6H > 4H > 2H$, which is just the same as found in the case of silver. The values of the cohesive energy per atom of 3C, 6H, 4H, and 2H polytypes of gold are 0 meV, 1.2 meV, 2.0 meV, and 4.9 meV, respectively, with 3C as the reference. In comparison, our estimates of the cohesive energies per atom of the silver 3C, 6H, 4H, and 2H polytypes are 0 meV, 0.9 meV, 1.3 meV, and 2.3 meV, respectively. Based on the energetics, we predict that the occurrence of 2H polytype is more likely in silver than in gold, although it is metastable in both cases.

4.1.7 Conclusions

On examining the possible stability of the large- c 2H polytype of silver using extensive simulations of energetics and lattice dynamics, we find that the structure is not inherently stable, and cannot be stabilized by increasing the temperature or intercalation of atoms such as N or O. Weak instabilities in the final distorted 2H structure that are evident our local stability analysis, suggests an energy surface that is rather flat with respect to many modes. This feature of the energy surface makes a large contribution to configurational entropy, and is likely to be a possible cause for *meta-stability* of the observed 2H polytype with unusually large c -constant. We thus conclude that the observed 2H polytype of silver is a **metastable** structure, in a way similar to supercooled liquid state but exhibits a reasonably good long-range order.

4.2 4H polytype [†]

4.2.1 Introduction

In addition to the 2H polytype, the 4H polytype (ABACABAC...) of silver has been experimentally synthesized by Chakraborty *et al.* [92]. The observed 4H polytype is metastable, and makes a transition from 4H to 3C structure between the temperature range of 433 K

[†]This work has been published in part in Journal of Physics: Condensed Matter [97, 98]. Copyright (2014) by Institute of Physics (IOP).

to 443 K. Though there exist extensive accounts on polytypism and polytypic phase transitions in literature [99], the origin of such large periodicities in polytypes, and the nature of these transitions are not fully understood. The one most commonly observed feature that appears to link all polytypes is the presence of stacking faults [99]. The creation and periodic arrangement of stacking faults (which are deviations from the ideal stacking sequence of the crystal structure) are known to give rise to polytypes [100]. Hence, we have explored the possible mechanisms of this transition through instability of the structure to form stacking faults by estimating the contribution of vibrational entropy to stacking fault energy using first-principles analysis, and predict the P-T phase diagram of the 3C and 4H polytypes of silver. We have also investigated the instability of electronic structure of the 4H polytype with respect to a Charge Density Wave (CDW).

4.2.2 Computational Methods

See section 3.1.2 for details of the first-principles calculations. The exchange-correlation energy of electrons was treated within a Generalized Gradient Approximated (GGA) functional of Perdew Burke Ernzerhof parametrized form [30]. Stacking fault was introduced in a supercell of 1x1x3 dimensions with a stacking sequence of ABAC ABAB ABAC. All the Brillouin zone (BZ) integrations were sampled over a 9x9x3 and 9x9x1 mesh of k-points for pristine and faulted structures, respectively. All the Brillouin zone (BZ) investigations were sampled over a 9x9x3 and 9x9x1 mesh of k-points for pristine and faulted structures respectively. Such a choice was made after verifying that a larger mesh of k-points, e.g. 15x15x5, has no significant impact on the results obtained. For example, the energy of the 4H polytype with respect to the 3C polytype obtained with 9x9x3 and 15x15x5 k-meshes were 1.3 meV/atom and 1.5 meV/atom, respectively. Not only do the energy differences converge within ≈ 0.2 meV/atom with respect to k-mesh sampling, we also find no significant change in the electronic Fermi surface and band structure of the 4H polytype calculated with a 15x15x5 mesh. This justifies our use of a 9x9x3 mesh of k-points sampling the BZ integrations for the pristine structures. In the case of the faulted structures, we use a 9x9x1 mesh because the corresponding Brillouin zone is shorter by a factor of 3

along c-direction.

To determine phonons and dynamical matrices at the wavevectors on a mesh, we have used DFT linear response as implemented in the Quantum ESPRESSO package. The dynamical matrices of pristine and faulted silver were calculated on a q-point grid of $2 \times 2 \times 2$ and $2 \times 2 \times 1$, respectively, and Fourier interpolated onto a much finer mesh to determine free energy in the quasi-harmonic approximation.

4.2.3 Electronic structure of pristine 4H polytype

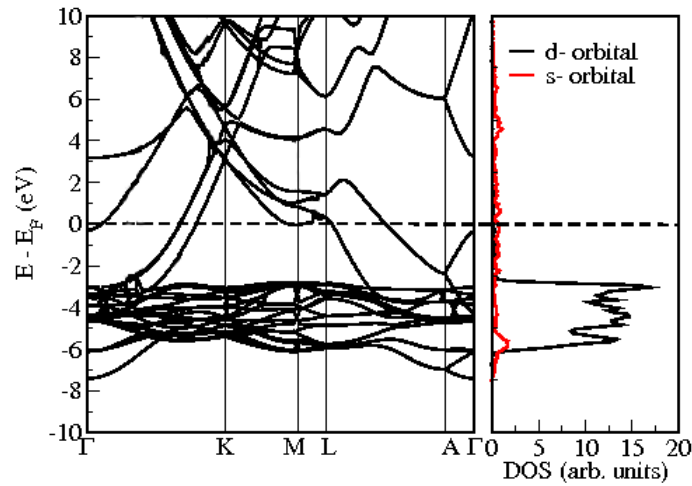


Figure 4.5: Electronic structure of pristine 4H polytype. Left panel shows the band structure and right panel shows the projection of the density of states (DOS) on the 4d and 5s orbitals of silver. Note that the d orbitals constitute a flat band below the Fermi level, and the band width is approximately 3 eV. Here, all the energies are scaled with respect to Fermi level. Copyright (2014) by Institute of Physics (IOP) [97].

The electronic structure of the pristine 4H polytype along high symmetry direction in reciprocal space (refer to Figure 4.5) shows that the main contribution to the relatively flat band about 3 eV below the Fermi level comes from the 4d orbitals of silver. The 5s orbitals, on the other hand, contribute to bands crossing at the Fermi level and hence to the metallic nature of silver. The Fermi surfaces constituted of the four bands crossing the Fermi level (refer to Figure 4.6) show no nesting for bands 2, 3 and 4. However there is a weak nesting between the vertices of the hexagonal Fermi surface of band 1. On a closer look (refer to Figure 4.6b) we observe that the edges of the hexagon are curved, and

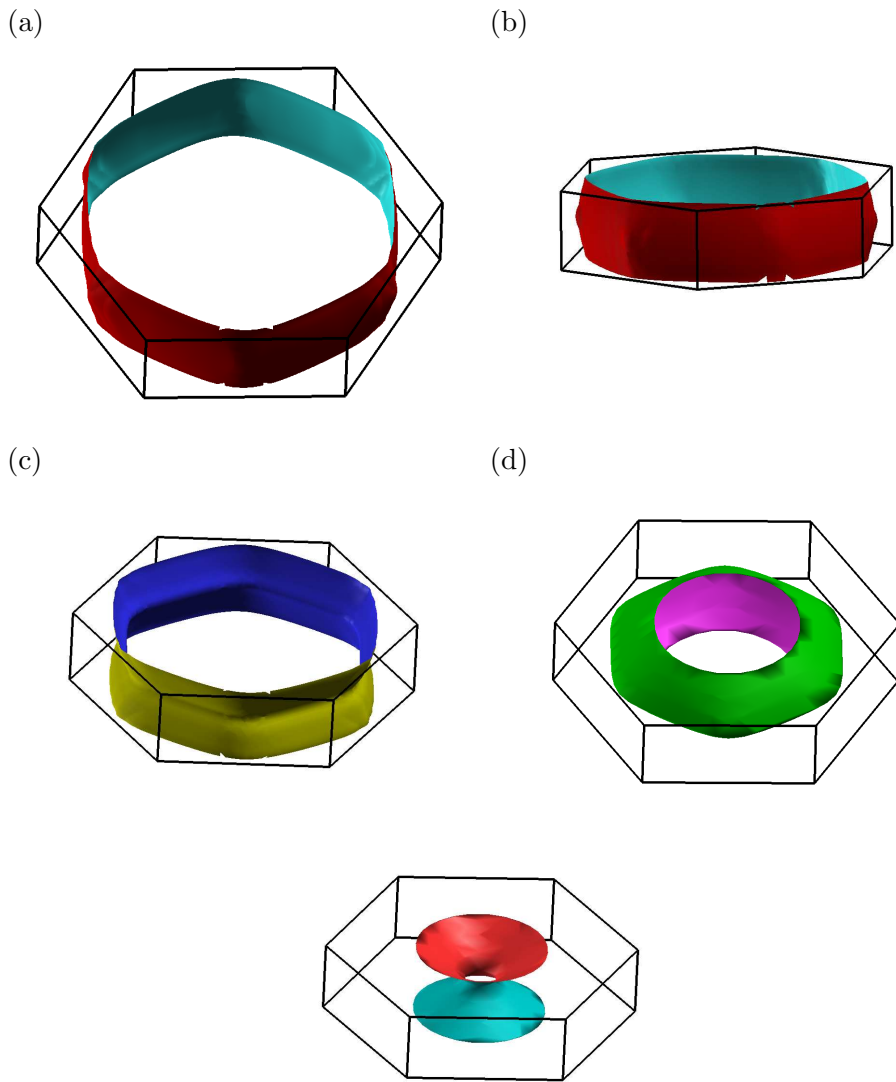


Figure 4.6: Fermi surface plots of pristine 4H polytype of silver. (a) Top view and (b) side view of band number 1, (c), (d) and (e) are the top views of band numbers 2, 3 and 4 respectively. Note that for band number 1, there is no nesting between the vertices of the hexagonal Fermi surface due to curved edges. Copyright (2014) by Institute of Physics (IOP) [97].

that the nesting between the edges is not over a significant interval in k -space. This is in contrast with the recently discovered 2H polytype of Ag, for which more significant Fermi surface nesting was observed [92]. From the phonon dispersion of pristine 4H polytype (refer to Figure 4.7), we conclude that 4H polytype is locally stable as it does not exhibit any unstable modes (*i.e.* imaginary frequencies). Since the 4H polytype is structurally

stable and does not exhibit Fermi surface nesting, we eliminate the possibility of structural transition or occurrence of a charge density wave (CDW) in the system.

In the Hagg notation the 4H configuration is given by $[+ - - +]_n$ corresponding to an ABACABAC... stacking, while the 3C phase is given by $[+ + +]_n$ corresponding to an ABCABC... stacking. From the DFT calculations, we find that the energy of the 3C phase is slightly lower (i.e. ≈ -0.46 meV/atom) than that of the 4H phase. The relatively higher stability of 3C-Ag is attributed to the higher density of stacking faults (i.e. higher number of sign flips in the Hagg) associated with 4H-Ag.

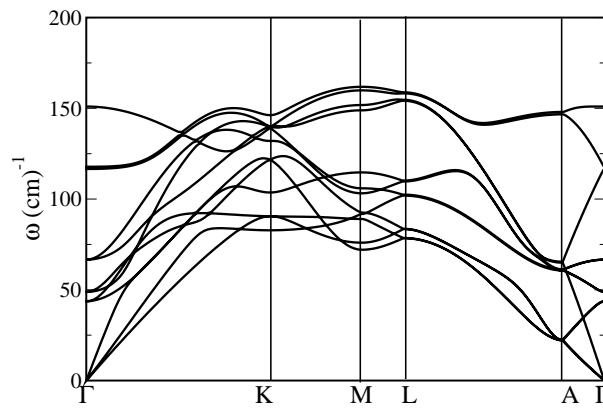


Figure 4.7: Phonon dispersion of pristine 4H polytype of silver. Observe that all the phonon frequencies are real, which imply a locally stable structure. Copyright (2014) by Institute of Physics (IOP) [97].

4.2.4 Do stacking faults drive the structural phase transition?

In experiments, it was observed that the 4H polytype of silver makes a phase transition to the 3C polytype at ambient pressure between the temperature range of 433 K to 443 K. We explore whether stacking faults can lead to such a transition from 4H polytype to 3C polytype.

In the 4H polytype with ABAC stacking sequence, the only possible stacking faults have sequences ABAC ABAB ABAC and ABAC ACAC ABAB. In Hagg notation, 4H polytype is $[+ - - +]_n$ and the two stacking faults correspond to $+ - - + + - + - + - - +$ (ABAC ABAB ABAC) and $+ - - + - + - + + - - +$ (ABAC ACAC ABAC), which implies that

both are equivalent. Henceforth we consider only the stacking fault with ABAC ABAB ABAC stacking sequence. The stacking fault energy $[\gamma_s(T=0 \text{ K})]$ associated with this planar defect at 0 K is $\approx 3.3 \text{ mJ/m}^2$. While the 4H polytype is stable against formation of stacking faults at 0 K, the low stacking fault energy suggests that wide faults should be present in 4H polytype. We now explore a possibility of stabilization of the stacking fault in 4H polytype due to vibrational free energy (F_{vib}) at finite temperatures. The vibrational free energy is calculated as, [101]

$$F_{vib}(T) = \frac{k_B T}{N_q} \sum_q \sum_i \log \left[2 \sinh \left(\frac{\hbar \omega_{qi}}{2k_B T} \right) \right], \quad (4.1)$$

here, k_B , \hbar and T are the Boltzmann constant, Planck's constant and temperature respectively. N_q denotes the number of wavevectors in the Brillouin zone (BZ) at which the frequencies are calculated, and q the wavevector. i denotes the mode of vibration ($i=1$ to $3N_a$, N_a is the number of atoms). ω_{qi} corresponds to the phonon frequency at wavevector q and i^{th} mode of vibration. In the calculation of free energy, we have omitted the zero frequency, acoustic modes at Γ -point.

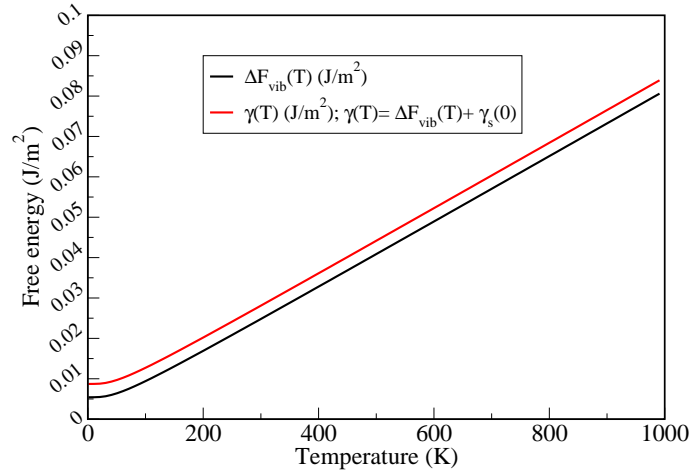


Figure 4.8: Variation in stacking fault energy of 4H polytype with temperature. Red (grey) and black curves denote $\gamma_s(T)$ and $\Delta F_{vib}(T)$, respectively. Note that the vibrational contribution to the free energy at 0 K is higher than that of stacking fault energy. Copyright (2014) by Institute of Physics (IOP) [98].

We estimate the variation in stacking fault energy as a function of temperature using

$\gamma_s(T) = \gamma_s(0) + \Delta F_{vib}(T)$. Where, $\Delta F_{vib}(T)$ is the difference between the vibrational free energy of faulted and pristine structure obtained using Equation (1). As $T \rightarrow 0$ K, we observe that $\Delta F_{vib}(T) \approx 5$ mJ/m² (is larger than $\gamma_s(0)$), *i.e.* the vibrational free energy too does not stabilize the faulted structure at 0 K. At finite temperatures, the energy of the stacking fault continues to increase with temperature (refer to Figure 4.8). In the temperature range of the phase transformation (433 K to 443 K), the stacking fault energy is ≈ 0.039 J/m², implying that the faults in 4H polytype will become narrower with temperature. Since 4H is a more faulted structure relative to 3C, it implies that the 3C structure is favoured over the 4H structure at higher temperature. Our results show that, faulted 4H polytype is locally stable but, it remains higher in energy than the pristine 4H polytype for $T > 0$ K. Hence, we conclude that the transition of 4H to 3C polytype of silver between the temperature range of 433 K to 443 K is probably not driven by stacking faults.

4.2.5 Phase diagram of 3C and 4H polytype

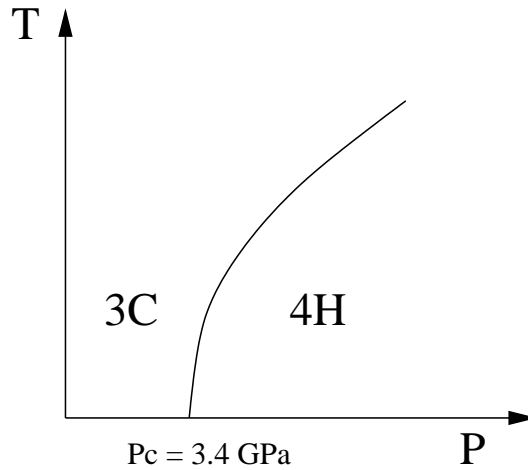


Figure 4.9: Phase diagram for 3C and 4H polytypes of silver. Note that 4H polytype makes a transition to 3C polytype under 3.4 GPa pressure at 0 K. P and T denote pressure and temperature respectively. Copyright (2014) by Institute of Physics (IOP) [98].

We have explored the possibility of a structural phase transition due to application of external pressure. We estimate a critical pressure of 3.4 GPa (at 0 K) for the system to make a phase transition from the 3C to 4H polytype. With the available data at 0 K and

$P = 0$ GPa, we guess a P-T phase diagram for the 3C and 4H polytypes of silver (refer to Figure 4.9). From the phase diagram, it is evident that the experimentally observed phase transition (at ambient pressure and within the temperature range of 433 K to 443 K) cannot be explained with just thermal fluctuations and other atomistic mechanism maybe responsible this phase transformation.

4.3 Conclusions

We show that the pristine 4H polytype of silver is locally stable, and does not exhibit Fermi surface nesting. Thus, it is stable against displacive structural transition and the formation of a CDW. Secondly, the observed transformation of 4H polytype to 3C polytype of silver is unlikely through the formation of stacking faults or soft modes. We believe that other mechanisms such as local -ve pressures (since we estimate a negligible change in volume at critical pressure *i.e.* $\Delta V \approx 0.01 \text{ \AA}^3/\text{atom}$) need to be explored to understand the 4H to 3C transformation.

Chapter 5

Oxides

5.1 Effect of anti-site disorder on structural, electronic and magnetic properties of $\text{Al}_{1-x}\text{Ga}_x\text{FeO}_3$ *

5.1.1 Introduction

Al_2O_3 , Ga_2O_3 and Fe_2O_3 are known to crystallize in the rhombohedral structure, and their metastable orthorhombic phases are also known to exist [103]. Surprisingly the stable structures of AlFeO_3 and GaFeO_3 belong to the non centrosymmetric polar space group with an orthorhombic ($\text{Pna}2_1$) structure. Since AlFeO_3 and GaFeO_3 are reported to be ferrimagnetic, piezoelectric and magnetoelectric at low temperatures [104–107], these materials are also likely to exhibit multiferroicity. In view of their unusual properties, using first-principles density functional theory based calculations, we have attempted to understand how magnetic ordering in $M\text{FeO}_3$ ($M = \text{Al}, \text{Ga}$) and related properties depend sensitively on the disorder at the cation site. The tendency of cations to disorder, its origin and the associated properties are traced to the local structure and ionic sizes. A strong coupling between the structure and the spin at the Fe sites, arising from anti-site disorder is suggested to be responsible for observed magnetocapacitive response [108].

*This work has been published in part in Journal of Solid State Chemistry [102]. Copyright (2011) by Elsevier.

5.1.2 Computational Methods

Our first-principles calculations were based on density functional theory (DFT) with a spin-density dependent exchange correlation energy approximated with a generalized gradient approximated (GGA) (PerdewWang 91 (PW 91)) functional form [31] as implemented in the Vienna ab initio Simulation Package (VASP) [109–112]. The projector augmented wave (PAW) method [113] was used to capture interaction between ionic cores and valence electrons. An energy cutoff of 400 eV was used to truncate the plane wave basis and integrations over the Brillouin were sampled over a $4 \times 4 \times 4$ mesh of k-points. Structure was optimized to minimum energy using Hellman-Feynman forces, while maintaining the lattice constants at their experimental values. Minimum energy states with different magnetic ordering were obtained through appropriate initialization of the spins on *Fe* sites.

5.1.3 Structure

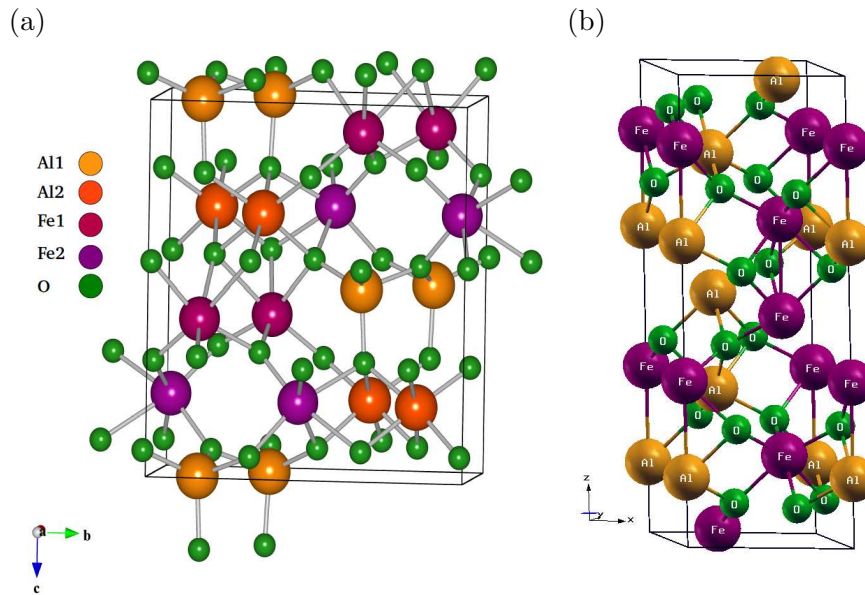


Figure 5.1: (a) Orthorhombic and (b) Corundum structures of AlFeO₃. Copyright (2011) by Elsevier [102].

We examine the crystal structure of AlFeO₃. Its space group is Pna2₁ with a unit cell consisting of 8 formula units (40 atoms) refer to Figure 5.1a. There are four different

Wyckoff sites of cations labelled Fe1, Fe2 (predominantly occupied by iron), Al1 and Al2 (predominantly occupied by aluminum). The oxygen environment of Al1 forms a regular tetrahedron, while other sites have distorted octahedral coordination; with higher distortion for the Fe1 and Fe2 sites. The occupancy factors of the (taken from Ref. [104]) cation sites are given in Table 5.1. Cation site disorder here means occupation of Fe site by an Al cation or vice-versa, which arises from an interchange of Al and Fe atoms in the perfectly ordered structure. From the observed occupancies of cation sites at low temperatures, disorder arises with highest probability through interchange in the positions of Fe and Al cations at Fe2 and Al2 sites respectively. We have simulated the disordered structure (D) obtained by interchanging one Al at Al2 site with one Fe atom at Fe2 site (in one unit cell, amounting to 12.5 % anti-site defects), along with the perfectly ordered structure (O). Symmetry of the structure permits a non-zero polarization along the c -axis, consistent with the known piezoelectric properties.

Table 5.1: Occupancy factors of AlFeO_3 at room temperature (RT) and at $T=30$ K (taken from [104]). Copyright (2011) by Elsevier [102].

cation site	Occupancy by Fe	Occupancy by Al
Fe1 (RT)	0.777	0.223
Fe1 (30)	0.803	0.197
Fe2 (RT)	0.764	0.236
Fe2 (30)	0.751	0.249
Al1 (RT)	0.095	0.905
Al1 (30)	0.105	0.895
Al2 (RT)	0.340	0.660
Al2 (30)	0.310	0.690

5.1.4 AlFeO_3 : Disorder, Magnetic Ordering and Stability

From our results for energies of ferromagnetically and antiferromagnetically ordered states of AlFeO_3 (see Table 5.2), it is clear that the antiferromagnetic state (AFM) is noticeably more stable than the ferromagnetic (FM) one in the chemically ordered case. Noting

that there are eight Fe ions with six-fold coordination in the unit cell, an estimate of the exchange coupling in a model with nearest neighbour interaction of constant spins is about 0.076 eV, significantly higher than the experimental magnetic transition temperature. This is rationalized through closer examination of the magnetically ordered states: magnetic moments on various Fe ions change significantly (see Tables 5.3 and 5.4) with change in their magnetic ordering, resulting in Fe^{3+} in the low-spin state in the FM-ordered state.

Table 5.2: Energetics of magnetic configuration. Copyright (2011) by Elsevier [102].

order/ disorder	Total energy of magnetic configuration (eV)		
	AlFeO ₃ -FM	AlFeO ₃ -AFM	GaFeO ₃ -AFM
ordered	-297.02	-300.67	-270.71
disordered	-298.59	-300.09	-270.45

Thus, interpretation of the estimate of exchange interaction is a bit tricky when compared with experimental magnetic transition. As the low-spin state of Fe^{3+} is known to be rare in nature, FM state of AlFeO₃ is indeed much higher in energy than the AFM one. A rather interesting change is seen in our analysis when we introduce the anti-site disorder between Fe2 and Al2. First of all, the difference in energies of FM and AFM states (see Table 5.2) becomes much smaller with an estimated strength of the nearest neighbour exchange interaction of about 0.031 eV, which is much smaller than that (0.076 eV) in the chemically ordered configuration. Secondly, the magnetic moments (see Tables 5.3 and 5.4) of the Fe ion located only at the Al2 site change significantly, indicating its low-spin state in the FM ordering. Our result for the strength of exchange interaction in this case in comparison with experimental T_c is an overestimate, typical of DFT calculations. We note that the magnetic moment on each Fe^{3+} ion varies with the site in both the AFM and FM states, and in this sense the system is *ferrimagnetic* with a rather small effective magnetic moment, as seen experimentally. The energy of the lowest energy magnetic ordering in

the disordered case is 0.58 eV higher than that in the ordered case, giving an estimate of energy of an anti-site defect. Interestingly, FM ordering in the disordered state is lower in energy than the FM ordering in the chemically ordered state.

Table 5.3: Total magnetic moments. Copyright (2011) by Elsevier [102].

order/disorder	Total magnetic moment (μ_B)	
	FM	AFM
ordered	7.80	0.058
disordered	22.87	-0.002

Table 5.4: Magnetic moments on individual Fe ions (μ_B). Copyright (2011) by Elsevier [102].

Atom no.	Cation site	Magnetic moment (μ_B)			
		FM		AFM	
		order	disorder	order	disorder
1	Fe1	1.26	3.85	3.59	3.69
2	Fe1	1.26	-3.20	3.59	3.40
3	Fe1	1.26	3.12	3.59	3.71
4	Fe1	1.26	3.77	3.59	3.58
5	Fe2/Al2	0.50	1.27	-3.57	-3.72
6	Fe2	0.50	3.70	-3.57	-3.59
7	Fe2	0.50	3.66	-3.57	-3.58
8	Fe2	0.50	3.81	-3.57	-3.54

We now examine these results in terms of the electronic and atomic structure and how they are affected by anti-site disorder. Fe³⁺ ion has an [Ar] 3d⁵ electronic configuration, and an octahedral crystal field results in a splitting of the degeneracy of its *d* state into *t*_{2g} and *e*_g states. Hund's coupling (intra-atomic exchange interaction) breaks the spin

degeneracy, and all 5 d electrons occupy states with the same spin. For the d^5 configuration, superexchange interaction via O is strongly anti-ferromagnetic, particularly when $Fe - O - Fe$ bond angles are close to 180° . Hence, the ground state exhibits an AFM ordering. Ideally, such electronic structure would give a magnetic moment of $5 \mu_B$ per Fe ion corresponding to the high-spin state. Our simulations, however, give a moment of about $4 \mu_B$ per Fe ion due to a strong hybridization between the d -states of Fe and the p -states of O (see Figures 5.2 and 5.3), similar to that in $BiFeO_3$ [114]. We note that we have not included any on-site correlation (Hubbard $U = 0$), and hence the d -band widths are expected to be overestimated. If the crystal field splitting is larger than the exchange coupling, Fe^{3+} can be in the low-spin state (see Figures 5.2 and 5.3), as seen in our simulations of (a) FM state in the chemically ordered case, and (b) Fe populating Al2 site of the FM state in the disordered case. In the AFM states and chemically disordered FM state (except for the Fe populating Al2 site) however, Fe^{3+} is always in the high-spin state irrespective to its site, consistent with its greater stability.

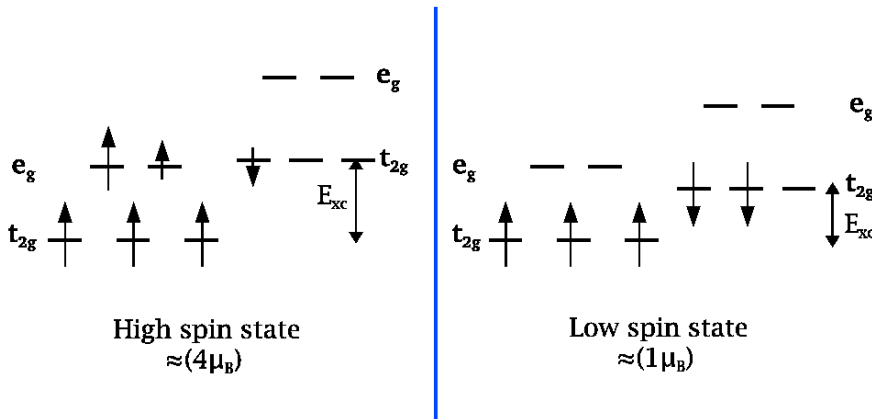


Figure 5.2: High-spin and low-spin state. Copyright (2011) by Elsevier [102].

This is also reflected in a small gap in the electronic structure (see Figure 5.3), which is typically underestimated in DFT calculations. We point out that the simulated gap may become more pronounced when on-site correlation (through Hubbard U correction) is included. A non-zero density of states at the Fermi energy in the AFM state of the disordered case arises from the states *localized* on Fe^{3+} at Al2 site and is not expected to

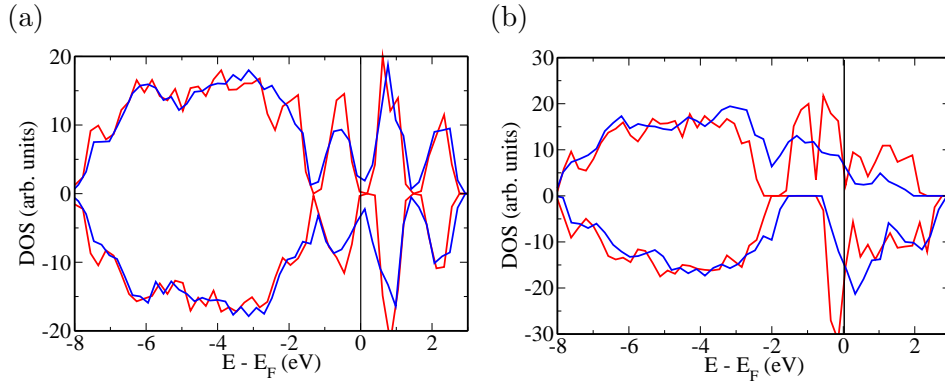


Figure 5.3: Electronic density of states for (a) AFM state and (b) FM state. Positive values are for up spin and negative for down spin. Ordered state is shown in **red** and disordered state is shown in **blue**. Copyright (2011) by Elsevier [102].

make it metallic. Finally, a larger exchange energy E_{xc} in the disordered FM state than that in the ordered FM state is responsible for its high-spin state and its greater stability.

Table 5.5: Fe-O and Al-O bond lengths (\AA). Copyright (2011) by Elsevier [102].

state	Chemically ordered		Chemically disordered	
	L(Fe-O)	L(Al-O)	L(Fe-O)	L(Al-O)
FM	1.87	1.90	1.85	1.86
	1.87	1.92	1.93	1.87
	1.97	1.93	1.95	1.91
	2.04	1.96	1.97	1.95
	2.06	1.96	1.97	2.02
	2.11	2.02	1.99	2.05
AFM	1.83	1.88	1.90	1.85
	1.89	1.90	2.02	1.86
	1.99	1.92	2.02	1.90
	2.10	1.94	2.03	1.95
	2.18	1.95	2.05	2.05
	2.24	1.97	2.09	2.07

We now examine the relation of structure and magnetic ordering with anti-site disorder.

From the bond lengths of oxygen to Fe and Al ions at the Fe2 and Al2 sites (see Table 5.5), a characteristic feature becomes evident. The Fe2 site prefers dichotomous (bi-modal distribution) of bond lengths while the Al2 site exhibits uniformity in bond lengths. In the relaxed structures (see Tables 5.3 and 5.5), we observe that the bond lengths change considerably with the change in magnetic ordering implying a strong spin-phonon coupling in the system (note that we report bond lengths for Fe and Al are at Fe2 and Al2 sites respectively in the ordered state; Fe and Al are at Al2 and Fe2 sites respectively in the disordered state). Our results clearly bear that (a) a high-spin state of Fe^{3+} is energetically favorable (lower) than the low-spin state, and (b) Fe-O bonds are longer when Fe^{3+} is in the high-spin state, which are hence linked with disorder intimately. As the Shannon-Prewitt radius of Fe^{3+} in the low-spin state is close to that of Al^{3+} in octahedral coordination, only Fe^{3+} at the Al2 site takes the low-spin state and Fe^{3+} at other sites are in the high-spin state, hence the FM state in the disordered case is significantly lower in energy. This results in longer Fe-O bond-lengths of the high-spin configuration, reflected in the Fe-O bonds of the AFM state with Fe^{3+} taking the high-spin state.

We have also determined energetics of AlFeO_3 in perovskite and corundum (see Figure 5.1b) structures. While Fe is found to prefer *A* site (in the perovskite structure) with a high-spin state and G-AFM ordering, the energy of the cubic perovskite structure is almost 3 eV/f.u. higher than the observed one (chemically ordered AFM state of orthorhombic structure). Secondly, Fe^{3+} randomly occupying Al sites in the corundum structure takes the low spin state (due to size mismatch), and hence AlFeO_3 in the corundum structure is higher in energy by about 84 meV/f.u. than the ordered AFM state of the orthorhombic structure. Thus, we believe that the stability of the observed structure is to be partly due to the distinct sites associated with Al and Fe, giving just the right space to Al and Fe consistent with their size.

5.1.5 GaFeO_3 : Disorder, Magnetic Ordering and Stability

Because of the mismatch in the ionic radii of Fe^{3+} in high-spin state and Al^{3+} , anti-site disorder in AlFeO_3 is relatively weak. In contrast, the radius of Fe^{3+} in high-spin state is

close to that of Ga³⁺ (R= 0.62 Å) in octahedral coordination, hinting a greater degree of anti-site disorder in GaFeO₃. From our calculations on GaFeO₃ we find that (a) its AFM state is lower in energy than the FM one in both the ordered and disordered cases with a slightly larger magnetic moment in the latter, (b) within a DFT-description, FM ordering does *not* occur in a self-consistent solution in the chemically disordered state. (c) In the AFM state, magnetic moments at Fe1 and Fe2 sites are not of the same magnitude giving a weak total magnetic moment effectively. (d) The energy difference between the AFM states in the disordered and ordered cases is only 32 meV/f.u. (as opposed to 73 meV/f.u. of AlFeO₃). Thus, we expect anti-site disorder in GaFeO₃ to be more prominent than in AlFeO₃. Electronic structure of GaFeO₃ is qualitatively similar to that of AlFeO₃.

5.1.6 Conclusions

Our first-principles analysis shows (i) greater anti-site disorder in GaFeO₃ than in AlFeO₃ due to better matching of ionic radii of Fe and Ga, (ii) weak magnetic total moment arising from the difference in effective magnetic moments of Fe³⁺ at Fe1, Fe2 and Al2 sites, and (iii) the presence of strong spin-phonon coupling arising from a large difference in ionic radii of Fe³⁺ in high and low spin states (0.645 and 0.55 Å respectively). Both disorder and magnetic properties are intimately related to the local structure that can be explained in terms of ionic sizes. Spin-phonon coupling demonstrated here is shown to manifest more strongly in the presence of disorder, and hence the corresponding magnetocapacitive effects are expected to be pronounced in GaFeO₃, as found experimentally [108]. In a solid solution of GaFeO₃ and AlFeO₃, additional disorder associated with low-spin states of Fe³⁺, Al and Ga should give even more spectacular magneto-capacitive effects. Disorder in heterovalent cations is well-known to give diffuse dielectric response or relaxor properties in ferroelectrics [115]. In MFeO₃, while disorder occurs among ions of the same charge (Fe³⁺ and Al³⁺), their magnetic spins (Fe being magnetic and Al being non-magnetic) coupling with its structure are distinct. Hence, we conclude that the introduction of disorder and its intimate coupling of spin with the structure (spin-phonon coupling) are key to the properties of MFeO₃ and should give rise to a characteristic frequency-dependent

magneto-capacitive response [108].

5.2 Effect of anti-site disorder on spin-phonon coupling, and its signatures in the Raman spectrum of AlFeO_3 [†]

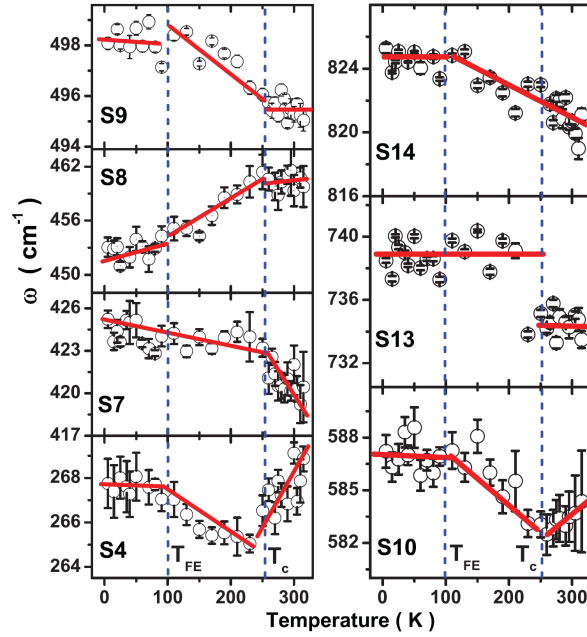
5.2.1 Introduction

Applications of magneto-electric materials require them to exhibit their couplings to responses at and above room temperature, which is often not realized in many multiferroics/magnetoelectric materials. In this context, AlFeO_3 exhibiting ferrimagnetism and magnetoelectric coupling with a paramagnetic to ferrimagnetic transition temperature $T_c \sim 250$ K [104] is very promising. Another attractive feature is its environment friendly nature as compared to other lead based multiferroics. In AlFeO_3 , cations occupy four distinct crystallographic sites: cations Fe1, Fe2 and Al2 with octahedral coordinated of oxygen, whereas Al1 with tetrahedral coordination. Structural analysis of AlFeO_3 [104] shows significant distortion of the FeO_6 octahedra, while oxygen tetrahedron around Al1 is quite regular. The disorder in the occupation of the cation sites, and the difference between octahedral radii of Fe^{3+} and Al^{3+} ions cause the local deformation of lattice. Hence, vibrational properties that depend on the structure, also depend on the magnetic state of the system, and are central to magnetoelectric behavior of many multiferroics. In particular, Raman spectroscopy has proved to be a powerful probe to investigate magnetic ordering induced phonon renormalization where the observed phonon anomalies below the magnetic transition temperature are associated with strong spin-phonon coupling.

A strong spin-phonon coupling and magnetic ordering induced phonon renormalization were evident in the experimental observations of Khatri *et. al.* [116]. These include, (a) anomalous temperature dependence (*i.e.* sudden change or hardening of modes across T_c) of many Raman modes with frequencies below 850 cm^{-1} (refer to Figure 5.4a), particularly

[†]This work has been published in part in Physical Review B [116]. Copyright (2012) by the American Physical Society.

(a)



(b)

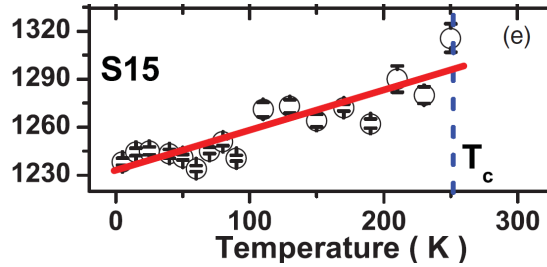


Figure 5.4: Temperature dependence of (a) the first-order phonon modes S4, S7-S10, S13, and S14, and (b) high frequency S15 mode. Note that S8 mode hardens with temperature, and S15 mode disappears above T_c . Solid lines are the linear fits above and below T_c . This work has been done by Khatri *et al.* [116]. Copyright (2012) by the American Physical Society.

near the magnetic transition temperature $T_c \sim 250$ K, and (b) the appearance of a broad mode near 1250 cm^{-1} only below T_c attributed to the two-magnon scattering (see Figure 5.4b). We have carried out first-principles analysis to understand the emergence of these anomalies through determination of the phonon spectrum and its coupling with spin.

5.2.2 Computational Methods

See section 5.1.2 for details of the first-principles calculations. Dynamical matrix and phonons at the Γ -point ($q = 0,0,0$) were obtained with a frozen-phonon method with atomic displacements of $\pm 0.04 \text{ \AA}$. Numerical errors associated with Fourier mesh in our calculations break symmetry of the dynamical matrix weakly and introduce an error of about $\pm 12 \text{ cm}^{-1}$ in phonon frequencies.

5.2.3 Results and Discussion

It is known that AlFeO_3 exhibits disorder associated with occupancy of Fe and Al sites, with most common occurrence of anti-site disorder being between Fe2 and Al2 sites [104]. This disorder is taken into account by exchanging the site positions of an Fe atom at Fe2 site with an Al atom at Al2 site. We have also considered the anti-site disorder between Fe1 and Al2 sites. From the energetics, we find that the AFM state is the most stable for system with either type of anti-site disorder between Fe and Al. The AFM state with Fe1-Al2 anti-site disorder is higher in energy as compared to the AFM state with Fe2-Al2 anti-site disorder by 5.7 meV/atom, corroborating greater occurrence of anti-site disorder. To facilitate a meaningful comparison with experimental Raman spectra, we simulate the structure with experimental lattice constants, and relax internally the atomic positions using conjugate gradients algorithm.

To understand the interplay between disorder, magnetic ordering and phonons, we determine phonons at Γ -point for a chemically disordered structure with non-magnetic (NM), FM and AFM ordering (see Figure 5.5). The spin-phonon coupling is analysed by examining how normal modes evolve with the magnetic ordering by examining the correlation matrix between phonon eigenmodes of AlFeO_3 in two different magnetic states. In the absence of spin-phonon coupling, the phonons would be unaffected by changes in the magnetic order, and hence only the diagonal terms would be non-zero in the correlation matrix. Non-zero off-diagonal elements of the correlation matrix clearly uncover the correspondence between eigenmodes in different magnetic orders. For example, it determines

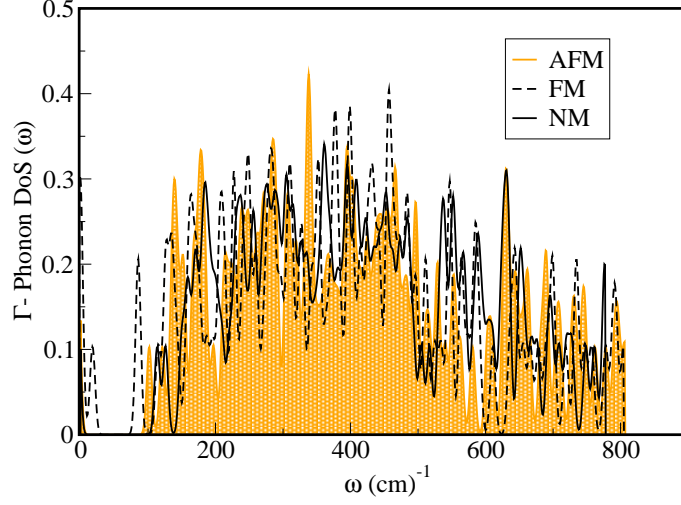


Figure 5.5: Distribution of phonons at Γ -point for AFM, FM and NM orderings with Fe2-Al2 anti-site defect. A Gaussian broadening of $\sim 4 \text{ cm}^{-1}$ has been used here. Copyright (2012) by the American Physical Society [116].

which phonon modes of the AFM state relate to phonons of the FM state, giving a quantitative idea of mixing between modes due to spin-phonon coupling. The spin-hamiltonian has the form:

$$H = \frac{1}{2} \sum_{i,j} J_{i,j} \vec{S}_i \vec{S}_j, \quad (5.1)$$

where, J_{ij} is the exchange interaction between i^{th} and j^{th} using spins S_i and S_j . Only considering the nearest neighbour and isotropic interaction, we reduce J_{ij} to J . The change in J due to spin phonon coupling is given by the second-order Taylor series expansion of J w.r.t. amplitude of atomic displacements ($u_{\nu\Gamma}$) of the ν^{th} Γ -phonon mode of the magnetic state,

$$J(u_{\nu\Gamma}) = J_o + \overline{u_{\nu\Gamma}} (\nabla_u J) + \frac{1}{2} \overline{u_{\nu\Gamma}} (\nabla_u^2 J) \overline{u_{\nu\Gamma}}, \quad (5.2)$$

Substituting equation 5.2 in equation 5.1, and summing over all modes gives,

$$H = \frac{1}{2} \sum_{i,j} \sum_{\nu} \left[J_o + \overline{u_{\nu\Gamma}} (\nabla_u J) + \frac{1}{2} \overline{u_{\nu\Gamma}} (\nabla_u^2 J) \overline{u_{\nu\Gamma}} \right] \cdot \vec{S}_i \vec{S}_j. \quad (5.3)$$

Here, J_o is the bare spin-spin coupling parameter, $\nabla_u J$ corresponds to the force exerted on the system due to change in magnetic ordering from its ground state magnetic configuration, and $\nabla_u^2 J$ is proportional to the change in phonon frequency (Δ) of ν^{th} Γ -phonon mode due to change in magnetic ordering. From the spin-hamiltonian (see equation 5.1), energies of a single pair of spins in AFM and FM states are given by, $E_{AFM} = -J_o|S|^2$ and $E_{FM} = J_o|S|^2$ respectively. The difference in the energies of AFM and FM states is directly proportional to J_o . The unit cell of AlFeO₃ used in our simulation contains 8 Fe ions where, the i^{th} Fe ion is connected to z_i number of other Fe ions. This gives, $J_o = (E_{FM} - E_{AFM})/(\sum_i z_i \cdot 8 \cdot |S|^2)$; here $S = 5/2$ and $E_{FM} - E_{AFM} \sim 1.5$ eV from first principles calculations. Our estimate of the exchange coupling parameter J_o is thus 6 meV. This value is in good agreement with the one estimated from the two-magnon peak observed in Raman spectrum reported by Khatri *et al.* [116].

Assignment of the modes in Raman spectrum of a polycrystalline sample is tricky. In our theoretical analysis, we have listed only those calculated phonon frequencies which are close in frequency to the experimentally observed Raman active phonon modes (refer to Table 5.6). In the presence of anti-site disorder, many of the phonon modes which lie in the vicinity of the experimentally observed Raman active mode can be Raman active. We assume the correlation between the experimentally observed modes which exhibit anomalies at magnetic transition and calculated spin-phonon coupling for modes with frequencies in the vicinity of the observed modes, and carry out the mode assignment (see Table 5.6).

$\nabla_u J (J_1)$ is the coupling parameter derived from force acting on ions due to change in magnetic ordering. This is a measure of one-phonon-spin coupling (see Figure 5.6). From the change in structure with change in magnetic order from AFM to FM, it is apparent that all phonon modes couple (with varied degree) to the spin at the lowest order! In the configuration with Fe2-Al2 anti-site disorder, the modes that show significant coupling to spin at the first order (J_1) are S3, S7, S8, S9 and S11 (refer to Figure 5.6a). The largest coupling is shown by mode S11 which experimentally shows low intensity [116]. In spite of the mode being less populated or less Raman active, it contributes considerably to spin

Table 5.6: List of the experimental observed frequencies at 5 K and calculated frequencies in AlFeO_3 for disordered AFM (Fe2-Al2 anti-site disorder) state. Copyright (2012) by the American Physical Society [116].

Mode Assignment	Experimental ω (cm^{-1})	Calculated (cm^{-1})
S1	156	154
S2	178	179
S3	198	197
S4	268	270
S5	328	331
S6	380	379
S7	425	425
S8	453	453
S9	498	499
S10	587	581
S11	650	654
S12	698	691
S13	738	733
S14	826	807
S15 (Two-magnon)	1240	
S16 (Overtone)	1450	
S17 (Second-order)	1560	
S18 (Overtone)	1660	

phonon coupling at first order. We have carried out a similar analysis for non-magnetic (NM) and AFM states to estimate parameters proportional to the first and second order coupling parameters respectively. In Figure 5.6b, we see that modes, S1, S2, S5, S8, S10 and S11 couple to spin strongly at the first order. The maximum deviation of these frequencies from their experimental values is about 30 cm^{-1} , and the mode S1 exhibits the strongest spin-phonon coupling.

We next present results of the calculations for the anti-site disorder between Fe1 and Al2 sites. From the energetics we find that the AFM state is most stable for the configuration with anti-site disorder between Fe1 and Al2. This state is slightly higher in energy w.r.t. AFM state with Fe2-Al2 anti-site disorder by 5.7 meV/atom . The state with FM

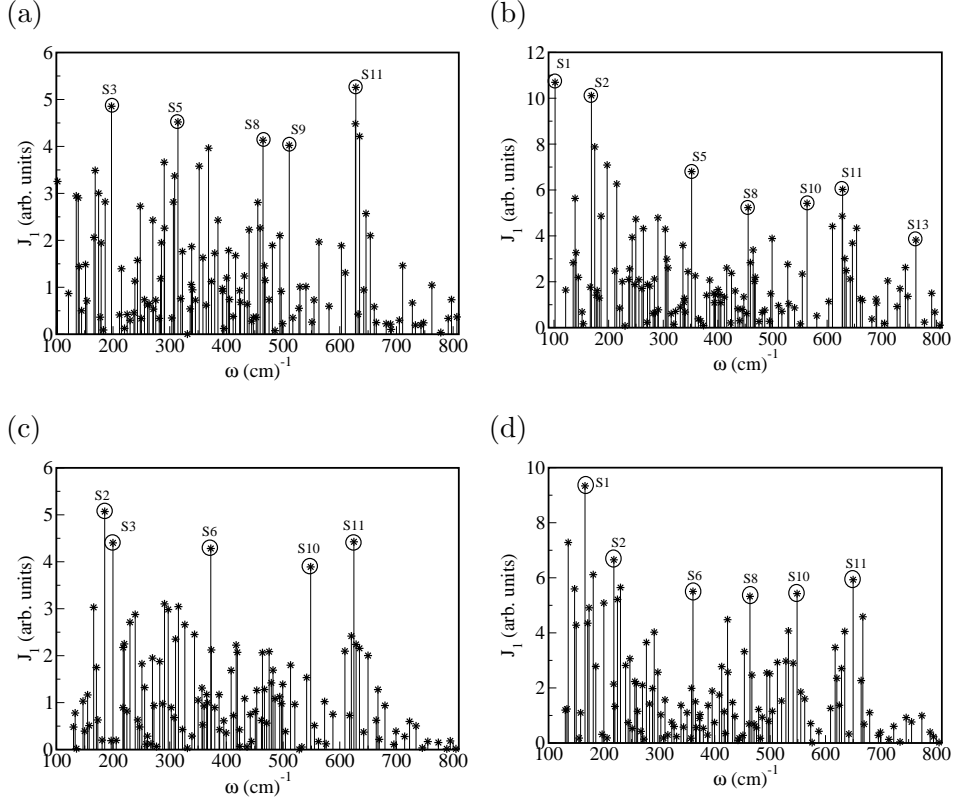


Figure 5.6: First-order spin-phonon coupling (J_1) in different magnetic states. (a) FM-AFM and (b) NM-AFM states with Fe2-Al2 anti-site disorder. (c) FM-AFM and (d) NM-AFM states with Fe1-Al2 anti-site disorder.

ordering with Fe1-Al2 anti-site disorder is more stable than the FM configuration with Fe2-Al2 anti-site disorder in the configuration by 29.3 meV/atom. From the normal mode analysis of FM ordered state with anti-site disorder between Fe1 and Al2 sites, we find an unstable mode of sizeable imaginary frequency of $\sim 390 \text{ cm}^{-1}$, a clear indication of the strong spin-phonon coupling in the system. First order (J_1) couplings of spin with lattice degrees of freedom for change in magnetic ordering from FM to AFM (with anti-site disorder between Fe1 and Al2 sites) are given in Figure 5.6c. It is observed that modes S2, S3, S6, S10 and S11 couple to the spins at the lowest order, with S2 and S11 exhibiting rather strong coupling with the spin. The analysis of the spin-phonon Hamiltonian for the NM and AFM state shows that modes S1, S2, S6, S8, S10 and S11 (see Figure 5.6d) couple to the spins at the lowest order.

Denoting $\nabla_u^2 J$ as J_2 , the change in phonon frequency (Δ) of the λ^{th} Γ - point phonon

mode is given by

$$\Delta_\lambda = \frac{1}{2\mu_\lambda\omega_\lambda} \sum_\nu \vec{u}_{\nu\Gamma} J_2 \vec{u}_{\nu\Gamma}. \quad (5.4)$$

Here, μ_λ and ω_λ are the reduced mass and frequency of the λ^{th} phonon mode at Γ , respectively. We note that large Δ implies stronger spin-coupling. We carried out calculations for both types of disorder: Fe2 at Al2 site (Fe2-Al2) as well as Fe1 at Al2 site (Fe1-Al2). For Fe2-Al2 type disorder, Figure 5.7a and Figure 5.7b show the changes in the Γ -point phonon frequency (Δ) between FM and AFM and NM and AFM states respectively. The corresponding changes for Fe1-Al2 disorder are shown in Figure 5.7c and Figure 5.7d.

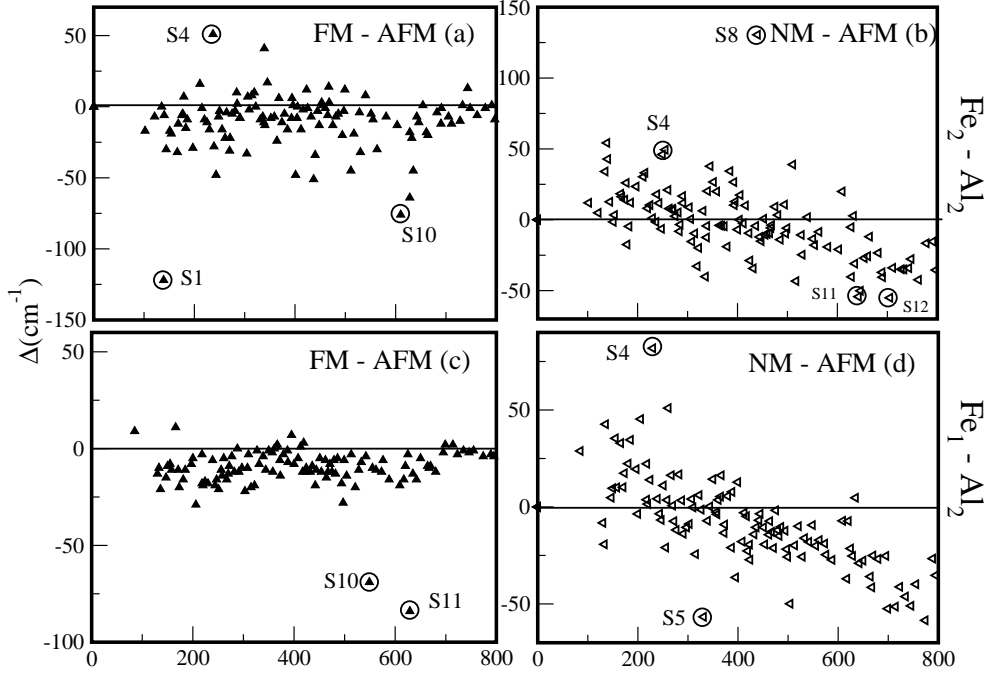


Figure 5.7: Second-order spin-phonon coupling (J_2) in different magnetic states. (a) FM-AFM and (b) NM-AFM states with Fe2-Al2 anti-site disorder. (c) FM-AFM and (d) NM-AFM states with Fe1-Al2 anti-site disorder [116].

In case of Fe2-Al2 anti-site disorder, Δ and hence J_2 , which corresponds to correlations between phonons of FM/NM state with AFM state (see Figure 5.7) is high for modes with frequencies in the neighbourhood of modes S1, S4 and S10 for FM-AFM coupling (see Figure 5.7a) and modes S4, S8, S11 and S12 (see Figure 5.7b) for NM-AFM state

coupling. We note that J_2 for NM-AFM state coupling is not exactly spin-phonon coupling parameter as in the case of FM-AFM state coupling, but here it denotes the change in phonon frequencies in going from NM state to AFM ordering. In Figure 5.4a modes close to S4, S7, S8 and S10 show sharp changes in frequency at the transition temperature T_c suggesting their strong coupling with spin, consistent with our first-principles calculations. Another interesting observation from Figure 5.7b is that the mode with frequency near S8 (438 cm^{-1}) shows increase in frequency (by $\approx 130 \text{ cm}^{-1}$) in going from AFM to the NM state at T_c , and is consistent with experimental observations of Khatri *et al.* [116].

We now discuss the effect of Fe1-Al2 anti-site disorder. Figure 5.7c and Figure 5.7d correspond to correlation between phonons of FM/NM state with AFM state, respectively. For the change in magnetic ordering from FM to AFM state, modes near S10 and S11 (see Figure 5.7c) couple strongly to spin at the second order. In comparison, modes close to S4 and S5 (see Figure 5.7d) show large second order coupling for a change from NM to AFM ordering. Mode S4 shows a significant hardening in going from the AFM state to the NM. We have thus confirmed the existence of strong spin-phonon coupling and the anomalous hardening of the S8 mode due to strong spin-phonon coupling at the second-order (J_2) in AlFeO_3 with Fe2-Al2 anti-site disorder in going from AFM to NM ordering. We have listed modes coupling to spins at the second order (J_2) for different anti-site disorder configurations in different magnetic states in Table 5.7.

Table 5.7: List of modes coupling to spins at the second order (J_2) for Fe1-Al2 and Fe2-Al2 anti-site disorder configurations in different magnetic states.

anti-site disorder	Mode	
	FM-AFM	NM-AFM
Fe1-Al2	S10, S11	S4, S5
Fe2-Al2	S1, S4, S10	S8, S11, S12

Another mode that exhibits a remarkable T-anomaly is S15 (second order Raman).

The vanishing of the S15 mode above T_c (250 K) suggests that it may be associated with two-magnon Raman scattering. From the energy of the two-magnon band, an estimate of the nearest-neighbor exchange coupling parameter J_o can be made. If deviations in spins are created on the adjacent sites, the two-magnon energy is given by $J_o(2 \cdot S \cdot z - 1)$, where S is the spin on the magnetic site (Fe³⁺ here, with $S = 5/2$) and z ($z = 6$) is the number of the nearest neighbours to that site. Using $\omega = 1240 \text{ cm}^{-1}$ (at 5 K), the estimated value of the exchange parameter J_o is $\sim 5.3 \text{ meV}$. This value is close to our first-principles calculations of $J_o \approx 6 \text{ meV}$, confirming that the S15 peak is two magnon peak which disappears above T_c .

5.2.4 Conclusions

We explored the richness in effects of (Al, Fe) anti-site disorder on phonons and magnetic ordering. We have shown that strong coupling between the spin and lattice degrees of freedom lead to the observed hardening and phonon anomaly involving disappearance of modes above the magnetic transition temperature. Results in this work suggest that the strong spin-phonon coupling is the key to understand the underlying physics responsible for various exotic physical phenomena in these materials.

5.3 Magnetoelectric and Multiferroic nature of GaFeO₃, AlFeO₃ and related oxides[‡]

5.3.1 Introduction

GaFeO₃, AlFeO₃ and related oxides are ferrimagnetic exhibiting magneto-dielectric effect [102, 106, 107]. There has been no evidence to date for ferroelectricity, and hence multiferroicity in these oxides. Recent experiments by Rana *et. al.* have shown that these oxides as well as oxides of the composition Al_{1-x-y}Ga_xFe_{1+y}O₃ are multiferroic in nature [117]. AlFeO₃ and GaFeO₃ exhibit spontaneous polarization with peak pyroelectric currents at 103 K and 90 K respectively (see Figure 5.3.1). We argue that a possible

[‡]This work has been published in part in Solid State Communications [117]. Copyright (2012) by Elsevier.

origin of this observed ferroelectricity is in the broken inversion symmetry in ordering of collinear magnetic moments particularly as a consequence of anti-site disorder. We report first-principles calculations to corroborate this scenario of the mechanism of the observed ferroelectricity.

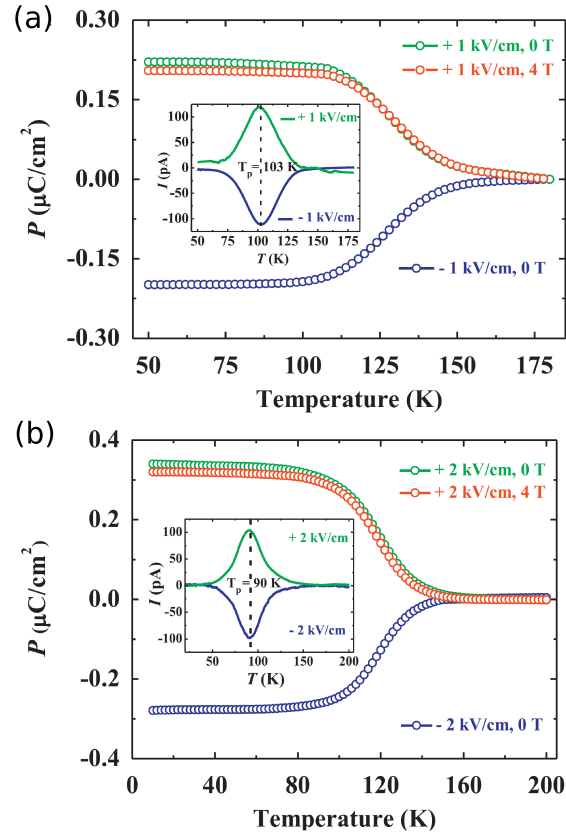


Figure 5.8: Variation of electric polarization (P) as a function of temperature at +ve and -ve poling for (a) AlFeO_3 and (b) GaFeO_3 (after leakage subtraction) along with the effect of a 4 T magnetic field. This work has been done by Saha *et al.* [117]. Copyright (2012) by the Elsevier.

5.3.2 Computational Methods

See section 5.1.2 for details of the first-principles calculations. Minimum energy states with different magnetic ordering were obtained through appropriate initialization of the spins on Fe sites, simulating a unit cell containing 8 formula units (f.u.) of GaFeO_3 i.e. a unit cell of 40 atoms.

5.3.3 Results and Discussion

Since the experimental sample is polycrystalline, precise crystallographic direction of its spontaneous polarization cannot be determined from the results of pyroelectric measurements. We present an argument purely based on symmetry and disorder to explain a possible origin of the observed ferroelectricity. GaFeO₃ belongs to an orthorhombic structure with a non-centrosymmetric space group (Pna2₁). In this structure, polarization along z-axis can be non-zero because of lack of inversion symmetry, and there is no symmetry that involves a reflection in *xy* plane. We note that P_z is not switchable (cannot be reversed on the application of electric field of opposite direction).

Table 5.8: Magnetic moments on individual Fe ions (μ_B) in the ordered and disordered AFM state. Copyright (2012) by Elsevier [117]

Atom no.	Cation site	Magnetic moment (μ_B)	
		ordered	disordered
1	Fe1	3.62	3.71
2	Fe1	3.62	3.51
3	Fe1	3.62	3.70
4	Fe1	3.62	3.62
5	Fe2/Ga2	-3.59	-3.75
6	Fe2	-3.59	-3.62
7	Fe2	-3.59	-3.61
8	Fe2	-3.59	-3.59

However, the anti-site disorder between Fe and octahedral Ga sites is known to be present in the experimental samples. In the absence of such disorder, magnetic ordering of GaFeO₃ in its ground state is antiferromagnetic (AFM): Fe at Fe1 and Fe2 sites have antiparallel spins. We note that the effective interaction among Fe at Fe1 sites (or Fe at Fe2 sites) is ferromagnetic, whereas that between Fe at Fe1 and Fe2 sites is antiferromagnetic, and is expected to lead to magnetic frustration in GaFeO₃. One of the symmetry operations of Pna2₁, ($\bar{x}, \bar{y}, z+1/2$), transforms a pair of Fe1 sites to the other of Fe1 sites.

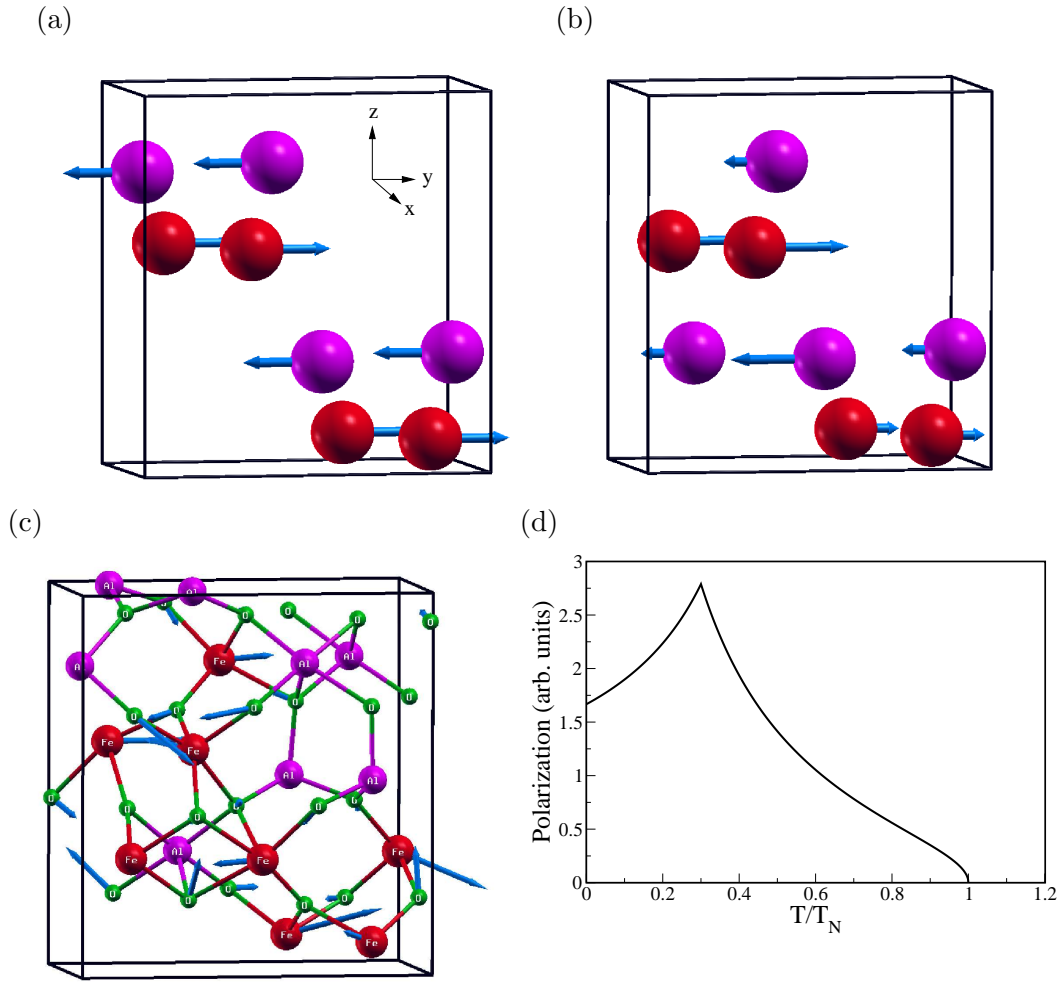


Figure 5.9: (a) Magnetic structure of GaFeO_3 , without anti-site defect and (b) with anti-site defect. Red represents Fe1 sites and pink Fe2 sites. (a) In the ordered state, magnetic moments on Fe1 sites are equal and opposite to Fe2 sites. Hence they don't break inversion symmetry in 'ab' plane. (b) Due to anti-site defect, one of the Fe at Fe2 site is displaced to the Ga2 site. Also the magnetic moments at the four Fe1 or Fe2 sites no longer remain equal. The inversion symmetry in 'ab' plane is broken which permits spontaneous polarization in the same plane. (c) Forces acting on the ions when the system goes from AFM to paramagnetic state. Forces are proportional to the first order spin-phonon coupling (Δ) responsible for non-zero spontaneous polarization in $(\text{Al,Ga})\text{FeO}_3$. (d) Variation of polarization with temperature within our spin-phonon coupling theory. The temperature variation of magnetization and frequency was approximated from the Landau theory of phase transitions. It is evident that system shows non-zero polarization below T_N in the presence of disorder [117].

As the magnetic moments of Fe at all the Fe1 sites are equal and opposite of those at Fe2 sites (refer to Table 5.8 and Figure 5.9), the magnetic structure preserves C_{2z} rotational

symmetry. Thus, it has the planar inversion symmetry (\bar{x}, \bar{y}, z) in the xy plane, and cannot have $P_x, P_y \neq 0$.

The most likely anti-site disorder exists between Fe and Ga at Fe2 and Ga2 sites due to nearly same ionic radii of Fe^{3+} (0.65 Å) and Ga^{3+} (0.62 Å) in octahedral coordination [102]. We have simulated this disorder by interchanging one of Fe at an Fe2 site with one Ga at Ga2 site in a single unit cell (which corresponds to 12.5 % of anti-site defects) in the AFM state (where Fe at Fe1 and Ga2/Fe2 have antiparallel spins). Though the ordered state is energetically more favourable than the disordered state, the difference in their energies is only 32 meV/f.u. [102]. Due to this anti-site defect with Ga at Fe2 site and magnetic frustration, magnetic moments on Fe ions at the four Fe1 sites no longer remain equal and the same holds for Fe at Fe2 sites (refer to Table 5.8 and Figure 5.9b). Such magnetic order breaks the inversion symmetry at least locally in ‘ ab ’ plane and permits a non-zero polarization in the ‘ x ’ and ‘ y ’ directions.

We note that the inversion symmetry is broken due to anti-site disorder even in the absence of magnetic ordering in the system. This leads to non-zero polarization in ‘ x ’ and ‘ y ’ directions. But the polarization induced purely by the anti-site disorder is not switchable. $\text{Al}_{1-x}\text{Ga}_x\text{FeO}_3$ compounds exhibit a strong spin-phonon coupling [102], which is manifested in anomalies in their Raman spectra close to magnetic transitions [116]. Due to the unequal magnetic moments developed on the Fe ions in the presence of anti-site defects, unequal forces are exerted on the ions which lead to small structural distortions. These non-centrosymmetric structural distortions due to spin-phonon coupling are switchable with field, and induce a switchable non-zero P_x and P_y . We consider a phonon (μ) coupling strongly with the spin. It involves oxygen displacements and softens with decreasing temperature [116]. Its first order spin-phonon coupling (Δ) is reflected in the forces on atoms due to change in magnetic ordering (refer to Figure 5.9c).

We now give a phenomenological theory to explain the observed polarization arising from magnetic order and spin-phonon coupling. Let ω_μ , Z_μ^* and u_μ denote the frequency, mode effective charge and displacements of the ions associated with μ which couples to spin. M and E are magnetic order parameter and applied electric field respectively. The

expression for the free energy (F) is:

$$F = -\Delta M(T)u_\mu + \frac{1}{2}\omega_\mu(T)^2 u_\mu^2 - Z_\mu^* E u_\mu. \quad (5.5)$$

For $T < T_N$, minimizing the free energy w.r.t. u_μ

$$u_\mu = \frac{Z_\mu^* E + \Delta M(T)}{\omega_\mu(T)^2}. \quad (5.6)$$

Polarization (P) associated with structural distortion can be obtained as:

$$\Omega \cdot P = Z_\mu^* u_\mu = \frac{Z_\mu^{*2} E}{\omega_\mu(T)^2} + \frac{\Delta Z_\mu^*}{\omega_\mu(T)^2} M(T), \quad \Omega \text{ is the volume.} \quad (5.7)$$

First and second terms in equation 5.7 are the dielectric and spin-phonon coupling contributions to polarization respectively. The polarization induced due to spin-phonon coupling is thus directly proportional to the magnetic order parameter ($M(T)$), first order spin-phonon coupling (Δ), and inversely proportional to square of the phonon frequency ($\omega^2(T)$). Within Landau theory one can show,

$$M(T) \propto (T_N - T)^{\frac{1}{2}},$$

and

$$\omega_\mu(T)^2 \propto |(T_P - T)|.$$

Here, T_N and T_P are the Neil temperature and temperature of peak in pyroelectric current respectively. This dependence of polarization on magnetization, spin-phonon coupling and frequency of phonon gives a non-zero value of polarization at temperatures below T_N ($T_P < T_N$, refer to Figure 5.9d). Such magnetostriction is expected to give rise to observable electromagnons [118] in these compounds. To estimate this, we have carried out first-principles calculations of the structure with the magnetic configuration obtained with

time-reversed spins. We find that changes in structure involve rather small displacements of ions ($\sim 10^{-3}$ Å) and are within the errors in DFT calculations indicating a rather weak ionic contribution to magnetoelectric coupling.

From the temperature dependent polarization estimated from pyroelectric current measurements, we note that it is non-zero well above T_P , and magnitude of the pyroelectric current even 60 K above T_P is comparable to its values at low temperatures. Thus, the pyroelectric current that is switchable with electric field clearly shows a broken inversion symmetry well above T_P . Within the model which we use here to explain the observed results, a non-zero polarization arises from the broken inversion symmetry associated with magnetic ordering that occurs at a higher temperature (T_N). However, magnitude of such a polarization is typically rather small [25], of the order of $0.05 \mu\text{C}/\text{cm}^2$, and is even smaller in the present case due to partial cancellation due to disorder. Once the magnetic order becomes strong enough, phonons make an additional contribution to polarization (and pyroelectric current), and giving rise to a maximum in pyro-current at T_P . In this sense, (Al,Ga)FeO₃ seems to go through another improper transition at lower temperatures. While the leakage currents are likely to affect the pyroelectric current measurements on a polycrystalline sample, it would have increased with temperature which is not observed in the measurements, thus supporting our model of the origin of polar order.

The pyroelectric measurements of spontaneous polarization can be used to obtain an insight into the main contributors to ferroelectricity. These measurements of P_s in GaFeO₃, show an asymmetry w.r.t. the poling field applied during sample cooling (see Figure 5.3.1b). Unlike P_x and P_y , the sign of the pyroelectric current due to non-switchable P_z does not change on reversing the poling field. Hence, the spontaneous polarization which has both switchable (P_x and P_y) and non-switchable (P_z) contributions gives rise to this asymmetry. The difference in the total polarization of positively poled and negatively poled sample gives an estimate of contribution from pyroelectric change in P_z , which is $\sim 0.075 \mu\text{C}/\text{cm}^2$. Since the remainder of the polarization comes from P_x and P_y , our observation of switchable spontaneous polarization (*i.e.* ferroelectricity) in GaFeO₃ is quite robust. Thus, the ferroelectricity in GaFeO₃ is induced by non centrosymmetric

magnetic ordering which emerges from inherent magnetic frustration in these compounds, arising from the anti-site disorder and spin-phonon coupling.

5.3.4 Conclusions

We have shown that the anti-site disorder in $\text{Al}_{1-x}\text{Ga}_x\text{FeO}_3$ systems breaks the inversion symmetry in the ‘xy’ plane, and leads to non-zero inplane polarization. This polarization however has (a) a non-switchable part due to anti-site defects themselves, and (b) switchable part coming from the structural distortions induced by spin-phonon coupling. Thus, a strong interplay between spin, structure and anti-site defects induces ferroelectricity, and hence multiferroic behaviour in these oxides. Our Landau-like phenomenological theory shows that observed polarization is non-zero below the Neel temperature and arises from non-centrosymmetric magnetic order and spin-phonon coupling.

Chapter 6

Emergence of Ferroelectricity at a Metal-Semiconductor Transition in 1T Monolayer of MoS₂ *

6.1 Introduction

While two dimensional (2D) materials like graphene and MoS₂ are promising for high speed-low power nanoelectronic devices, incorporation of a smart functional property like ferroelectricity can significantly enhance the range of their applications to sensors, actuators and memories [13–15]. Ferroelectrics are typically insulators that exhibit a macroscopic electric polarization arising from spontaneous ordering of electric dipoles which can be controlled by external electric and stress fields. In ultra-thin films however, ferroelectric dipoles perpendicular to the film surface are suppressed by their depolarizing field and ferroelectricity has been shown to disappear below film thicknesses of 24 Å in BaTiO₃ [119], 12 Å in PbTiO₃ [120] and 10 Å in polymer films [121]. While truly 2D materials such as graphene [40], BN [75] and MoS₂ [122] have not been explored for ferroelectricity, they are attractive for (a) addressing the fundamental issue of 2D ferroelectricity, and (b) a possible combination of ferroelectricity and semiconducting transport properties relevant

*This work has been published in Physical Review Letters [162]. Copyright (2014) by the American Physical Society.

to applications. Among these, MoS₂ holds a special promise for being a 2-dimensional ferroelectric semiconductor, as it exhibits polytypes with rich electronic structure [123] and a moderate band gap [124], and has been used effectively in a field effect transistor [125].

6.2 Computational Methods

See section 3.1.2 for details of the first-principles calculations. Exchange-correlation energy of electrons was treated within a GGA functional of PW91 parameterized form [31]. To determine the dynamical matrices and phonons for the unit cell at the wavevectors on a mesh, we used DFT linear response as implemented in the Quantum ESPRESSO package. These phonon calculations were carried out with a uniform 10x10x1 mesh of k-points in self consistent field (scf) calculations, and the dynamical matrices were determined over a mesh of 3x3x1 k-points for a unit cell. For the 3x3x1 supercell, the self consistent field (scf) calculations were carried over a 6x6x1 mesh of k-points and dynamical matrices were determined over a mesh of 2x2x1 k-points. The group theoretical analysis was carried out with the help of ISOTROPY package [126] and Bilbao Crystallographic Server [127].

6.3 Polytypes of MoS₂

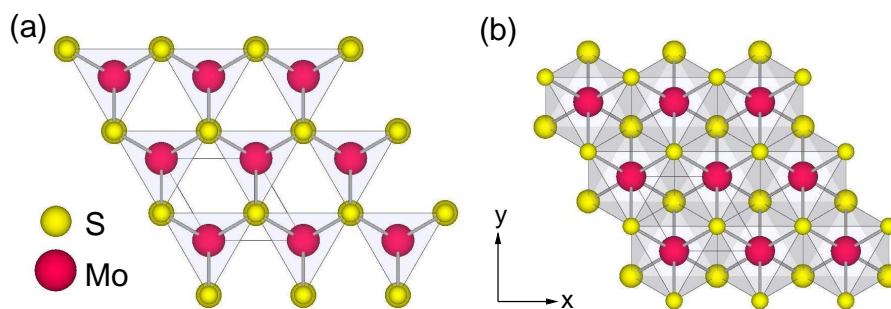


Figure 6.1: Structure of polytypes of MoS₂ monolayers. Top view of the structure of monolayers of MoS₂ in (a) 2H polytypical form with triangular prismatic (six-fold) coordination of Mo atoms and two on-top triangular lattices of sulphur atoms, and (b) 1T polytypical form with octahedral coordination of Mo atoms. To distinguish between the two S planes, the S atoms in the top plane are denoted by a smaller radii than the bottom plane ones.

The common two-dimensional form of MoS₂ has the 2H structure [128] with a honeycomb

lattice decorated by Mo at every alternate site and a pair of S atoms centered at each of the other sites [see Figure 6.1a], exhibiting electronic structure with a band gap of 1.8 eV [124]. Though a monolayer of 2H-MoS₂ is non-centrosymmetric, its polarization vanishes due to other symmetries of the structure, and it is not particularly interesting in the context of ferroelectricity that arises from breaking of structural inversion symmetry with temperature or pressure. Monolayers of MoS₂ can also be synthesized [129,130] in the 1T structure (see Figure 6.1b), in which the two sulphur lattice planes are staggered such that each Mo site becomes the center of inversion making 1T-MoS₂ a promising candidate for ferroelectricity.

We investigate here a possible existence of ferroelectricity in metal chalcogenides through analysis of the electronic and structural stability of their 1T polymorph, with a focus on MoS₂. We present group theoretical analysis to identify order parameters, and derive the form of a Landau free energy function that is relevant to low-energy symmetry breaking structural distortions of the 1T polymorph using ISOTROPY package [126] and Bilbao Crystallographic Server [127]. Inputs to this analysis are derived from accurate first-principles calculations based on density functional theory (DFT).

6.4 Electronic structure of 1T-MoS₂

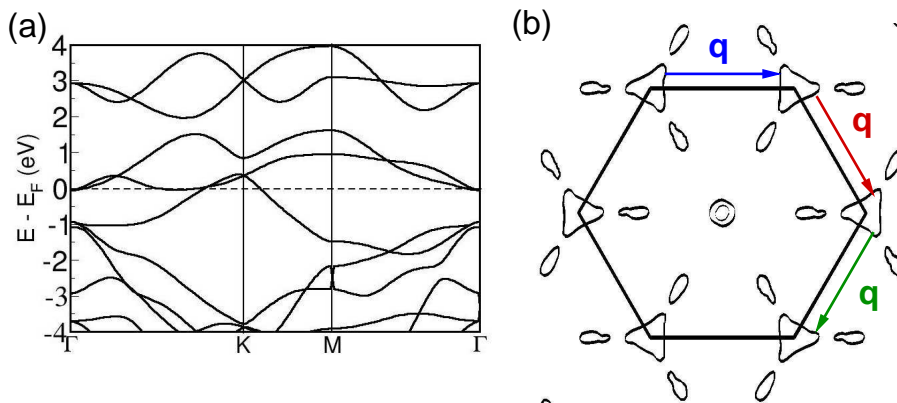


Figure 6.2: Electronic structure of 1T-MoS₂. (a) Electronic structure showing dispersion of energy with Bloch vector (k) of $c1T$ structure and (b) its Fermi surface exhibiting a weak nesting between sides of the triangular pockets centered at K and K' . The nesting vectors (\mathbf{q}) are denoted by red, blue and green arrows.

With a closely knit network of edge-shared MoS_6 octahedra, the centrosymmetric $1T$ ($c1T$) structure of MoS_2 is metallic, evident in the calculated electronic structure (see Figure 6.2a, we note that the bands at the Fermi level arise from 4d-orbitals of Mo). Its Fermi surface (see Figure 6.2b), which separates the occupied valence and unoccupied conduction states of electrons as a function of Bloch wave vector, consists of packets centered at the corner (K) and center (Γ) of the Brillouin zone, each having a three-fold rotational symmetry. The Fermi surface exhibits weak or hidden nesting *i.e.*, many points on the surface are connected by a common nesting wave vector; in this case the three nesting vectors $q = K + \delta K$ (see Figure 6.2b) form an equilateral triangle centered at the valley point K . The average of these three vectors is exactly the valley point K . Since the degeneracy of electronic states associated with nesting of the Fermi surface can be lifted to lower the energy by a spontaneous symmetry breaking field such as a charge density wave [131] or structural distortion, we expect the $c1T$ form to be unstable.

6.5 Vibrational spectrum of $c1T$ - MoS_2 and properties of its cell tripled state

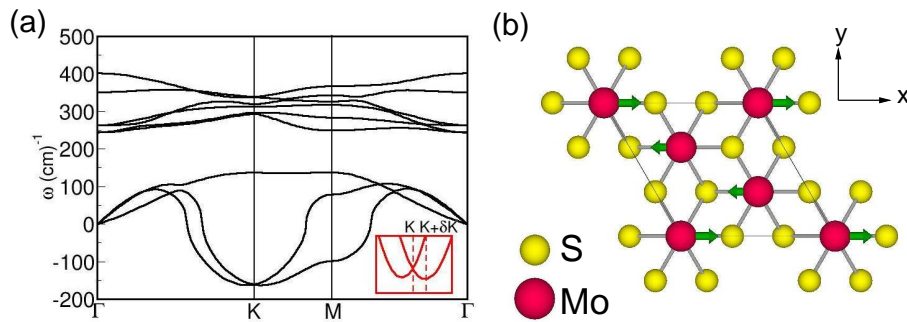


Figure 6.3: Structural instabilities of the centrosymmetric $1T$ ($c1T$) structure of MoS_2 . (a) Phonon dispersion of the $c1T$ structure, with inset showing a zoomed in view of the unstable modes near K point (the strongest instability is at $q = K + \delta K$). (b) Atomic displacements associated with unstable mode at K -point that lead to the cell tripling transition.

Indeed, the calculated phonon dispersion of the $c1T$ structure (see Figure 6.3a) exhibits unstable modes ($w^2 < 0$, w being frequency). Although the strongest instabilities are

at points close to the nesting q -vectors, $q = K + \delta K$'s (see inset of Figure 6.3a), almost equally unstable mode (of K_3 symmetry) at K is doubly degenerate. Thus, there are two modes at K that point to lower the energy through distortion of the $c1T$ structure, as opposed to competing single mode of comparable strength at the Fermi surface nesting vectors ($K + \delta K$'s). As a result, the lowest energy structure is obtained by freezing in the K_3 mode (modulation of the $c1T$ structure). Along with a symmetry-related mode (K'_3) of the same frequency at K' , its overall degeneracy is 4. It involves predominantly Mo displacements in the plane of MoS₂ that leads to Mo-trimerization, analogous to dimerization arising from a Peirel's instability in 1-dimension (see Figure 6.3b).

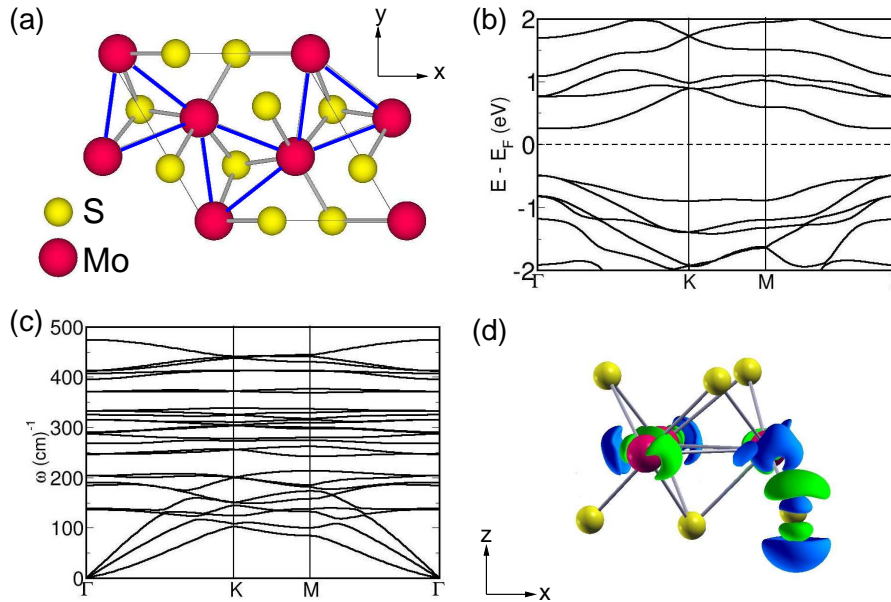


Figure 6.4: Structure and properties of $d1T$ -MoS₂. (a) Trimerization of Mo atoms in the distorted low symmetry $1T$ form with $\sqrt{3} \times \sqrt{3}$ unit cell. (b) Electronic structure and (c) vibrational spectrum of $d1T$ MoS₂. (d) An isosurface of the difference in charge densities of ferroelectric $d1T$ state with up polarization and the $c1T$ state. Green colour denotes negative charge and blue denotes positive charge. The broken inversion symmetry in the charge density difference confirms ferroelectricity in the cell-tripled ground state structure.

As expected, a K_3 -distortion of the $c1T$ structure leads to a lower symmetry cell tripled structure (we call it $d1T$, see Figure 6.4a), that is energetically 0.23 eV/f.u. lower than $c1T$, with reduction in Mo-Mo bond length from 3.19 Å to 2.97 Å. Trimerization of Mo is consistent with the observed $1T$ -structure [129,132]. As the $d1T$ structure is energetically

0.59 eV/f.u. higher than the 2H structure, stabilization of the 1T polymorph against the 2H-MoS₂ requires special consideration in experiment [133]. As the mechanism of this instability involves lifting of degeneracy of the nested Fermi surface, a gap of 0.7 eV opens up in the electronic structure (see Figure 6.4b) marking a metal to semiconductor transition. Phonon dispersion of the resulting *d1T* structure establishes it as a local minimum of energy and confirms its structural stability (see Figure 6.4c).

Table 6.1: In-plane Born effective charges ($Z_{\alpha,\beta}^*$, $\alpha, \beta = x, y$) of *d1T*-MoS₂*.

Atom	direction	x	y
Mo	x	1.7	0.0
	y	0.0	-5.0
Mo	x	-3.5	2.9
	y	2.9	0.1
Mo	x	-3.5	-2.9
	y	-2.9	0.1
S	x	1.9	0.0
	y	0.0	1.2
S	x	-1.6	0.0
	y	0.0	-1.6
S	x	1.1	0.4
	y	-0.4	1.0
S	x	1.4	-0.3
	y	-0.3	1.7
S	x	1.1	-0.4
	y	0.4	1.0

* Note that the volume factor in estimation of polarization and dielectric constants is $(\sqrt{3}/2)a_o^2(c/2)$ (where $c/2 = 6.2 \text{ \AA}$) and c is the bulk lattice constant of *c1T*-MoS₂.

We now make specific predictions for experimental validation of the MIT and structural transition in 1T-MoS₂. Increased local and energetic stability of the *d1T* structure leads

to hardening of Raman active E_{2g}^1 and A_{1g} modes from 246 cm^{-1} and 327 cm^{-1} of $c1T$ to 312 cm^{-1} and 407 cm^{-1} respectively. The frequency of A_{1g} mode of $2H$ -phase (405 cm^{-1}) is close to that of $d1T$ (407 cm^{-1}), the E_{2g}^1 mode of the $d1T$ (312 cm^{-1}) is much softer (by $\approx 70 \text{ cm}^{-1}$) than that of the $2H$ -phase (381 cm^{-1}), and is thus a clean Raman signature to detect the $d1T$ structure. The signatures of MIT are typically reflected in the response of a material to electric field [134], and we focus on the semiconducting $d1T$ phase and determine (a) the force felt by an ion due to applied field given by the Born effective charge (Z^*), and (b) electronic dielectric constant (ϵ^∞). We find a highly anomalous Z^* of Mo ion (-5), and that of all S to be +2.0 (for an in-plane electric field, see Table 6.1). Even the sign of these charges is counter-intuitive (nominal charge of Mo being +4 and S being -2), and its origin can be traced through band-by-band decomposition to the d -states of Mo just below Fermi energy, which are also involved in opening of a gap through trimerization of Mo atoms. Secondly, our calculations show that most of the contribution to static dielectric constant ($\epsilon_{xx} = 15.87$, $\epsilon_{yy} = 15.76$ and $\epsilon_{zz} = 1.77$) comes from electrons ($\epsilon_{xx}^\infty = 12.30$, $\epsilon_{yy}^\infty = 12.30$ and $\epsilon_{zz}^\infty = 1.77$), reflecting on their fundamental role in the mechanism of MIT and the structural instability.

From the difference in charge density of the $d1T$ and $c1T$ structures (see Figure 6.4d), we find a change in charge density localized only on one of the sulphur atoms showing that the $d1T$ structure is clearly non-centrosymmetric. Berry phase calculations reveal a spontaneous polarization of $\approx 0.28 \mu\text{C}/\text{cm}^2$ ($0.18 \mu\text{C}/\text{cm}^2$ on the application of dipole correction to eliminate the fictitious field arising out of the continuity of electrostatic potential at the supercell boundary) along the z -axis, while the in-plane polarization vanishes. The structural distortion of a K_3 mode involves a periodic array of dipole moments that average to a vanishing polarization. Thus, a nonzero polarization has to arise from a nonlinear coupling of K_3 mode with polar mode [26]. Note that the volume factor in estimation of polarization and dielectric constants is $(\sqrt{3}/2)a_o^2(c/2)$ (where $c/2 = 6.2 \text{ \AA}$), and c is the bulk lattice constant of $c1T$ - MoS_2 .

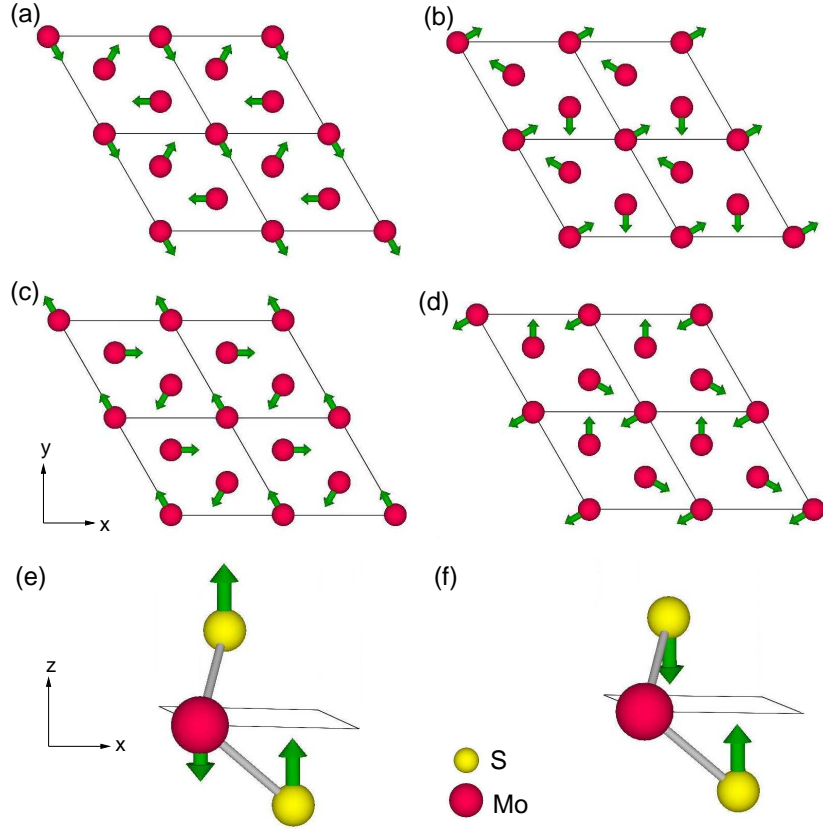


Figure 6.5: Atomic displacements defining the order parameters of Landau theory. Displacement of Mo atoms associated with order parameters (a) η_1 , (b) η_2 , (c) η_3 and (d) η_4 , that capture the properties of valley (K_3) phonons (note that displacement of S atoms are not shown here), and yield trimerization of Mo atoms, (e) η_5 is the polar Γ_2^- phonon responsible for polarization, and (f) η_6 has the full symmetry of $c1T$ structure, representing Γ_1^+ phonon of the $c1T$ and out-of-plane expansion of the monolayer. Atomic displacements are denoted by green arrows. Copyright (2014) by the American Physical Society [162].

6.6 Landau Theory

We now use symmetry analysis within a Landau theory to derive a precise form of the coupling responsible for ferroelectricity in the $d1T$ structure. With centrosymmetric $c1T$ as the reference structure, free energy is expressed as a symmetry invariant Taylor series in the relevant structural distortions, called order parameters, that connect $c1T$ to a $d1T$ structure. Symmetrized combinations [126] of K_3 and K'_3 modes form two sets of primary order parameters $S = (\{\eta_1, \eta_2\}$ and $\{\eta_3, \eta_4\})$, giving trimerization of Mo (see Figure 6.5). The polar mode Γ_2^- is the secondary order parameter, η_5 , which involves out-of-plane

Table 6.2: Transformations of Γ_2^- mode *i.e.* η_5 and K_3 and K_3' modes, *i.e.* $(\{\eta_1, \eta_2, \eta_3, \eta_4\})$ under the generators of the $P\bar{3}m1$ space group (164) describing the high-temperature $c1T$ phase.

	E	$2C_3$	$3C_2'$	I	$2S_6$	$3\sigma_d$
Γ_2^-	1	1	-1	-1	-1	1
K_3	2	-1	0	0	0	0
K_3'	2	-1	0	0	0	0

displacement of sulphur sublattices relative to the Mo sublattice inducing a polarization along z-axis. Another secondary order parameter (η_6) is associated with changes in the effective thickness of the $1T$ monolayer, *i.e.* Γ_1^+ mode with the full structural symmetry of $c1T$ (see Figure 6.5f), for simplicity we omit the contribution of the Γ_1^+ mode in our analysis here). The transformations of Γ_2^- , K_3 and K_3' modes under the generators of the $P\bar{3}m1$ space group (164) describing the high-temperature $c1T$ phase are given in Table 6.2.

Free energy is written as a symmetry-invariant Taylor expansion in order parameters $\{\eta_1, \eta_2, \eta_3, \eta_4, \eta_5\}$:

$$\begin{aligned}
F = & g_{12}[(T - T_c)/T_c] (\eta_1^2 + \eta_2^2 + \eta_3^2 + \eta_4^2) + g_{22} \eta_5^2 \\
& + g_{13} (\eta_1^3 - 3 \eta_1 \eta_2^2 + \eta_3^3 - 3 \eta_3 \eta_4^2) \\
& + g_{23} \eta_5(\eta_1^2 + \eta_2^2 - \eta_3^2 - \eta_4^2) \\
& + g_{14} [(\eta_1^2 + \eta_2^2)^2 + (\eta_2^2 + \eta_3^2)^2 + (\eta_3^2 + \eta_4^2)^2 + (\eta_4^2 + \eta_1^2)^2 \\
& + (\eta_3^2 + \eta_1^2)^2 + (\eta_4^2 + \eta_2^2)^2 - 2\eta_1^4 - 2\eta_2^4 - 2\eta_3^4 - 2\eta_4^4] \\
& + g_{24} [(\eta_1^2 + \eta_2^2)^2 + (\eta_3^2 + \eta_4^2)^2] \\
& + g_{34} \eta_5(\eta_1^3 - 3 \eta_1 \eta_2^2 + \eta_3^3 - 3 \eta_3 \eta_4^2) \\
& + g_{44} \eta_5^2(\eta_1^2 + \eta_2^2 + \eta_3^2 + \eta_4^2) + g_{54} \eta_5^4.
\end{aligned} \tag{6.1}$$

where T_c is the Curie temperature, and $g_{\alpha\beta}$'s are coefficients that are determined from

first-principles calculations (see Table 6.3). Minimization of free energy in the $\{\eta_1, \eta_5\}$ subspace gives

$$\eta_5 = -\frac{g_{23}}{2g_{22}}\eta_1^2, \quad (6.2)$$

clearly showing that the polarization is induced as a quadratic function of η_1 which becomes non-zero below the transition temperature (implying improper nature of ferroelectricity).

Table 6.3: Landau coefficients (g).

coefficient	value
g_{12}	0.7095 eV/Å ²
g_{22}	7.8636 eV/Å ²
g_{13}	-0.4459 eV/Å ³
g_{23}	0.8906 eV/Å ³
g_{14}	3.8614 eV/Å ⁴
g_{24}	-2.5110 eV/Å ⁴
g_{34}	1.0326 eV/Å ⁴
g_{44}	2.7749 eV/Å ⁴
g_{54}	0 eV/Å ⁴

The coefficients (g) in Landau free energy function are obtained by fitting to first-principles calculations, *i.e.* by freezing in various amplitudes of η 's and obtaining the total energies. The Free energy expression (F) is then fit to the total energies obtained from first-principles. Note that g_{22} is 4.3059 eV/Å² in the absence of depolarizing field.

We have thus shown that d1T-MoS₂ is an *improper* ferroelectric, where the primary order parameter is the unstable modes with K_3 symmetry and the polarization (P) is the secondary order parameter (corresponding to polar mode with Γ_2^- symmetry) that arises from its non-linear coupling with the K_3 mode. The depolarization field does *not* influence the primary ordering of the K_3 mode which gives most of the energy gain through distortion of the structure. Once the primary ordering occurs, the secondary order (of polarization) is guaranteed by symmetry even if the energy gain associated with it is

small. In fact, there is no instability associated with polarization, and the depolarization field only slightly hardens the Γ_2^- mode. Thus, the further energy gain associated with it is reduced by the depolarization field, but the dominant mechanism of the instability involves K_3 mode. In the case of $d1T$ MoS₂, the gain in energy by K_3 mode distortion (0.42×10^{-2} eV/Å³) is much larger than the depolarizing energy (0.16×10^{-5} eV/Å³). Thus, the depolarizing field does not succeed in suppressing the single domain ferroelectric state. This is also evident in our calculated phonon dispersion of the $d1T$ structure, which exhibits no instabilities (see Figure 6.4c). These arguments are quite similar to the ones detailed in the work on the presence of thickness limits in improper ferroelectrics by Na Sai *et al.* [135], which we find realized in $1T$ -MoS₂. Note that, the effects of depolarizing field are included in g_{22} .

The temperature dependence of polarization (Figure 6.6a, where $P \propto \eta_5$ and dielectric susceptibility χ is $\propto 1/\frac{\partial^2 E}{\partial P^2}$ at $\{\eta_1$ to $\eta_5\}$ which minimize Landau free energy at a given temperature) predicted by the Landau theory (a) is almost linear reflecting on its geometric or improper origin [26, 27] of ferroelectricity, and (b) exhibits a weak discontinuity at the transition temperature, slightly above T_c . The latter and accompanying change in the slope of dielectric susceptibility at the transition reveal its first order character arising from the cubic dependence of free energy on η_1 (see Figure 6.6b). The dielectric anomaly is quite distinct from the one in conventional (proper) ferroelectrics. A mean field estimate of the transition temperature, obtained from the energy well-depth of 0.23 eV/f.u. is well above room temperature, but is bounded above by the temperature of stability of $1T$ polymorph.

The nontrivial geometry and symmetry of the 4-dimensional structural subspace $\{\eta_1, \eta_2, \eta_3, \eta_4\}$ are essential to establish the existence of states with opposite polarization and switchability, and hence the ferroelectricity of $d1T$ structure (see Table 6.4). In the $\{\eta_1, \eta_2\}$ plane, we find three minima of energy (see Figure 6.6b and Figure 6.6c) corresponding to symmetry equivalent $d1T$ structures with polarization of the same sign, $P_z \approx 0.22$ $\mu C/cm^2$ (comparable to our estimate from first-principles). These semiconducting states are separated from each other by semi-infinite lines corresponding to metallic states

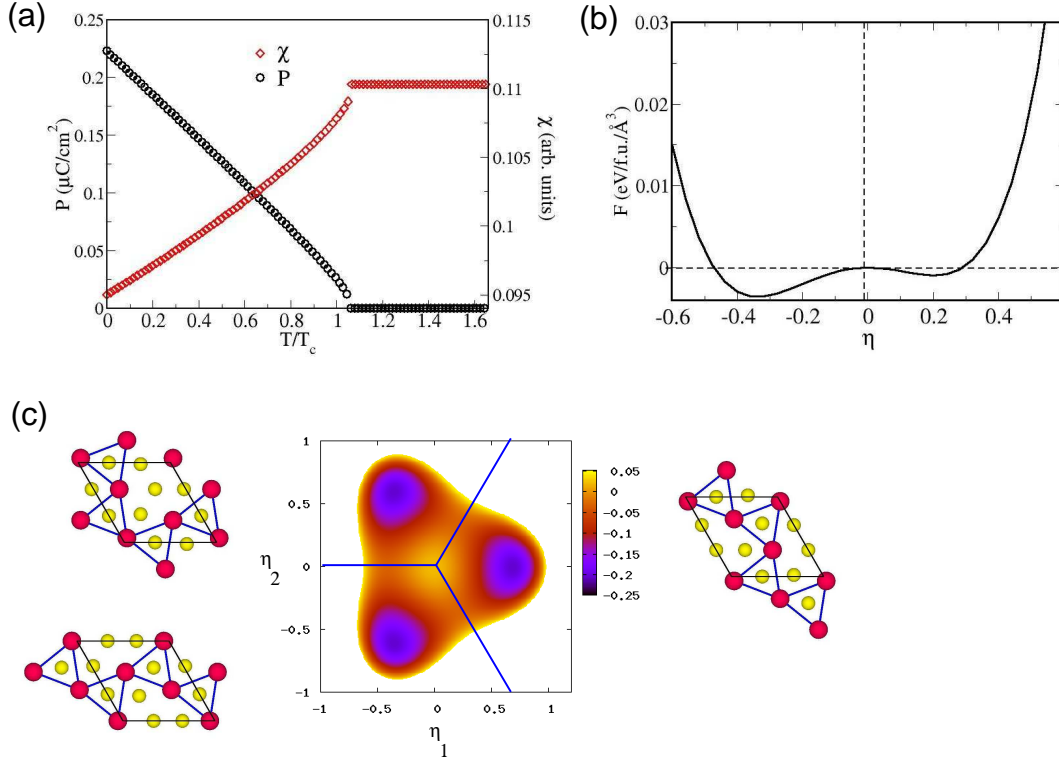


Figure 6.6: Ferroelectric transition behavior, Landau free energy landscape and metallic states of $d1T$. (a) Polarization (P) and dielectric susceptibility (χ) as a function of temperature, derived from Landau theory. (b) Variation of Landau Free energy (F) with η . F is minimized w.r.t c where $\eta = \{\eta_1, \eta_2 = \sqrt{3}\eta_1, \eta_3 = 0, \eta_4 = 0, \eta_5 = c\}$. Note that, cubic dependence of free energy on η *i.e.* the first order nature of the phase transition is reflected in the two unequal minima. (c) Contour plot of Landau free energy as a function of $\{\eta_1, \eta_2, 0, 0, -0.039\}$ at $T = 0$ K, and structures corresponding to the local minima each of which involves trimerization of Mo. Semi-infinite blue lines in the $\{\eta_1, \eta_2\}$ plane correspond to metallic states.

(see Figure 6.6c). Application of inversion symmetry transforms a $d1T$ structure in the $\{\eta_1, \eta_2\}$ plane to that in the $\{\eta_3, \eta_4\}$ plane with reversed polarization.

6.7 Polarization switching

Our free energy based estimate of the intrinsic coercive field (E_c) to switch the sign of polarization is unrealistically large. In most ferroelectrics, switching is facilitated by nucleation and growth of domains of polarization at heterogeneously distributed defect sites.

Table 6.4: Contribution of η_1 to η_5 to the ferroelectric up and down polarized states, obtained by projecting structural distortions of the $d1T$ state on the order parameters (see Figure 6.5). η_1 to η_4 are the primary order parameters, and η_5 is the secondary order parameter.

order parameter	up polarization	down polarization
η_1	0	-0.323
η_2	0	-0.559
η_3	-0.323	0
η_4	-0.559	0
η_5	0.047	-0.047

We now explore the structure and properties of domain walls that are relevant to polarization switching under experimental conditions. The domain wall energy (D_w) was estimated by subtracting the energies of up and down polarized domains from the configuration with both up and down polarized domains. The area was calculated as the product of length of domain wall and $c/2$ (where c is the lattice constant along ‘z’ direction of bulk MoS₂).

$$D_w = \frac{E(\text{domain configuration}) - E(\text{up state}) - E(\text{down state})}{\text{domain wall length} \times c/2}. \quad (6.3)$$

Our estimate of D_w that separates domains of up and down polarization of $d1T$ (see Figure 6.7a) structure is ≈ 7.7 mJ/m², quite comparable to that of ferroelectric BaTiO₃ [136].

Estimation of coercive field is quite challenging even for simpler, conventional ferroelectrics like BaTiO₃. In fact, the intrinsic coercive (switching) field (which is easier to estimate) is always much larger than that measured in experiments, as the mechanism of switching at the intrinsic coercive field involves homogeneous nucleation of domains of opposite polarization. Such field can be estimated from Landau theory, and its estimate from the Landau theory presented here is indeed unrealistically large. Polarization switching in most ferroelectrics is based on heterogeneous nucleation and growth of domains, in which defects (extrinsic mechanism) act as the nucleating seeds. To estimate such the coercive

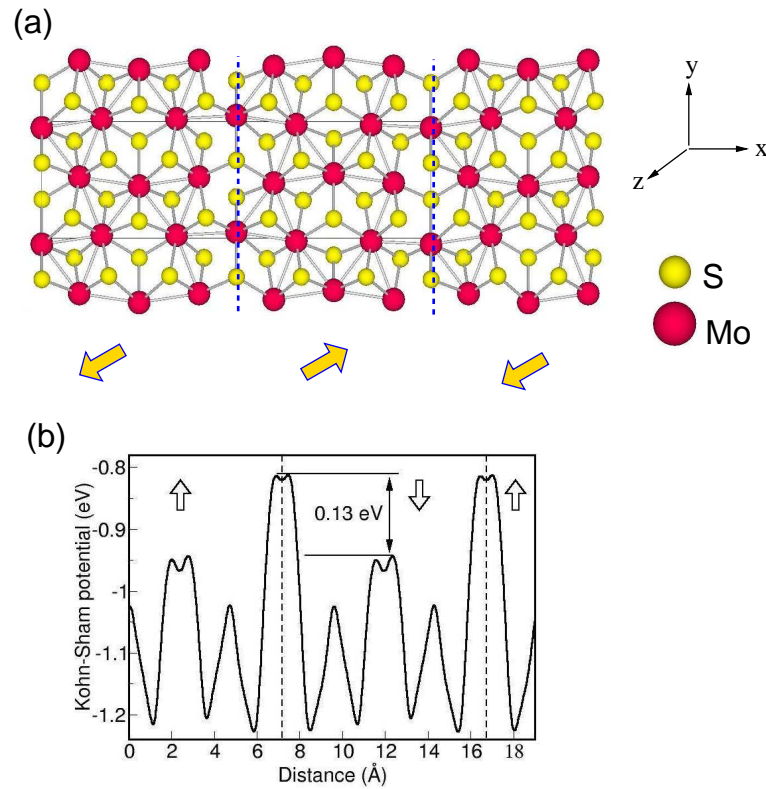


Figure 6.7: Ferroelectric domain wall in $1T$ -MoS₂. (a) Structure of the domain wall (blue dashed line) between up and down polarized states of $d1T$. (b) Variation of Kohn-Sham potential at the interface of up and down polarized domains. The energy barrier at the domain wall (marked with dashed lines) separating domains with opposite polarization is ≈ 0.13 eV. This barrier is estimated by taking the macroscopic average of the Kohn-Sham potential in the ‘yz’ plane for every point on the line perpendicular to the domain wall (*i.e.* ‘x’ direction), which gives the variation in the Kohn-Sham potential across the interface of up and down polarized domains.

field of MoS₂, we used its most common defect, the S vacancy [137]. From the simulations with a large supercell containing vacancy, we find that the size of such a point defect in MoS₂ is about 12-16 Å. Using this, the domain wall energy and spontaneous polarization in the model by Shin *et al.* [138], our estimate of the realistic coercive field (within an order of magnitude) in $d1T$ MoS₂ is about 2.3×10^7 V/cm. While this is still 10 times higher than the coercive field of a conventional ferroelectric like BaTiO₃, it is achievable in realistic MoS₂ devices [125].

6.8 Dipolelectronic devices

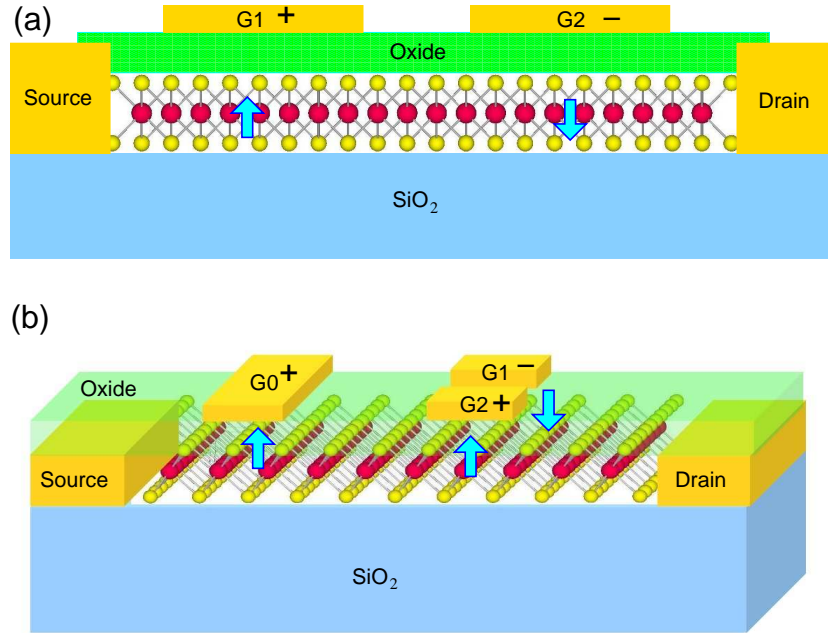


Figure 6.8: Schematic of logic gates. (a) X-NOR and (b) NAND logic gate. G1 and G2 are the gate electrodes, and G0 is the electrode for the offset voltage. Solid blue arrows indicate direction of polarization.

We find a barrier of 0.13 eV in the electrostatic potential (see Figure 6.7b) at the domain wall, which can be used to alter the electron transport in $1T$ - MoS_2 channel. For example, an XNOR gate (see Figure 6.8a and Table 6.5) can be developed using a field effect transistor (FET) with $d1T$ MoS_2 as a channel and two gate electrodes in series, whose voltages control the dipolar structure. When both the gates are at the same potential, the single domain of $1T$ - MoS_2 carries a large current (on state). On the other hand, opposite potentials at the two gates stabilize a domain structure carrying little current (off state). Based on the same principle, NAND and OR gates can be realized in an FET device with three gate electrode (see Figure 6.8b and Table 6.6). Since the semiconducting channels in these devices are made of monolayers of $d1T$ - MoS_2 , they involve the coupling between the dipoles (polarization) and electrons, and we term them as *dipolelectronic* devices.

Table 6.5: Truth table for XNOR gate. V_{G1} and V_{G2} are the potentials at the G1 and G2 gate electrodes respectively.

V_{G1}	V_{G2}	Output
+V	+V	on
+V	-V	off
-V	+V	off
-V	-V	on

Table 6.6: Truth table for NAND and OR gates. V_{G1} and V_{G2} are the potentials at the G1 and G2 gate electrodes respectively. V_{G0} is the offset potential at G0 electrode*.

Gate	V_{G0}	V_{G1}	V_{G2}	Output
NAND	+V	+V	+V	on
	+V	+V	-V	on
	+V	-V	+V	on
	+V	-V	-V	off
OR	-V	+V	+V	off
	-V	+V	-V	on
	-V	-V	+V	on
	-V	-V	-V	on

* Change in the voltage at offset gate G0 leads to transformation from NAND to OR gate.

6.9 Conclusions

Our work establishes that ferroelectricity in $d1T$ -MoS₂ is a robust consequence of symmetry of K_3 modes whose instability originates from the degeneracy of Fermi surface and a strong electron-phonon coupling [139], which is also known to be relevant to the competing instabilities of superconductivity [140] and charge density waves [131, 141] in layered

dichalcogenides. Experimental observation of trimerization of Mo atoms in the $d1T$ structure by Wypych *et al.* [129] is in agreement with our structure. We show that there exists a non-linear coupling between the structural distortion leading to the trimerization of Mo atoms and the polar Γ_2^- mode of 1T-MoS₂ that gives rise to switchable polarization in its monolayer. Hence, we expect this work to be a stimulant to extensive experimental investigations for finding the presence of ferroelectricity in a monolayer of 1T-MoS₂. While opening up a small bandgap desirable for high mobility and on/off ratio of a transistor, the electron (carriers) - phonon (dipoles) coupling is the key to the novel dipolelectronic devices. Furthermore, the vicinity of the $d1T$ structure to an MIT makes it attractive for use in devices based on electro-resistive properties as well as in chemical sensors and catalytic structures. Also, 2-dimensional heterostructures consisting of $d1T$ interfacing with $2H$ polymorphs of MoS₂ can introduce more functionality in its devices [125]. Our symmetry analysis applies equally well to $1T$ form of other transition metal (M) di-chalcogenides, MX₂ (M= Mo, W and X= S, Se), which may exhibit richness of such properties.

Chapter 7

Selenium

7.1 Multiferroic behaviour in elemental Selenium*

7.1.1 Introduction

Magnetoelectric multiferroics are materials in which ferromagnetism and ferroelectricity coexist. Since the ferroelectric and magnetic orders are intrinsically coupled in multiferroics, these materials are of great technological interest and have been a subject of intense research. Due to the mutually exclusive nature of ferromagnetism and ferroelectricity (mainly in oxides [143]), along with symmetry restrictions and conflicting chemical requirements, very few materials exhibit multiferroic behaviour. A possible solution is offered by systems in which different ions or functional groups are responsible for different types of ferroic order. In such ‘Type-I’ multiferroics, magnetism and ferroelectricity originate independently from different sublattices (e.g., BiFeO₃) [114,144] and necessarily exhibit a weak coupling. In ‘Type-II’ multiferroics, on the other hand, ferroelectricity is induced by certain types of non-collinear (e.g., cycloidal) spin order that breaks inversion symmetry. Such systems (that include certain rare earth manganites) [25,145] show a strong coupling between the ferroelectric and magnetic order parameters.

Very recently, a particularly interesting connection has been suggested between multiferroic systems and topological insulators [146,147]. We show that *elemental selenium* is a

*This work has been published in part in Scientific Reports [142]. Copyright (2013) by Nature Publishing Group.

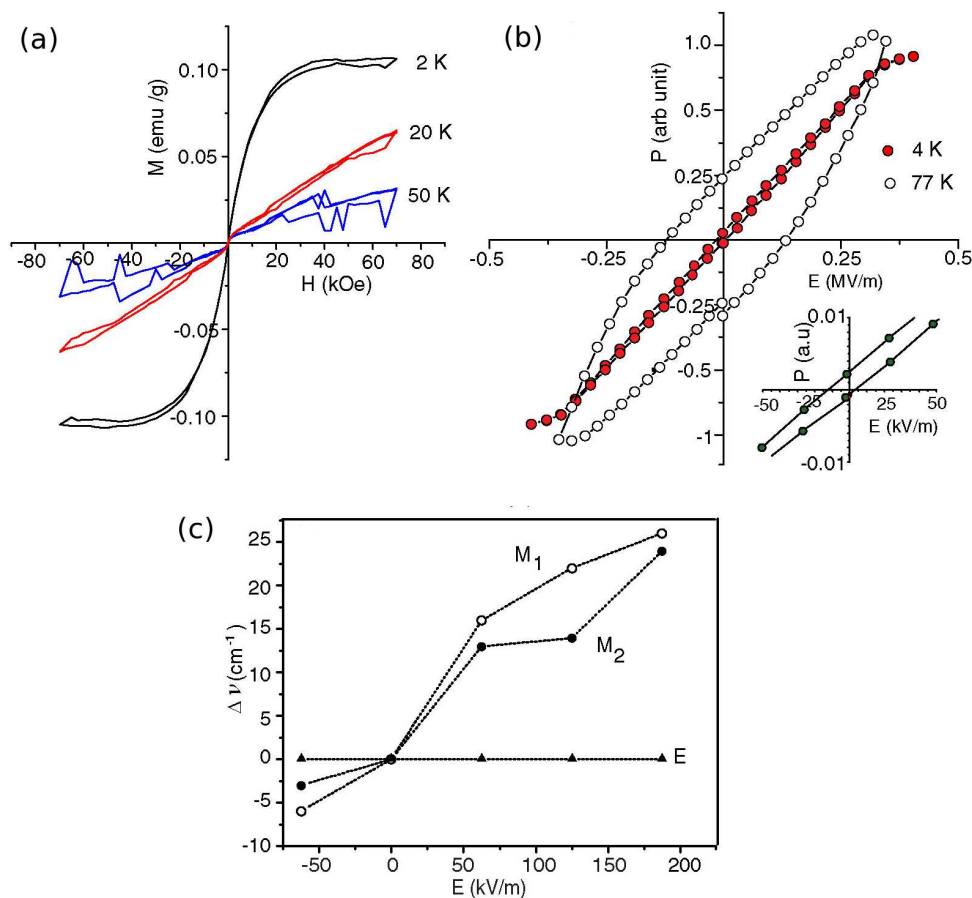


Figure 7.1: (a) Magnetic hysteresis curves for a bunch of parallel Se microrods at three temperatures spanning the magnetic ordering temperature. (b) Ferroelectric hysteresis curve for Se microrods at 4 K. (c) Shift in magnon mode frequencies (M_1 and M_2) with applied DC electric field, recorded at 4 K. The phonon mode at 232 cm^{-1} shows very little field dependence. This work has been done by Pal *et al.* [142]. Copyright (2013) by Nature Publishing Group.

3-D insulator with quasi-1-D structure, which exhibits quantized polarization (non-trivial topological invariant) and hence a surface charge. The spontaneous magnetic ordering of this surface charge gives rise to magnetoelectric coupling, hence making elemental selenium the simplest material to exhibit magnetoelectric coupling with a novel origin *i.e.* non-trivial electronic topology.

One of the earliest known elemental semiconductors and photoconductors, Se, has an unusual, quasi-one-D, chiral structure. However, it has attracted little attention as a potential multiferroic. The crystal structure of trigonal Se (space group $P3_121$) consists

of parallel, helical atomic chains with three atoms per unit cell. The atoms within a helix are covalently bonded, and the weakly coupled helical chains are arranged on a hexagonal lattice. With a $4s^2 p^4$ configuration, Se was so far believed to be an insulator with no magnetic ordering. However experiments carried out by Pal *et. al.* [142], found evidence for both magnetic and ferroelectric order in Se microtubes below ≈ 40 K (see Figure 7.1). Their experimental study suggests that the magnetic ordering occurs mainly at the crystal surface, and they clearly observe magnetoelectric coupling from the dependence of frequency of magnon modes on the applied electric field (see Figure 7.1c).

We use first-principles simulations to show that elemental Se is indeed multiferroic. This property of Se arises from its complex, chiral structure and a non-trivial electronic topology. In this chapter, we discuss (a) electronic structure and topology of Se, and (b) present a Landau like theory which describes the origin of magnetoelectric coupling. We thus give a theory of the possible origin of multiferroic behaviour in elemental selenium.

7.1.2 Computational Methods

See section 3.1.2 for details of the first-principles calculations. The spin-density dependent GGA to exchange-correlation function (Perdew, Burke and Ernzerhof [30]) and ultrasoft pseudopotentials [34] were used to represent the interaction between ionic cores and valence electrons. Spin polarized calculations were performed using the GGA+U method with $U=1$ eV and 5 eV. Electric polarization was determined using the Berry's phase approach [148]. Integrations over the Brillouin zone were sampled over $5 \times 5 \times 5$ and $6 \times 6 \times 1$ meshes of k-points for bulk and slab calculations, respectively. Some of the subtle results (e.g., Berry phase polarization) were reproduced with LDA [1], and HGH pseudopotentials [149] and energy cutoff of 70 Ry using ABINIT package [150, 151].

7.1.3 Electronic structure and topology of Se

From our first-principles calculations we estimate the structural parameters: $a = 4.47$ Å and $c = 5.04$ Å, within 3% of their reported values. We find an indirect band gap of 1.1eV, which is underestimated with respect to the experimental value by $\approx 41\%$ (a

known limitation of the DFT method). For bulk Se, our calculations with local spin or magnetic moments on Se sites initialized with ferromagnetic (FM) and antiferromagnetic (AFM) ordering resulted in a state with vanishing magnetic moments, confirming our experimental prediction [142] that bulk Se is non-magnetic.

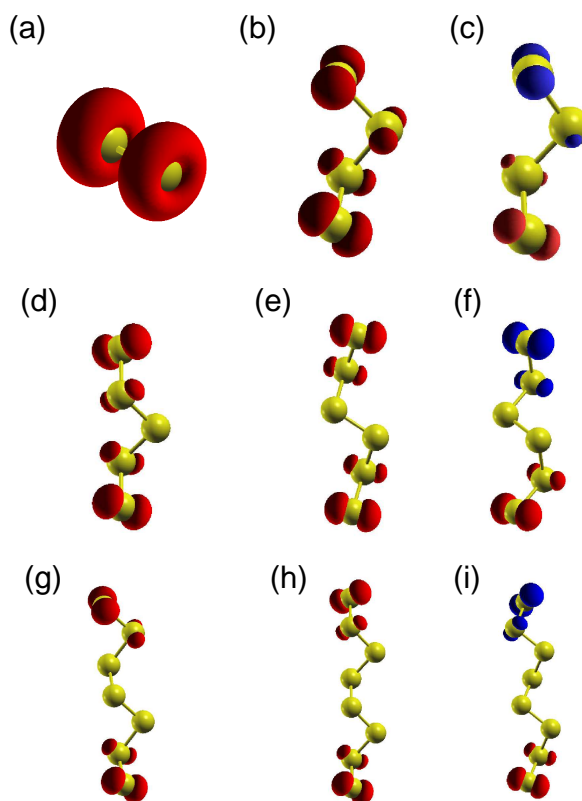


Figure 7.2: Isosurfaces of spin density of Se chains of different length with (a) FM ordering in 2 atom chain, (b) FM and (c) AFM ordering in 4 atom chain, (d) FM ordering in 5 atom chain, (e) FM and (f) AFM ordering in 6 atom chain, (g) FM ordering in 7 atom chain, (h) FM and (i) AFM ordering in 8 atom chain. In all the cases, it is evident that the magnetic moments are localized and confined to the end atoms of the chains. Copyright (2013) by Nature Publishing Group [142].

We next investigated the possible presence of magnetic moments in 2-8 atom, helical chains of Se, initialized with different types of magnetic order along the chains. For all except the 3-atom chains, the self-consistent electronic ground state clearly exhibits an ordering of magnetic moments, with the moments confined at the ends of the chains (see Figure 7.2). For odd-atom chains, the initial AFM state de-evolved into a FM state, while even-atom chains exhibit stable ordering of both AFM and FM types, with very similar

energies. Thus the observed magnetism can originate from the surface or boundary of Se.

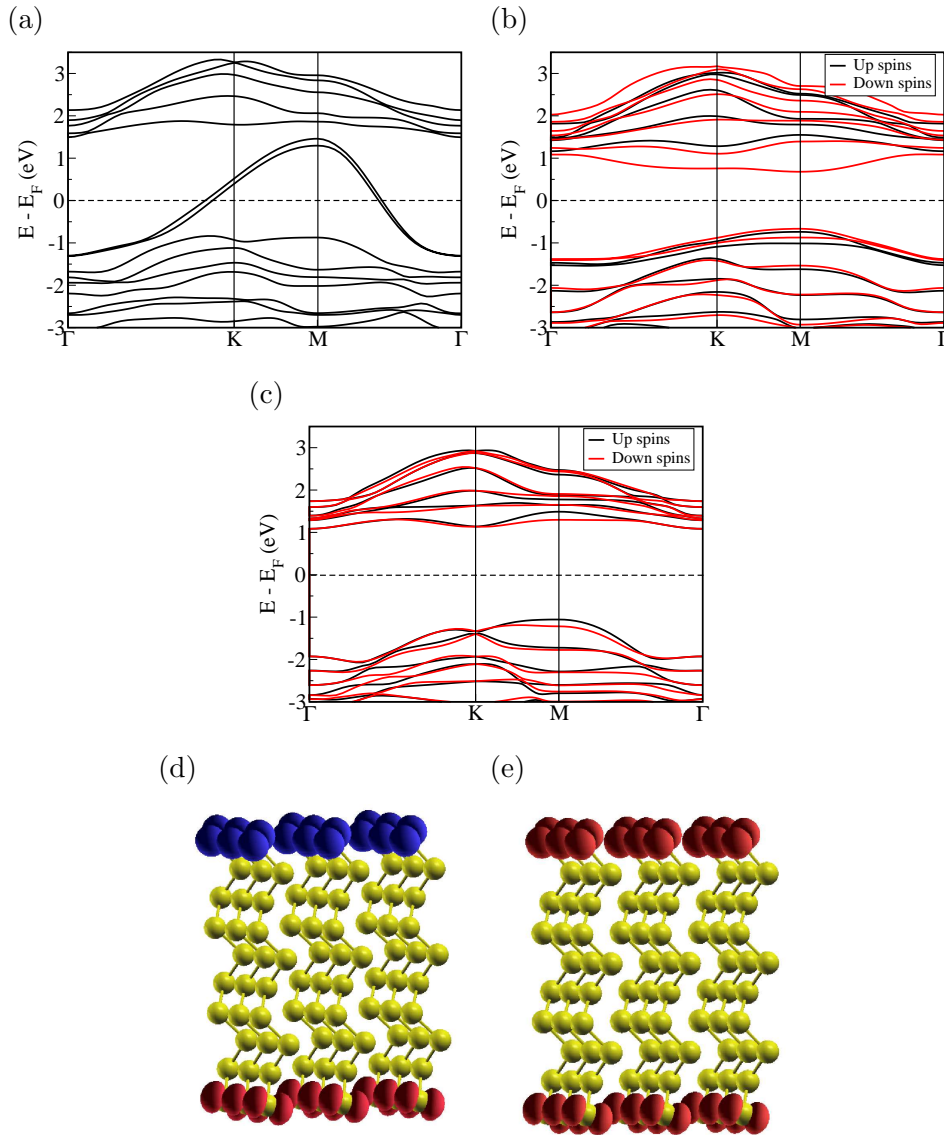


Figure 7.3: Electronic structure of Se (001) slab with 10 atomic planes in (a) a non-magnetic configuration with metallic nature due to surface states, (b) ferromagnetic configuration, and antiferromagnetic configuration obtained with $U = 5$ eV, exhibiting a band gap. Iso-surfaces of spin-density in (d) antiferromagnetic configuration and (e) ferromagnetic configuration, revealing the magnetic moments localized at the surface. Copyright (2013) by Nature Publishing Group [142].

To simulate the (001) surface, we have studied slabs consisting of 10 and 11 atomic planes separated from its periodic images by a vacuum of 1 nm along c-direction and initialized with AFM and FM ordering of spins at its surface. The non-magnetic state of

the slab exhibits a metallic electronic structure (see Figure 7.3a), and the bands crossing the Fermi energy are localized at the surfaces. As Se is quasi-one-dimensional, we expect this electronic structure to be unstable possibly with respect to magnetic ordering. Noting that magnetism in graphene nano-ribbons arising from its edge states is stabilized by on-site correlation [152], we simulated the Se slab by including on-site correlation with Hubbard $U = 1$ eV to 5 eV, and initial states with AFM and FM ordering. For all the Hubbard U values, magnetic moments and the nature of electronic structure (with band gap increasing with U) of the selenium slab remain qualitatively the same (see Figure 7.4). In contrast to bulk Se, the self-consistent solution exhibits non zero ($\approx 0.5 \mu_B/\text{atom}$) local magnetic moments on the surface atoms even after structural relaxation. The relaxed structures with AFM and FM configurations are energetically the same, implying only a weak interaction between the moments at the opposite slab surfaces as expected. A band gap opens up in the electronic structure upon magnetic ordering at the Se slab surfaces (see Figures 7.3b and 7.3c), and the visualization of the spin-density iso-surfaces (see Figures 7.3d and 7.3e) clearly shows that the surface states are responsible for the magnetic character of the slabs. An increase in the on-site correlation energy U results in further stabilization of the surface spins and their ordering.

The robustness of the surface states of the Se slab and their resemblance to the localized states at the end of single helical chains of Se prompt us to trace their origin to the electronic topology [153] of bulk Se. As Se has a quasi-one-dimensional structure, we note that the relevant topological invariant is essentially the Berry phase of occupied electronic states, which is essentially the polarization [154]. Symmetry considerations predict zero polarization in the ab plane as well as along the c -axis of bulk Se. Berry-phase calculations confirm the former expectation, but predict a half-integer quantum polarization, $P_z = e/A$ along z -axis ($e =$ electronic charge, $A =$ unit cell area). This does not violate symmetry principles, since polarization (as a Berry phase) can be estimated only within an integer quantum polarization. Thus, P and $-P$ (obtained by applying inversion symmetry or a two-fold rotation along an axis in the ab -plane in case of Se) may differ by an integer quantum polarization ($= eR/\Omega$); hence a half-integer quantum polarization is allowed by

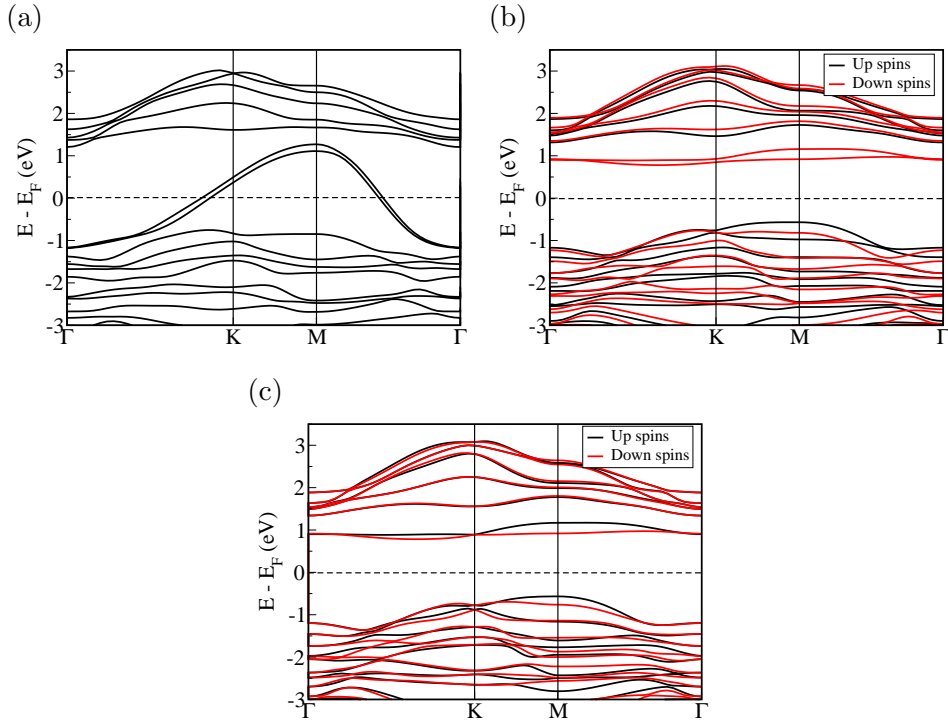


Figure 7.4: Electronic structure of Se (001) slab with 10 atomic planes in (a) a non-magnetic configuration with metallic nature due to surface states, and (b) ferromagnetic configuration, and (c) antiferromagnetic configuration obtained with $U = 3$ eV, exhibiting a bandgap. Copyright (2013) by Nature Publishing Group [142].

symmetry even in centrosymmetric systems. We believe bulk Se is the only system known so far to exhibit a half-integer quantum *electronic* polarization (*i.e.* the electronic structure of bulk Se has an overall Berry phase of π) and its total (ionic + electronic) polarization remains invariant upon any shift in the origin. This would naturally support electronic charge at the surfaces and consequently the magnetism. Ordering of spins at the surface breaks the two-fold symmetry (C_{2x}) of Se (see Figure 7.3d) and gives rise to a switchable polarization. This necessarily implies that the ferroelectric and magnetic ordering temperatures are close or identical, in conformity with experimental observations [142]. Such magnetically induced polarization, though small, inherently involves a strong magnetoelectric coupling. The emergence of multiferroic behaviour in selenium microtubes/slab can be best understood from the flow of ideas shown in Figure 7.5.

We point out that Se is a weak topological insulator (TI), being a 2-D array of 1-D insulators with nontrivial topological invariant. This is reflected in an even number of

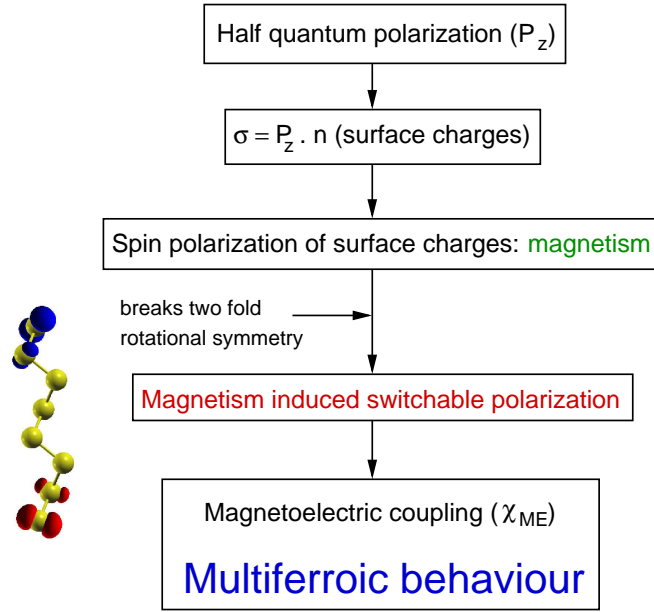


Figure 7.5: Flowchart depicting the emergence of multiferroic behaviour in Se microtubes from half quantum of polarization.

band crossings at the Fermi energy (see Figures 7.3 and 7.4) in the electronic structure of the non-magnetic state. As a result, its surface states are not as robust against disorder as those of a strong 3-D TI. Finally, as the topological invariant of bulk Se is linked to its structure and forced by its symmetry, it should be considered a crystalline TI.

7.1.4 Origin of the magnetoelectric effect: spin-charge-phonon coupling

It is observed that the Raman active E phonon mode at 232 cm^{-1} in trigonal Se shows no dependence on external electric field. On the other hand, the magnon modes that appear in the Raman spectrum below 40 K are depend strongly on the external electric field. We now present an analysis of the phonons and their coupling with spin and electric field to explain the experimental observations (see Figure 7.1c). Our theoretical estimates of the phonon frequencies of bulk Se (217 cm^{-1} for the E mode and 89 cm^{-1} for an IR-active A_2 mode) are in reasonable agreement with experimental observations (232 cm^{-1} and 82 cm^{-1} , respectively [142]). The Hellman-Feynman forces on Se atoms in the non-magnetic state with atomic structure obtained by minimizing energy of the ferromagnetic state give the lowest order spin-phonon coupling. Projecting these onto the phonon eigenvectors,

we establish that the Raman-active E mode at 217 cm^{-1} exhibits the largest spin-phonon coupling, while the lower energy E mode at 128 cm^{-1} shows noticeable but weaker coupling with spin. This spin-phonon coupling is responsible for the concurrent anomalies in magnon and phonon modes seen in the Raman spectra near the magnetic ordering temperature. Though the three Se atoms in the trigonal crystal cell are symmetry equivalent and homopolar, an external electric field does couple to its lattice (phonons) due its non-trivial symmetry (see Table 7.1). The tensorial character of the coupling of electric field with the atomic displacements (Born dynamical charges) permits a nonzero dynamical charge Z for Se atoms positioned on the x-axis, with the electric field also along x-axis, e.g., $Z_{xx} = 0.70$.

Having established the coupling of phonons with spin and electric field based on experimental and first-principles theoretical evidence, we express free energy of Se surface as a function of spin (S), phonon coordinate (u) and electric field (E), using a Landau-like theory:

$$F = \frac{1}{2}Ku^2 - ZEu - LSu + JS^2, \quad (7.1)$$

where $K = \mu\omega^2$ is the phonon spring constant, Z is the dynamical charge, L is the spin-phonon coupling and J , the exchange coupling. Minimizing energy with respect to u , we obtain the effective free energy:

$$F_{eff} = -\frac{Z^2}{2K}E^2 + \left(J - \frac{L^2}{2K}\right)S^2 - \frac{ZL}{K}ES, \quad (7.2)$$

where the three terms on RHS are the phonon contribution to the dielectric constant, the phonon-renormalized exchange coupling and the phonon-mediated linear magnetoelectric coupling respectively. We note that magnon frequency is determined by the effective exchange coupling.

Since this *linear* theory does not explain the electric field dependence of magnon frequency (a third order effect), we consider the third order coupling of a phonon with the electric field: $H = \alpha u^2 E$, with $\alpha = -\frac{\partial Z}{2\partial u}$. We determine α by distorting the structure

Table 7.1: (Top) The mode effective charges (Z^m) of Raman active E mode of bulk Se with an undistorted structure. (Centre, Bottom) Changes in the mode effective charges ($Z_{distorted}^m - Z_{undistorted}^m$) of a distorted structure obtained by freezing in the atomic displacements of the relevant Raman active E modes. Copyright (2013) by Nature Publishing Group [142].

Mode effective charges of the undistorted structure			
Mode frequency (cm^{-1})	x	y	z
128	0.142	1.293	0.000
128	1.293	-0.142	0.000
217	0.016	-0.117	0.000
217	0.117	0.016	0.000
Change in mode effective charges on freezing E mode at 128 cm^{-1}			
	x	y	z
128	-0.090	0.004	0.017
128	0.028	-0.093	-0.006
Change in mode effective charges on freezing E mode at 217 cm^{-1}			
	x	y	z
217	0.027	0.018	-0.046
217	-0.017	-0.031	0.021

with the atomic displacements (u) by $\approx 1\%$ of the lattice constant and estimating the Born dynamical charges of phonons using DFT linear response. Interestingly, lower energy modes exhibit the strongest third order coupling with electric field, while α of the Raman-active E mode is relatively much weaker (see Table 7.1). This explains the observed independence of the E mode (at 217 cm^{-1}) on electric field. The exchange coupling

renormalized by lower energy modes, can be shown to change with electric field as:

$$\frac{L^2}{2K} \left(1 - 2 \frac{\alpha E}{K} \right).$$

In this model, the observed dependence of magnon frequency on electric field originates from the third order phonon–electric field and linear spin-phonon couplings.

7.1.5 Conclusions

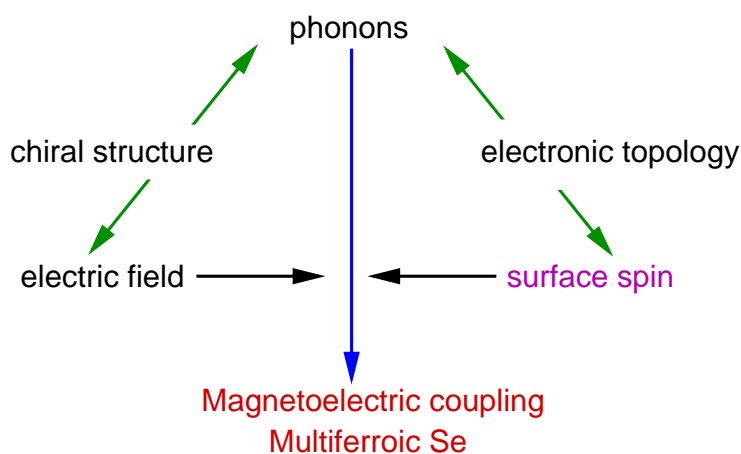


Figure 7.6: Schematic of emergence of magnetolectric coupling in Se microtubes. Note that the emergence of magnetolectric coupling requires the presence of surface spin.

The emergence of multiferroic behaviour in a non-magnetic, elemental semiconductor is quite astonishing. Indeed, ferroelectricity and magnetism are neither expected, nor observed in bulk Se. Our work suggests that the chiral arrangement of Se atoms leads to a coupling between the lattice and electric field, while the spin-polarized surface arises from its unique electronic structure with non-trivial topology, reflected in the Berry phase of π . This highly unusual coupling of its lattice with the electric field, surface spins or magnetic excitations allows elemental Se to acquire multiferroic properties, observable only in low-dimensional samples (see Figure 7.6). Significantly, our work uncovers a new route to multiferroic behaviour that is not strongly restricted by symmetry, and indicates that similar magnetolectric surface properties could well emerge in other semiconductors with low-symmetry chiral space group. At the same time, our observations provide strong

support to the recent experimental investigations that have shown multiferroicity in Se microtubes.

7.2 Optical Rotation in Selenium

7.2.1 Introduction

Trigonal bulk Selenium is an anisotropic and strongly covalent crystal with three atoms per unit cell. It consists of hexagonally stacked helical chains with their axis parallel to the c -axis of the crystal. The strong covalent bonding between atoms of the same chain, and weak inter-chain interaction gives rise to its crystal anisotropy. This non-trivial structure of trigonal bulk selenium is responsible for its interesting vibrational and optical properties.

Unlike cubic silicon, germanium or carbon, selenium exhibits infrared active phonons due to its non-trivial chiral structure and the presence of more than 2 atoms in its unit cell [155]. From the symmetry analysis, there exist three infrared (IR) active phonon modes, two of which are degenerate (E symmetry optical modes) and couple with electric field in the ‘ x ’ and ‘ y ’ directions, and the third one (A_2 symmetry optical mode) couples to the electric field along ‘ z ’ direction. Although the system is homopolar, it exhibits IR active phonons due to its chirality, evident in non-zero Born effective charges [155]. Using first-principles theoretical analysis we show that selenium optically rotates the plane of polarization of light propagating in directions perpendicular to the chains. This optical rotatory ability of selenium can be traced to magnetoelectric coupling which arises from the coupling of electric field to phonons (even in the absence of surface spins). Similar property was predicted by Lombardi *et. al.* [156] for chiral molecules.

7.2.2 Computational Methods

We based our theoretical analysis on first-principles within density functional theory (DFT) with a Generalized Gradient Approximation (GGA) and Perdew Burke and Ernzerhof [30] functional for exchange correlation energy as implemented in the ABINIT [150,151]

code. An energy cutoff of 70 Ry was used in truncating the plane wave basis in representation of Kohn-Sham wavefunctions. The Brillouin zone integrations were sampled over a 9x9x9 mesh of k-points. The phonons at the zone center and Born effective charges of bulk trigonal selenium, were determined using DFT linear response as implemented in the ABINIT package [150, 151].

Table 7.2: Born effective charges on all the three Se atoms.

Atom number	Direction of displacement	Direction of electric field		
		x	y	z
1	x	0.70	0.00	0.00
	y	0.00	-0.70	-0.74
	z	0.00	-0.38	0.00
2	x	-0.35	-0.61	0.64
	y	-0.61	0.35	0.37
	z	0.33	0.19	0.00
3	x	-0.35	0.61	-0.64
	y	0.61	0.35	0.37
	z	-0.33	0.19	0.00

7.2.3 Relation between Z^* and χ

Even though all the Se-Se bonds in selenium are covalent and all the positions symmetry equivalent, external electric field couples to lattice vibrations due to its non-trivial chiral structure. We consider Se structure with its axis of the helical chains parallel to ‘z’ direction *i.e.* the c-axis of the crystal. The maximum magnitude of Born effective charge (Z^*) is 0.74 |e| (refer to Table 7.2). Lattice vibrations at 89 cm^{-1} (ω_z) and two degenerate modes at 128 cm^{-1} (ω_x and ω_y) couple to electric field (E) in ‘z’, ‘x’ and ‘y’ directions respectively (see Figure 7.7). In the presence of an external electric field, the atoms are displaced according to the eigen displacements of the respective phonon mode, and

electric dipole moments induced on the Se atoms also point in the same direction as their displacements (refer to Table 7.2 and Figure 7.7).

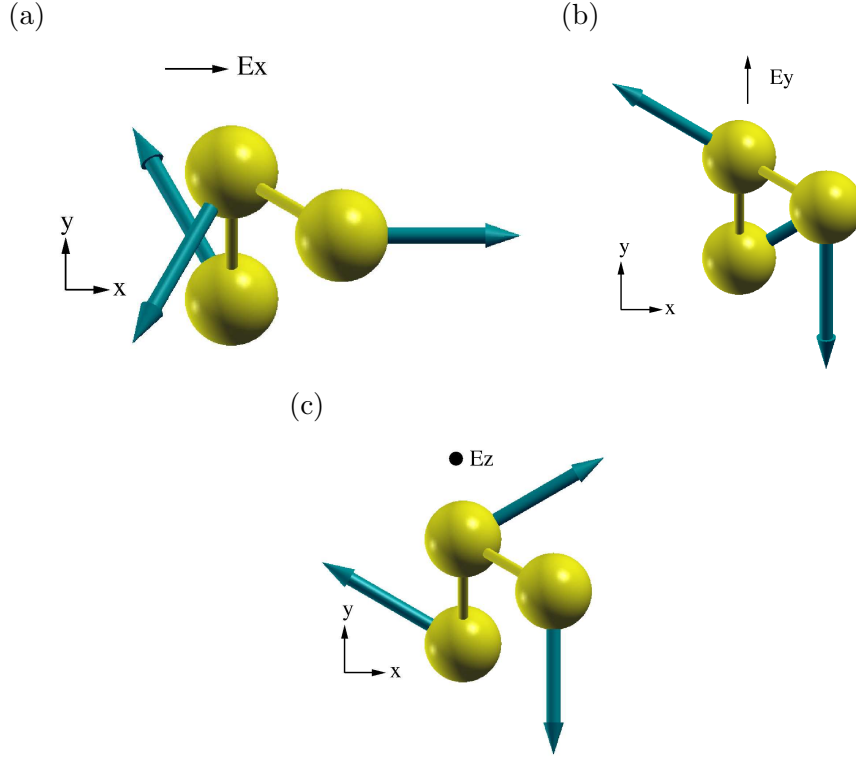


Figure 7.7: Bulk phonon modes of selenium that couple with electric field applied along (a) ‘x’, (b) ‘y’ and (c) ‘z’ directions. Phonon modes that couple to electric fields along ‘x’ and ‘y’ directions are degenerate and are at 128 cm^{-1} . The phonon mode at 89 cm^{-1} couples to electric field along ‘z’ direction, and involves rotation of Se helical chain about its axis.

We first derive the relation between magnetoelectric coupling (χ) in chiral media and optical rotation as a consequence of coupling of the lattice with external electric field (*i.e.* non-zero Z^*). Let \mathbf{E} be the electric field of the electromagnetic wave. We assume that the direction of propagation is in the ‘xy’ plane, and hence electric field can be expressed as $\mathbf{E} = E_o e^{i(\omega t - \mathbf{k} \cdot \mathbf{r})} (\sin\theta \cos\phi \hat{x} + \sin\theta \sin\phi \hat{y} + \cos\theta \hat{z})$, where θ and ϕ are polar and azimuthal angles in the spherical co-ordinate system. \mathbf{k} is the propagation vector in the ‘xy’ plane (*i.e.* $\mathbf{k} = k_x \hat{x} + k_y \hat{y}$). From the orthogonality condition of \mathbf{k} and \mathbf{E} for electromagnetic waves we arrive at the relation, $\phi = \tan^{-1}(k_x/k_y)$.

From the Born effective charges of Se atoms, we estimate the electric dipole moments

of atoms as follows,

$$p_{i,\alpha} = \sum_{\beta} Z_{i,\alpha\beta}^* u_{i,\beta}, \quad (7.3)$$

where α and β are cartesian directions, (x, y, z) . $Z_{i,\alpha\beta}^*$ is the Born effective charge tensor of the i^{th} atom, and $u_{i,\beta}$ the displacement of the i^{th} atom in the β direction. Expressing the displacement $u_{i\beta}$ in terms of Born effective charges and electric field we get,

$$u_{i,\beta} = \sum_{\gamma} \frac{Z_{i,\gamma\beta}^* E_{\gamma}}{\mu_{\gamma}(\omega_{\gamma}^2 - \omega^2)}, \quad (7.4)$$

where ω_{γ} and μ_{γ} are the frequency and the reduced mass of the IR active phonon mode that couples to electric field in γ direction. ω is the frequency of incident light. Hence, the electric dipole moment expression can be written as,

$$p_{i,\alpha} = \sum_{\beta,\gamma} Z_{i,\alpha\beta}^* Z_{i,\gamma\beta}^* \frac{E_{\gamma}}{\mu_{\gamma}(\omega_{\gamma}^2 - \omega^2)}. \quad (7.5)$$

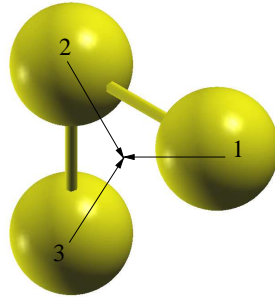


Figure 7.8: Arrows indicate the position vectors of Se atoms with respect to the centre of the helix.

Let \mathbf{r}_1 , \mathbf{r}_2 and \mathbf{r}_3 be the in-plane position vectors of the three Se atoms with respect

to the central axis of the helix (see Figure 7.8), and R the radius of the helix.

$$\begin{aligned}
 \mathbf{r}_1 &= -R \hat{x}, \\
 \mathbf{r}_2 &= -R \left(-\frac{1}{2} \hat{x} + \frac{\sqrt{3}}{2} \hat{y} \right), \\
 \mathbf{r}_3 &= -R \left(-\frac{1}{2} \hat{x} - \frac{\sqrt{3}}{2} \hat{y} \right).
 \end{aligned} \tag{7.6}$$

We estimate the magnetic field ' \mathbf{B}_i ' magnetic field induced by the motion of each atom 'i' using the Biot-Savart law as follows,

$$\begin{aligned}
 \mathbf{B} &= \sum_i \mathbf{B}_i \\
 &= \sum_i \frac{\mu_o}{4\pi} \frac{q[\mathbf{v}_i \times \mathbf{r}_i]}{r_i^3}, \\
 &= \sum_i \frac{\mu_o}{4\pi} \frac{\left[\frac{d\mathbf{p}_i}{dt} \times \mathbf{r}_i \right]}{r_i^3}, \\
 &= \sum_i \frac{\mu_o}{4\pi} \frac{[i\omega \mathbf{p}_i \times \mathbf{r}_i]}{r_i^3}, \text{ from } \mathbf{E} = \mathbf{E}_o e^{i(\omega t - \mathbf{k} \cdot \mathbf{r})} \text{ and equation 7.5.}
 \end{aligned} \tag{7.7}$$

The system is mono-atomic and the magnitude of forces acting on all the atoms are the same (see Figure 7.7). Hence, the magnitude of electric dipole moment on each atom under the influence of an electric field in a particular direction (E_α) is the same, *i.e.* $|\mathbf{p}_i| = p$ for a given α direction.

To simplify the derivation (of the relation between Z^* and χ), we consider the effect of electric field in 'x', 'y' and 'z' directions independently and estimate the magnetic field (\mathbf{B}) induced at the centre of the helix (selenium molecule of three atoms in the bulk chiral structure) by the electric field.

- (1) For $E_x \neq 0$ and $E_y = E_z = 0$ (i.e. $\theta = 90^\circ$ and $\phi = 0^\circ$), we get atom by atom contribution to magnetic field.

$$\begin{aligned}\mathbf{B}_1 &= \frac{\mu_o}{4\pi} \frac{[i\omega\mathbf{p}_1 \times \mathbf{r}_1]}{r_1^3}, \\ &= \frac{\mu_o}{4\pi} \frac{i\omega p_1 R[\hat{x} \times -\hat{x}]}{R^3}, \\ &= 0.\end{aligned}$$

$$\begin{aligned}\mathbf{B}_2 &= \frac{\mu_o}{4\pi} \frac{[i\omega\mathbf{p}_2 \times \mathbf{r}_2]}{r_2^3}, \\ &= \frac{\mu_o}{4\pi} \frac{i\omega p_2 R[(-\frac{1}{2}\hat{x} - \frac{\sqrt{3}}{2}\hat{y}) \times -(-\frac{1}{2}\hat{x} + \frac{\sqrt{3}}{2}\hat{y})]}{R^3}, \\ &= \frac{\mu_o}{4\pi} \frac{i\omega \frac{\sqrt{3}}{2} p}{R^2} \hat{z}.\end{aligned}\tag{7.8}$$

$$\begin{aligned}\mathbf{B}_3 &= \frac{\mu_o}{4\pi} \frac{[i\omega\mathbf{p}_3 \times \mathbf{r}_3]}{r_3^3}, \\ &= \frac{\mu_o}{4\pi} \frac{i\omega p_3 R[(-\frac{1}{2}\hat{x} + \frac{\sqrt{3}}{2}\hat{y}) \times -(-\frac{1}{2}\hat{x} - \frac{\sqrt{3}}{2}\hat{y})]}{R^3}, \\ &= \frac{\mu_o}{4\pi} \frac{-i\omega \frac{\sqrt{3}}{2} p}{R^2} \hat{z}.\end{aligned}$$

$$\Rightarrow \mathbf{B} = \mathbf{B}_1 + \mathbf{B}_2 + \mathbf{B}_3 = 0$$

(2) For $E_y \neq 0$ and $E_x = E_z = 0$ (i.e. $\theta = 90^\circ$ and $\phi = 90^\circ$)

$$\begin{aligned}\mathbf{B}_1 &= \frac{\mu_o}{4\pi} \frac{[i\omega \mathbf{p}_1 \times \mathbf{r}_1]}{r_1^3}, \\ &= \frac{\mu_o}{4\pi} \frac{i\omega p_1 R[-\hat{y} \times -\hat{x}]}{R^3}, \\ &= \frac{\mu_o}{4\pi} \frac{-i\omega p}{R^2} \hat{z}.\end{aligned}$$

$$\begin{aligned}\mathbf{B}_2 &= \frac{\mu_o}{4\pi} \frac{[i\omega \mathbf{p}_2 \times \mathbf{r}_2]}{r_2^3}, \\ &= \frac{\mu_o}{4\pi} \frac{i\omega p_2 R[(-\frac{\sqrt{3}}{2}\hat{x} + \frac{1}{2}\hat{y}) \times -(-\frac{1}{2}\hat{x} + \frac{\sqrt{3}}{2}\hat{y})]}{R^3}, \\ &= \frac{\mu_o}{4\pi} \frac{i\omega \frac{1}{2}p}{R^2} \hat{z}.\end{aligned}\tag{7.9}$$

$$\begin{aligned}\mathbf{B}_3 &= \frac{\mu_o}{4\pi} \frac{[i\omega \mathbf{p}_3 \times \mathbf{r}_3]}{r_3^3}, \\ &= \frac{\mu_o}{4\pi} \frac{i\omega p_3 R[(\frac{\sqrt{3}}{2}\hat{x} + \frac{1}{2}\hat{y}) \times -(-\frac{1}{2}\hat{x} - \frac{\sqrt{3}}{2}\hat{y})]}{R^3}, \\ &= \frac{\mu_o}{4\pi} \frac{i\omega \frac{1}{2}p}{R^2} \hat{z}.\end{aligned}$$

$$\Rightarrow \mathbf{B} = \mathbf{B}_1 + \mathbf{B}_2 + \mathbf{B}_3 = 0$$

(3) For $E_z \neq 0$ and $E_x = E_y = 0$ (i.e. $\theta = 0^\circ$ and $\phi = 0^\circ$)

$$\begin{aligned}
 \mathbf{B}_1 &= \frac{\mu_o}{4\pi} \frac{[i\omega\mathbf{p}_1 \times \mathbf{r}_1]}{r_1^3}, \\
 &= \frac{\mu_o}{4\pi} \frac{i\omega p_1 R[-\hat{y} \times -\hat{x}]}{R^3}, \\
 &= \frac{\mu_o}{4\pi} \frac{-i\omega p}{R^2} \hat{z}. \\
 \\
 \mathbf{B}_2 &= \frac{\mu_o}{4\pi} \frac{[i\omega\mathbf{p}_2 \times \mathbf{r}_2]}{r_2^3}, \\
 &= \frac{\mu_o}{4\pi} \frac{i\omega p_2 R[(\frac{\sqrt{3}}{2}\hat{x} + \frac{1}{2}\hat{y}) \times -(-\frac{1}{2}\hat{x} + \frac{\sqrt{3}}{2}\hat{y})]}{R^3}, \\
 &= \frac{\mu_o}{4\pi} \frac{-i\omega p}{R^2} \hat{z}.
 \end{aligned} \tag{7.10}$$

$$\begin{aligned}
 \mathbf{B}_3 &= \frac{\mu_o}{4\pi} \frac{[i\omega\mathbf{p}_3 \times \mathbf{r}_3]}{r_3^3}, \\
 &= \frac{\mu_o}{4\pi} \frac{i\omega p_3 R[(\frac{-\sqrt{3}}{2}\hat{x} + \frac{1}{2}\hat{y}) \times -(-\frac{1}{2}\hat{x} - \frac{\sqrt{3}}{2}\hat{y})]}{R^3}, \\
 &= \frac{\mu_o}{4\pi} \frac{-i\omega p}{R^2} \hat{z}.
 \end{aligned}$$

$$\Rightarrow \mathbf{B} = \mathbf{B}_1 + \mathbf{B}_2 + \mathbf{B}_3,$$

$$\mathbf{B} = -i \frac{\mu_o}{4\pi} \frac{3\omega p}{R^2} \hat{z},$$

Hence, only the electric field component along 'z' direction gives rise to non-zero magnetic field (also along z). Having established this, we now proceed to calculating the magnetic field induced by electric field in 'z' direction in bulk selenium.

Since trigonal bulk selenium is composed of parallel helical chains, we can approximate a helical chain of Se atoms to a solenoid. Hence, the magnetic field induced by the electric

field along the helical axis (*i.e.* the ‘z’ direction) is given by,

$$\begin{aligned}
 \mathbf{B} &= \mu_o n \mathbf{I}, \\
 &= \mu_o \frac{3}{c} \frac{d\mathbf{p}/dt}{2\pi R}, \\
 &= \mu_o \frac{3}{c} \frac{i\omega\mathbf{p}}{2\pi R}, \\
 &= -i \frac{\mu_o 6\omega p}{4\pi Rc} \hat{z}, \\
 \mathbf{B} &= 2 \left| \mathbf{B}_1 + \mathbf{B}_2 + \mathbf{B}_3 \right| \frac{R}{c}, \text{ from equation 7.10.}
 \end{aligned} \tag{7.11}$$

Here, \mathbf{I} is the current flowing through the solenoid, and n is the number of turns per unit length, and c is the lattice constant along the direction of helical axis. The negative sign of \mathbf{B} is due to current \mathbf{I} flowing in ‘-z’ direction. The magnetoelectric coupling (χ) can be defined as

$$\begin{aligned}
 \chi &= -i \frac{\partial \mathbf{B}}{\partial \mathbf{E}}, \text{ from the Tellegen form of constitutive relationships [157],} \\
 &= -i \frac{\partial B_z}{\partial E_z}, \\
 \chi &= -\frac{\mu_o 6\omega}{4\pi Rc} \frac{\partial p}{\partial E_z},
 \end{aligned} \tag{7.12}$$

where p is the magnitude of electric dipole moment of any one of the Se atoms, when electric field is applied in ‘z’ direction (same as the arrows in Figure 7.7c), and ‘-ve’ sign indicates that the induced magnetic field is in a direction opposite to the applied electric field. On substituting equation 7.5 in equation 7.12 for atom 1 (refer to Table 7.2) we get,

$$\chi = -\frac{\mu_o 6\omega}{4\pi Rc} \frac{Z_{1,y,y}^* Z_{1,z,y}^*}{\mu_z(\omega_z^2 - \omega^2)}. \tag{7.13}$$

7.2.4 Polarization rotation

In chiral media, the Tellegen form of constitutive relationships is very convenient for single frequency electromagnetic waves [157].

$$\begin{aligned}\mathbf{D} &= \epsilon\mathbf{E} - i\chi\mathbf{H}, \\ \mathbf{B} &= \mu\mathbf{H} + i\chi\mathbf{E},\end{aligned}\tag{7.14}$$

here χ is defined as a parameter that describes the chiral properties of the medium. It is clear that $\chi = -i \partial\mathbf{B}/\partial\mathbf{E}$, and is same as the magnetoelectric coupling constant in equation 7.12. In the case of trigonal bulk selenium, only the phonon mode at 89 cm^{-1} *i.e.* the mode coupling with \mathbf{E}_z field induces a non-zero magnetic field (refer to equation 7.10). For any arbitrary direction of applied electric field, only the ‘z’ component of \mathbf{E} gives rise to non-zero magnetic field, and therefore non-zero magnetoelectric coupling. The magnetic field induced by the rotatory motion of the helix (see Figure 7.7c) is along the ‘z’ direction (\mathbf{B}_z), and perpendicular to the incident magnetic field ($\mathbf{B}_{xy} = \mathbf{B}_x + \mathbf{B}_y$). The resultant magnetic field ($\tilde{\mathbf{B}}$) is the sum of \mathbf{B}_{xy} and \mathbf{B}_z , which implies that the direction of polarization of magnetic field rotates as the IR radiation passes through the crystal. Along with $\tilde{\mathbf{B}}$, the electric field of incident electromagnetic wave also rotates (since \mathbf{E} and $\tilde{\mathbf{B}}$ are perpendicular in electromagnetic radiation), and hence selenium exhibits polarization rotation. The extent of this rotation is given by [157],

$$\begin{aligned}\phi &= \chi\omega l, \\ \frac{\phi}{l} &= \chi\omega \\ &= \frac{\mu_o}{4\pi} \frac{6\omega^2}{Rc} \frac{Z_{1,y,y}^* Z_{1,z,y}^*}{\mu_z(\omega_z^2 - \omega^2)}, \text{ from equation 7.13 (within the -ve sign),}\end{aligned}\tag{7.15}$$

where ϕ is the angle of rotation, χ is the magnetoelectric coupling, ω is the frequency of the incident radiation, and l is the distance traversed by electromagnetic radiation in the crystal. Figure 7.9 shows the variation of ϕ/l with varying frequency of incident electromagnetic radiation ($\omega = 0.1$ to 6 THz). We have substituted $R = 1 \text{ \AA}$, $c = 4.95 \text{ \AA}$, $Z^* = 0.74e \text{ C}$, $\omega_z = 89 \text{ cm}^{-1} = 2.67 \text{ THz}$. Since trigonal bulk selenium is mono-atomic, the

reduced mass of a phonon mode is same as the mass of a single atom [158] *i.e.* $\mu_z = \text{mass of Se} = 78.96 \times 1.67 \times 10^{-27} \text{ kg}$. The angle of rotation diverges as ω approaches ω_z , and $\phi/l \approx -3.3^\circ/\text{mm}$ at $\omega = 2.7 \text{ THz}$. In the limit $\omega \rightarrow 0$, *i.e.* the polarization rotation vanishes in the low frequency limit. But in the high frequency limit *i.e.* $\omega \rightarrow \infty$, $\phi/l \rightarrow -0.08^\circ/\text{mm}$, implying a constant optical response of trigonal bulk selenium in the high frequency limit. The intrinsic absorption of selenium occurs at 375 THz with rotation as much as $300^\circ/\text{mm}$ [159], and at 88 THz with rotation of $4.8^\circ/\text{mm}$ [160]. It is important to note that these responses are at much higher frequencies and are due to electronic excitations [161], as compared to the mechanism we predict, which is due to IR active phonons in the far infrared region. This is essentially the Vibrational Circular Birefringence (VCB) [156] in trigonal bulk selenium using first-principles calculations and simple electromagnetic theory.

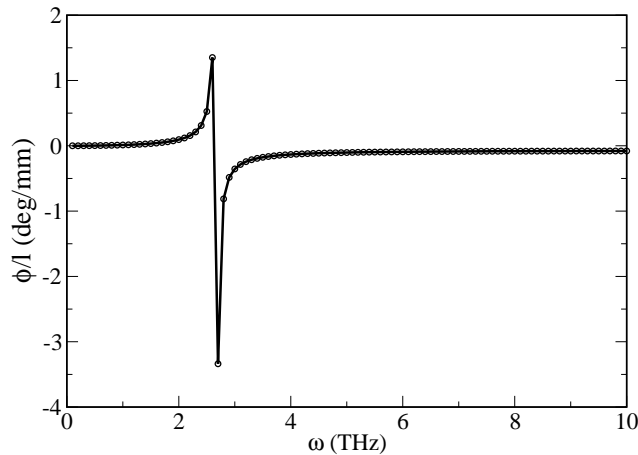


Figure 7.9: Variation in the angle of rotation (per unit length) *i.e.* ϕ/l with frequency of incident electromagnetic radiation. The electric field of the incident radiation is along the axis of the Se helical chain.

7.2.5 Conclusions

We propose a theory in which polarization rotation in the far infrared region of the electromagnetic spectrum originates from IR active phonons of trigonal bulk selenium. The IR active phonon at 89 cm^{-1} couples to the electric field along the helical axis, and gives rise to non-zero AC magnetoelectric coupling. This coupling leads to rotation of polarization

of electromagnetic waves, and explains the optical activity of trigonal bulk selenium in far IR region. We have shown that the AC magnetoelectric coupling arises from its chiral structure (which gives rise to IR active phonons), and not due to surface spins which are necessary to explain the emergence of DC magnetoelectric coupling in Se microtubes/slabs. Our observations can be summarized in the flowchart shown in Figure 7.10.

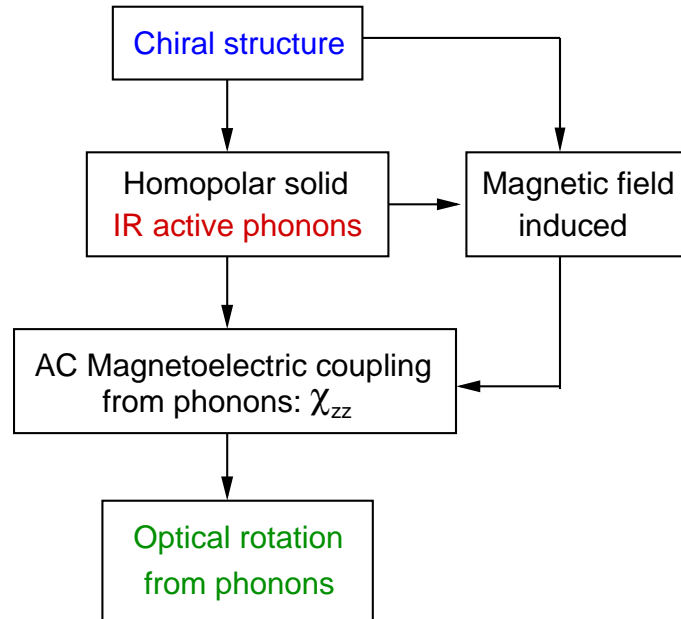


Figure 7.10: Flowchart depicting the emergence of magnetoelectric coupling and polarization rotation in trigonal bulk Se. Note that, the magnetoelectric coupling arises purely due the chiral structure of bulk Se, and does not involve surface spins.

Chapter 8

Summary

The central theme of this dissertation has been to elucidate the role played by defects in the modification of physical properties and behaviour of two dimensional as well as bulk materials. The compounds studied in this thesis are not only technologically important, but are also fundamentally interesting as they exhibit unusual phenomena involving fascinating physics. We have employed a combination of first-principles density theoretical calculations, modeling and phenomenological (eg. Landau) theory in our analysis to achieve this task.

We show that Stone-Wales (SW) defects in graphene and at the interface of a solid solution of graphene-boron nitride (C-BN) have comparable energies of formation, implying that SW defects are also very likely to form at C-BN interfaces (in contrast to their absence in hexagonal boron nitride). The coupling between electronic degrees of freedom, and the structural deformation associated with an SW defect leads to a shift in the Dirac cone from K to $K+\delta k$ in graphene. Whereas, the localization of Highest Occupied Molecular Orbital and Lowest Unoccupied Molecular Orbital at the SW defect, leads to an increased adsorption of CH_4 and CO_2 gases at the C-BN interface.

We have also studied stacking faults and their effects on polytypism in silver. In this work, we provided a possible explanation for the existence and stability of experimentally synthesized metastable 2H (with an unusually large c -constant) and 4H polytypes of silver. Our work shows that nesting of the Fermi surface, and unstable vibrational modes of the

2H polytype are responsible for its rather flat energy surface. This feature of the energy surface makes a large contribution to configurational entropy, and is likely to be a possible cause for metastability of the observed 2H polytype (with an unusual c -constant). On the other hand, it is observed in experiments that the 4H polytype makes a transition to 3C at 433 K. Though the exact mechanism of this phase transition is still unclear, our analysis has shown that stacking faults in the 4H polytype do not drive the phase transition, and other mechanisms such as local structural fluctuations and associated negative pressures should be explored to explain it.

We have shown that anti-site defects in $(\text{Al,Ga})\text{FeO}_3$ compounds give rise to unequal magnetic moments on the Fe ions, leading to the breaking of the in-plane inversion symmetry of the structure. This gives rise to a finite in-plane spontaneous polarization (which is switchable by external electric field) due to a strong spin-phonon coupling in these compounds. Thus, we provide a new mechanism for the emergence of multiferroic behaviour in $(\text{Al,Ga})\text{FeO}_3$, which is solely dependent on the presence of anti-site defects.

Our work on the 1T-polytype of MoS_2 highlights the strong coupling between its electronic and structural degrees of freedom. The 1T polytype of MoS_2 corresponds to a stacking fault (slip in one of the S atom planes) in its ground state (2H) structure. Nesting of the Fermi surface of 1T- MoS_2 , and the instability in its vibrational spectra lead to a structural phase transition that gives rise to improper ferroelectric behaviour in the faulted structure. Hence, our work shows that a strong coupling between electrons and phonons gives rise to an unexpected yet robust ferroelectricity in a monolayer of MoS_2 , making it the thinnest known ferroelectric [162].

Our work shows that the chiral arrangement of atoms in trigonal selenium gives rise to coupling between its lattice and external electric field. The spin-polarized surface in selenium arises from its unique electronic structure with non-trivial topology, reflected in the Berry phase of π , and these surface spins couple with its IR-active phonons. This highly unusual coupling of lattice with the electric field and surface spins gives rise to magnetoelectric coupling and multiferroic behaviour in low dimensional samples (such as slabs or microtubes) of selenium. On the other hand, the AC-magnetoelectric coupling in

trigonal bulk selenium is quite different, and arises from the coupling of its chiral structure (phonons) with external electric field. This leads to rotation of the plane of polarization of light (optical rotation) passing perpendicular to the chiral axis of the bulk.

We have summarized the work in this thesis in a schematic (see Figure 8) that brings out the commonality and central theme of the topics covered. In summary, we highlight how the influence of defects on the coupled motion of electronic (charge and spin) and structural degrees of freedom (phonons and strain) give rise to unexpected physical phenomena and fascinating behaviour of a material.

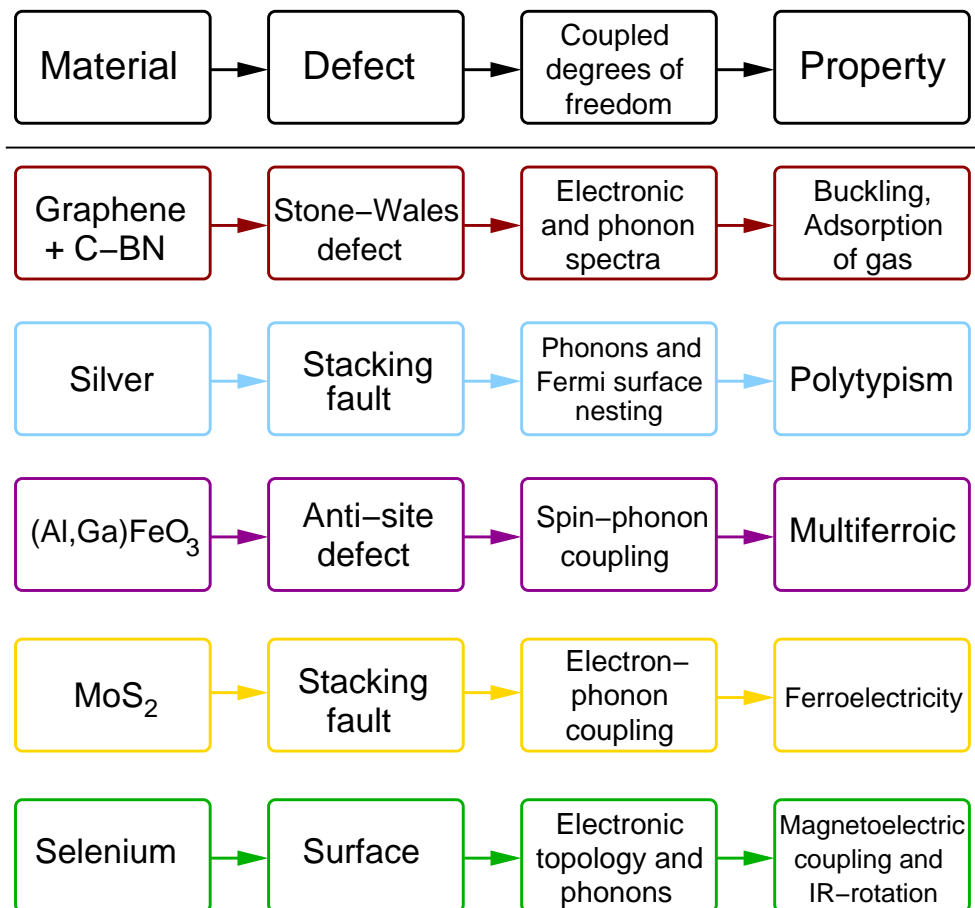


Figure 8.1: Schematic summarizing our work presented in the thesis.

Bibliography

- [1] W. Kohn and L. J. Sham, Phys. Rev. **140**, A1133 (1965).
- [2] P. Hohenberg and W. Kohn, Phys. Rev. **136**, B864 (1964).
- [3] D. Caliste and P. Pochet, Phys. Rev. Lett. **97**, 135901 (2006).
- [4] P. Fahey, S. Iyer, and G. J. Scilla, Applied Physics Letters **54**, 843 (1989).
- [5] E. A. Secco and W. J. Moore, The Journal of Chemical Physics **26**, 942 (1957).
- [6] G. L. Pearson and J. Bardeen, Phys. Rev. **75**, 865 (1949).
- [7] D. Stein, J. L. Jr., and A. Seybolt, Acta Metallurgica **11**, 1253 (1963).
- [8] D. Kuhlmann-Wilsdorf, Materials Science and Engineering: A **113**, 1 (1989).
- [9] G. I. Taylor, Proceedings of the Royal Society of London. Series A, Containing Papers of a Mathematical and Physical Character **145**, 362 (1934).
- [10] C. Fan and A. Inoue, Materials Transactions, JIM(Japan) **38**, 1040 (1997).
- [11] Z. Yin, Q. Pan, Y. Zhang, and F. Jiang, Materials Science and Engineering: A **280**, 151 (2000).
- [12] A. Istratov *et al.*, Journal of The Electrochemical Society **145**, 3889 (1998).
- [13] V. Garcia *et al.*, Nature **460**, 81 (2009).
- [14] R. Guo *et al.*, Nat Commun **4**, (2011).
- [15] J. F. Scott, Ferroelectrics **314**, 207 (2005).
- [16] J. Valasek, Phys. Rev. **17**, 475 (1921).
- [17] G. Busch and P. Scherrer, Naturwissenschaften **23**, 737 (1935).

-
- [18] B. Wul and I. M. Goldman, C.R. Acad. Sci. U.R.S.S. **51**, 21 (1946).
- [19] A. Von Hippel, R. G. Breckenridge, F. G. Chesley, and L. Tisza, Ind. and Eng. Chem. **38**, 1097 (1946).
- [20] C. Randall, R. Newnham, and L. Cross, Web Source (2004).
- [21] W. Cochran, Advan. Phys. **9**, 387 (1960).
- [22] P. W. Anderson, Fizika Dielektrikov (ed. G. I. Skanavi) Akad. Nauk. SSSR Moscow (1960).
- [23] N. Ikeda *et al.*, Nature **436**, 1136 (2005).
- [24] K. Gupta, P. Mahadevan, P. Mavropoulos, and M. Ležaić, Phys. Rev. Lett. **111**, 077601 (2013).
- [25] T. Kimura *et al.*, Nature **426**, 55 (2003).
- [26] C. Fennie and K. Rabe, Phys. Rev. B **72**, 100103 (2005).
- [27] B. B. Van Aken, T. T. Palstra, A. Filippetti, and N. A. Spaldin, Nat Mater **3**, 164 (2004).
- [28] P. Souvatzis, O. Eriksson, M. Katsnelson, and S. Rudin, Computational Materials Science **44**, 888 (2009).
- [29] M. Born and R. Oppenheimer, Annalen der Physik **389**, 457 (1927).
- [30] J. P. Perdew, K. Burke, and M. Ernzerhof, Phys. Rev. Lett. **77**, 3865 (1996).
- [31] J. Perdew, P. Ziesche, and H. Eschrig, Akademie-Verlag, Berlin 11 (1991).
- [32] B. Hammer, M. Scheffler, K. W. Jacobsen, and J. K. Nørskov, Phys. Rev. Lett. **73**, 1400 (1994).
- [33] E. Penev, P. Kratzer, and M. Scheffler, The Journal of Chemical Physics **110**, (1999).
- [34] D. Vanderbilt, Phys. Rev. B **41**, 7892 (1990).
- [35] P. Pulay, Molecular Physics **17**, 197 (1969).
- [36] S. G. Louie, K.-M. Ho, and M. L. Cohen, Phys. Rev. B **19**, 1774 (1979).
- [37] P. Souvatzis and O. Eriksson, Phys. Rev. B **77**, 024110 (2008).
- [38] P. Souvatzis, O. Eriksson, M. I. Katsnelson, and S. P. Rudin, Phys. Rev. Lett. **100**, 095901 (2008).

-
- [39] S. N. Shirodkar and U. V. Waghmare, Phys. Rev. B **86**, 165401 (2012).
- [40] K. S. Novoselov *et al.*, Science **306**, 666 (2004).
- [41] K. S. Novoselov *et al.*, Nature **438**, 197 (2005).
- [42] A. H. Castro Neto, F. Guinea, and N. M. R. Peres, Phys. Rev. B **73**, 205408 (2006).
- [43] Y. Zhang, Y.-W. Tan, H. L. Stormer, and P. Kim, .
- [44] N. D. Mermin, Phys. Rev. **176**, 250 (1968).
- [45] P. Le Doussal and L. Radzihovsky, Phys. Rev. Lett. **69**, 1209 (1992).
- [46] J. C. Meyer *et al.*, Nature **446**, 60 (2007).
- [47] A. Fasolino, J. H. Los, and M. I. Katsnelson, Nat Mater **6**, 858 (2007).
- [48] Y. Zhao, R. E. Smalley, and B. I. Yakobson, Phys. Rev. B **66**, 195409 (2002).
- [49] S. Bhowmick, A. K. Singh, and B. I. Yakobson, The Journal of Physical Chemistry C **115**, 9889 (2011).
- [50] R. C. Thompson-Flagg, M. J. B. Moura, and M. Marder, EPL (Europhysics Letters) **85**, 46002 (2009).
- [51] S. Kumar, K. P. S. S. Hembram, and U. V. Waghmare, Phys. Rev. B **82**, 115411 (2010).
- [52] J. C. Meyer *et al.*, Nano Letters **8**, 3582 (2008).
- [53] J. Ma, D. Alfè, A. Michaelides, and E. Wang, Phys. Rev. B **80**, 033407 (2009).
- [54] X. Peng and R. Ahuja, Nano Letters **8**, 4464 (2008).
- [55] V. N. Popov, L. Henrard, and P. Lambin, Carbon **47**, 2448 (2009).
- [56] P. Giannozzi *et al.*, Journal of Physics: Condensed Matter **21**, 395502 (19pp) (2009).
- [57] J. P. Perdew and A. Zunger, Phys. Rev. B **23**, 5048 (1981).
- [58] H. Amara *et al.*, Phys. Rev. B **76**, 115423 (2007).
- [59] F. Liu, P. Ming, and J. Li, Phys. Rev. B **76**, 064120 (2007).
- [60] A. R. Akhmerov and C. W. J. Beenakker, Phys. Rev. B **77**, 085423 (2008).
- [61] E. Ertekin, D. C. Chrzan, and M. S. Daw, Phys. Rev. B **79**, 155421 (2009).
- [62] N. Levy *et al.*, Science **329**, 544 (2010).

-
- [63] N. N. Klimov *et al.*, *Science* **336**, 1557 (2012).
- [64] G. M. M. Wakker, R. P. Tiwari, and M. Blaauboer, *Phys. Rev. B* **84**, 195427 (2011).
- [65] K.-J. Kim, Y. M. Blanter, and K.-H. Ahn, *Phys. Rev. B* **84**, 081401 (2011).
- [66] A. Carpio, L. L. Bonilla, F. de Juan, and M. A. H. Vozmediano, *New Journal of Physics* **10**, 053021 (2008).
- [67] O. Dubay and G. Kresse, *Phys. Rev. B* **67**, 035401 (2003).
- [68] S. Pisana *et al.*, *Nat Mater* **6**, 198 (2007).
- [69] M. Lazzeri *et al.*, *Phys. Rev. B* **73**, 155426 (2006).
- [70] P. Venezuela, M. Lazzeri, and F. Mauri, *Phys. Rev. B* **84**, 035433 (2011).
- [71] N. kumar *et al.*, *J. Mater. Chem. A* **1**, 5806 (2013).
- [72] C. Dimitrakopoulos *et al.*, *Journal of Vacuum Science and Technology B: Microelectronics and Nanometer Structures* **28**, 985 (2010).
- [73] K. Raidongia *et al.*, *Chemistry A European Journal* **16**, 149 (2010).
- [74] N. Kumar *et al.*, *Journal of Solid State Chemistry* **184**, 2902 (2011).
- [75] L. Song *et al.*, *Phys. Rev. B* **86**, 075429 (2012).
- [76] J. M. Pruneda, *Phys. Rev. B* **81**, 161409 (2010).
- [77] D. M. Ceperley and B. J. Alder, *Phys. Rev. Lett.* **45**, 566 (1980).
- [78] S. Grimme, *Journal of Computational Chemistry* **27**, 1787 (2006).
- [79] V. V. Ivanovskaya *et al.*, *The Journal of Physical Chemistry C* **113**, 16603 (2009).
- [80] J. d. R. Martins and H. Chacham, *Phys. Rev. B* **86**, 075421 (2012).
- [81] H. Nozaki and S. Itoh, *Journal of Physics and Chemistry of Solids* **57**, 41 (1996).
- [82] L. Ci *et al.*, *Nat Mater* **9**, 430 (2010).
- [83] M. S. C. Mazzoni, R. W. Nunes, S. Azevedo, and H. Chacham, *Phys. Rev. B* **73**, 073108 (2006).
- [84] X. Blase, J.-C. Charlier, A. D. Vita, and R. Car, *Applied Physics Letters* **70**, 197 (1997).
- [85] L. Li, S. Reich, and J. Robertson, *Phys. Rev. B* **72**, 184109 (2005).

- [86] B. Xu, Y. H. Lu, Y. P. Feng, and J. Y. Lin, *Journal of Applied Physics* **108**, 073711 (2010).
- [87] S. Bhowmick and U. V. Waghmare, *Phys. Rev. B* **81**, 155416 (2010).
- [88] M. Fujita, K. Wakabayashi, K. Nakada, and K. Kusakabe, *Journal of the Physical Society of Japan* **65**, 1920 (1996).
- [89] H. Lee *et al.*, *Phys. Rev. B* **72**, 174431 (2005).
- [90] Y.-W. Son, M. L. Cohen, and S. G. Louie, *Nature* **444**, 347 (2006).
- [91] Y. Ding, Y. Wang, and J. Ni, *Applied Physics Letters* **94**, 073111 (2009).
- [92] I. Chakraborty *et al.*, *Journal of Physics: Condensed Matter* **23**, 325401 (2011).
- [93] F. Bechstedt *et al.*, *physica status solidi (b)* **202**, 35 (1997).
- [94] J. Casady and R. Johnson, *Solid-State Electronics* **39**, 1409 (1996).
- [95] D. Novgorodova, A. Gorshkov, and A. Mokhov, *Zap. Vses. Mineral. Obs.* **102**, 552 (1979).
- [96] F. Ernst *et al.*, *Phys. Rev. Lett.* **69**, 620 (1992).
- [97] I. Chakraborty *et al.*, *Journal of Physics: Condensed Matter* **26**, 025402 (2014).
- [98] I. Chakraborty *et al.*, *Journal of Physics: Condensed Matter* **in print**, (2014).
- [99] C. N. R. Rao and K. J. Rao, *Phase transitions in solids / C. N. R. Rao and K. J. Rao*, 1st ed ed. (New York : McGraw-Hill, ADDRESS, 1977), includes index.
- [100] G. Trigunayat, *Solid State Ionics* **48**, 3 (1991).
- [101] T. Thomas, D. Pandey, and U. V. Waghmare, *Phys. Rev. B* **77**, 121203 (2008).
- [102] R. Saha *et al.*, *Journal of Solid State Chemistry* **184**, 494 (2011).
- [103] K. Kelm and W. Mader, *Zeitschrift fr anorganische und allgemeine Chemie* **631**, 2383 (2005).
- [104] F. Bouree *et al.*, *Acta Crystallographica Section B* **52**, 217 (1996).
- [105] K. Sharma *et al.*, *Journal of Physics: Condensed Matter* **22**, 146005 (2010).
- [106] J. P. Remeika, *Journal of Applied Physics* **31**, (1960).
- [107] G. T. Rado, *Phys. Rev. Lett.* **13**, 335 (1964).
- [108] A. Shireen *et al.*, *J. Mater. Chem.* **21**, 57 (2011).

-
- [109] G. Kresse and J. Hafner, Phys. Rev. B **47**, 558 (1993).
- [110] G. Kresse and J. Hafner, Phys. Rev. B **49**, 14251 (1994).
- [111] G. Kresse and J. Furthmüller, Phys. Rev. B **54**, 11169 (1996).
- [112] G. Kresse and J. Furthmüller, Computational Materials Science **6**, 15 (1996).
- [113] G. Kresse and D. Joubert, Phys. Rev. B **59**, 1758 (1999).
- [114] J. B. Neaton *et al.*, Phys. Rev. B **71**, 014113 (2005).
- [115] V. V. Bhat, A. M. Umarji, V. B. Shenoy, and U. V. Waghmare, Phys. Rev. B **72**, 014104 (2005).
- [116] P. Kumar *et al.*, Phys. Rev. B **85**, 134449 (2012).
- [117] R. Saha *et al.*, Solid State Communications **152**, 1964 (2012).
- [118] A. B. Sushkov *et al.*, Journal of Physics: Condensed Matter **20**, 434210 (2008).
- [119] J. Junquera and P. Ghosez, Nature **422**, 506 (2003).
- [120] D. D. Fong *et al.*, Science **304**, 1650 (2004).
- [121] A. V. Bune *et al.*, Nature **391**, 874 (1998).
- [122] H. S. S. R. Matte *et al.*, Angewandte Chemie **122**, 4153 (2010).
- [123] C. Rovira and M. H. Whangbo, Inorganic Chemistry **32**, 4094 (1993).
- [124] K. F. Mak *et al.*, Phys. Rev. Lett. **105**, 136805 (2010).
- [125] B. Radisavljevic *et al.*, Nat Nano **6**, 147 (2011).
- [126] H. T. Stokes, D. M. Hatch, and B. J. Campbell, (ISOTROPY, 2007).
- [127] M. I. Aroyo *et al.*, Acta Crystallographica Section A **62**, 115 (2006).
- [128] J. Wilson and A. Yoffe, Advances in Physics **18**, 193 (1969).
- [129] F. Wypych, T. Weber, and R. Prins, Chem. Mater. **10**, 723 (1998).
- [130] J. Heising and M. G. Kanatzidis, Journal of the American Chemical Society **121**, 638 (1999).
- [131] A. M. Gabovich, A. I. Voitenko, J. F. Annett, and M. Ausloos, Superconductor Science and Technology **14**, R1 (2001).
- [132] X. Rocquefelte *et al.*, Phys. Rev. B **62**, 2397 (2000).

-
- [133] U. Maitra *et al.*, *Angewandte Chemie International Edition* **52**, 13057 (2013).
- [134] U. V. Waghmare, N. A. Spaldin, H. C. Kandpal, and R. Seshadri, *Phys. Rev. B* **67**, 125111 (2003).
- [135] N. Sai, C. J. Fennie, and A. A. Demkov, *Phys. Rev. Lett.* **102**, 107601 (2009).
- [136] B. Meyer and D. Vanderbilt, *Phys. Rev. B* **65**, 104111 (2002).
- [137] W. Zhou *et al.*, *Nano Letters* **13**, 2615 (2013).
- [138] Y.-H. Shin, I. Grinberg, I.-W. Chen, and A. M. Rappe, *Nature* **449**, 881 (2007).
- [139] M. Calandra and F. Mauri, *Phys. Rev. Lett.* **106**, 196406 (2011).
- [140] E. Morosan *et al.*, *Nat. Phys.* **2**, 544 (2006).
- [141] M. H. Whangbo and E. Canadell, *Journal of the American Chemical Society* **114**, 9587 (1992).
- [142] A. Pal *et al.*, *Sci. Rep.* **3**, 2051 (2013).
- [143] N. A. Hill, *The Journal of Physical Chemistry B* **104**, 6694 (2000).
- [144] G. Catalan and J. F. Scott, *Advanced Materials* **21**, 2463 (2009).
- [145] N. Hur *et al.*, *Nature* **429**, 392 (2004).
- [146] X.-L. Qi, T. L. Hughes, and S.-C. Zhang, *Phys. Rev. B* **78**, 195424 (2008).
- [147] A. M. Essin, J. E. Moore, and D. Vanderbilt, *Phys. Rev. Lett.* **102**, 146805 (2009).
- [148] R. D. King-Smith and D. Vanderbilt, *Phys. Rev. B* **47**, 1651 (1993).
- [149] C. Hartwigsen, S. Goedecker, and J. Hutter, *Phys. Rev. B* **58**, 3641 (1998).
- [150] X. Gonze *et al.*, *Computer Physics Communications* **180**, 2582 (2009), 40 YEARS OF CPC: A celebratory issue focused on quality software for high performance, grid and novel computing architectures.
- [151] X. Gonze, *Zeitschrift für Kristallographie - Crystalline Materials* **220**, .
- [152] O. V. Yazyev, *Reports on Progress in Physics* **73**, 056501 (2010).
- [153] M. Z. Hasan and J. E. Moore, *Annu. Rev. Condens. Matter Phys.* **2**, 55 (2011).
- [154] A. A. Soluyanov and D. Vanderbilt, *Phys. Rev. B* **83**, 235401 (2011).
- [155] I. Chen and R. Zallen, *Phys. Rev.* **173**, 833 (1968).

-
- [156] R. A. Lombardi and L. A. Nafie, *Chirality* **21**, E277 (2009).
- [157] S. Orfanidis, *Electromagnetic Waves and Antennas* (online, <http://www.ece.rutgers.edu/orfanidi/ewa/>, 2004), Chap. 3.
- [158] T. Nishimatsu, U. V. Waghmare, Y. Kawazoe, and D. Vanderbilt, *Phys. Rev. B* **78**, 104104 (2008).
- [159] J. E. Adams and W. Haas, *The Physics of Selenium and Tellurium* (W. C. Cooper, Pergamon Press, New York, 1969).
- [160] G. W. Day, *Applied Physics Letters* **18**, 347 (1971).
- [161] H. Zhong, Z. H. Levine, D. C. Allan, and J. W. Wilkins, *Phys. Rev. Lett.* **69**, 379 (1992).
- [162] S. N. Shirodkar and U. V. Waghmare, *Phys. Rev. Lett.* **112**, 157601 (2014).